1506
UNIVERSITÀ
DEGLI STUDI
DI URBINO
CARLO BO

DIPARTIMENTO DI SCIENZE PURE E APPLICATE (DISPEA)

CORSO DI DOTTORATO DI RICERCA IN SCIENZE DI BASE E APPLICAZIONI

Curriculum Scienze della Terra

XXXI Ciclo

The role of orbital forcing in the early-middle Eocene carbon cycle: a marine perspective

Il ruolo della forzante orbitale nel ciclo del carbonio dell'Eocene inferiore-medio: una prospettiva marina

SSD Geo/01

RELATORE

Chiar.mo Prof. Simone Galeotti

DOTTORANDA

Dott.ssa Federica Francescone

ANNO ACCADEMICO 2017/2018

CONTENTS

INTRODUCTION

In the last decades global concentration of atmospheric greenhouse gases (GHGs) have produced irreversible effects on our climate system (Intergovernmental Panel for Climate Change - IPCC - 2014). One issue of particular concern is the rising of the carbon dioxide (CO_2) atmospheric concentration, which overcame the threshold of 400 parts per million (ppm), modifying the terrestrial radiative forcing. Accordingly, the observed global mean surface temperature for the decade 2006-2015 was estimated to be on average 0.87°C higher than the average over the 1850-1900 period (IPCC, 2014).

The most recent IPCC report (2014) considers diverse future scenarios by the end of the 21th century, characterized by different hypothesis of magnitude and emission rates of GHGs. These pathways, which have been defined as Representative Concentration Pathways (RCPs), include a stringent mitigation scenario (RCP2.6), two intermediate scenarios (RCP4.5 and RCP6.0) and one characterized by very high GHG concentration (RCP8.5). Scenarios without additional efforts to limit the emission lead to a RCP8.5 pathway (IPCC, 2014), which is characterized by atmospheric CO_2 concentration of ~1000 ppm (Fig. 1).

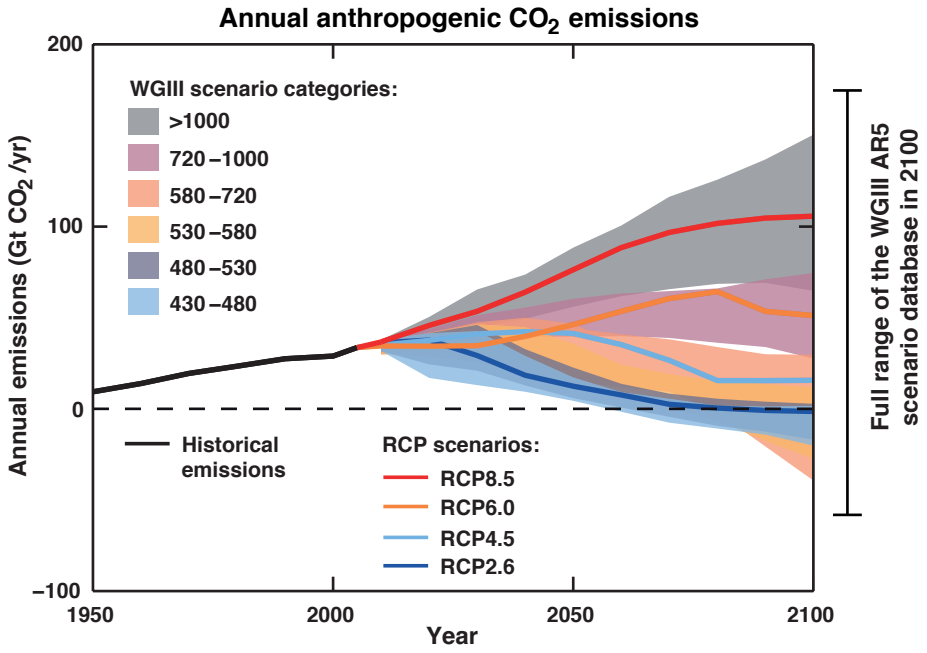

Figure 1: *Emissions of carbon dioxide (CO_2) alone in the Representative Concentration Pathways (RCPs) (lines) and the associated scenario categories used in Working Group (WG) III (colored areas show 5 to 95% range). The WGIII scenario categories summarize the wide range of emission scenarios published in the scientific literature and are defined on the basis of CO_2-eq concentration levels (in ppm) in 2100 (IPCC, 2014).*

Forecasting the magnitude of the global warming is one of the big scientific challenges. Indeed, all these pathways are characterized by a huge uncertainties due to the complexity of the climatic system.

Moreover, the Climate Sensitivity, i.e. the response of the mean global surface temperature to a doubling of atmospheric CO_2 concentration, which value is estimated between 1.5 and 4.5°C (IPCC, 2014), is affected by a range of uncertainty as well. Longer-trend Climate Sensitivity is determined by internal feedbacks, both positive and negative, that either amplify or diminish the GHG effects as a response of the dynamic steady state variations.

Geological record can be used as a key that can lead to a better understanding of the impact of extreme global warming on the ocean-atmosphere coupled system and the relationship between carbon cycle and climate in worlds characterized by GHG concentrations very similar to that forecast by different RCP scenarios. Accordingly, certain time intervals in the past provide a unique opportunity to assess climate model because they capture the behavior of Earth's climate system under pCO_2 concentrations that likely could be reached in the future. In particular, some time intervals and events are representative of mean global conditions similar to the more extreme scenarios predicted for the end of the century (RCP8.5), being characterized by levels equal or higher than 1000 ppm. The most recent geological time period characterized by this GHGs concentration is represented by the early Eocene and the so called hyperthermal events, occurring between ~56 and 51 million years ago (Ma).

The early-middle Eocene and hyperthermal events

The Cenozoic climate, the last ~65 million years (Myr), was characterized by a great variability (Fig. 2). As recorded in the $\delta^{18}O$ isotope curve, this time interval shows several steps at different time scales (10^7-10^4 years), which can be associated with episodes of warming and cooling (Zachos et al., 2001). Most of the variability is expressed through the Paleocene-Eocene epochs. A long-term global warming characterizes the evolving Greenhouse climate system through the late Paleocene and the early Eocene (~60-50 Ma), making the early Eocene (~56 to ~48 Ma) the warmest period over the entire Cenozoic. This gradual warming is followed by a long-term cooling eventually leading to the emplacement of a typical Icehouse climate system at the Eocene/Oligocene transition (~34 Ma) with the first significant appearance of a continental-scale Antarctic ice sheet (Zachos et al., 2008). The gradual warming that affected the Paleocene-early Eocene was punctuated by a series of transient (10^4-10^5 years) global warming events, called hyperthermals (Cramer et al., 2003; Lourens et al., 2005; Galeotti et al., 2010, 2017; Zachos et al., 2010; Sexton et al., 2011; Littler et al., 2014; Kirtland Turner et al., 2014; Lauretano et al., 2015, 2016, 2018).

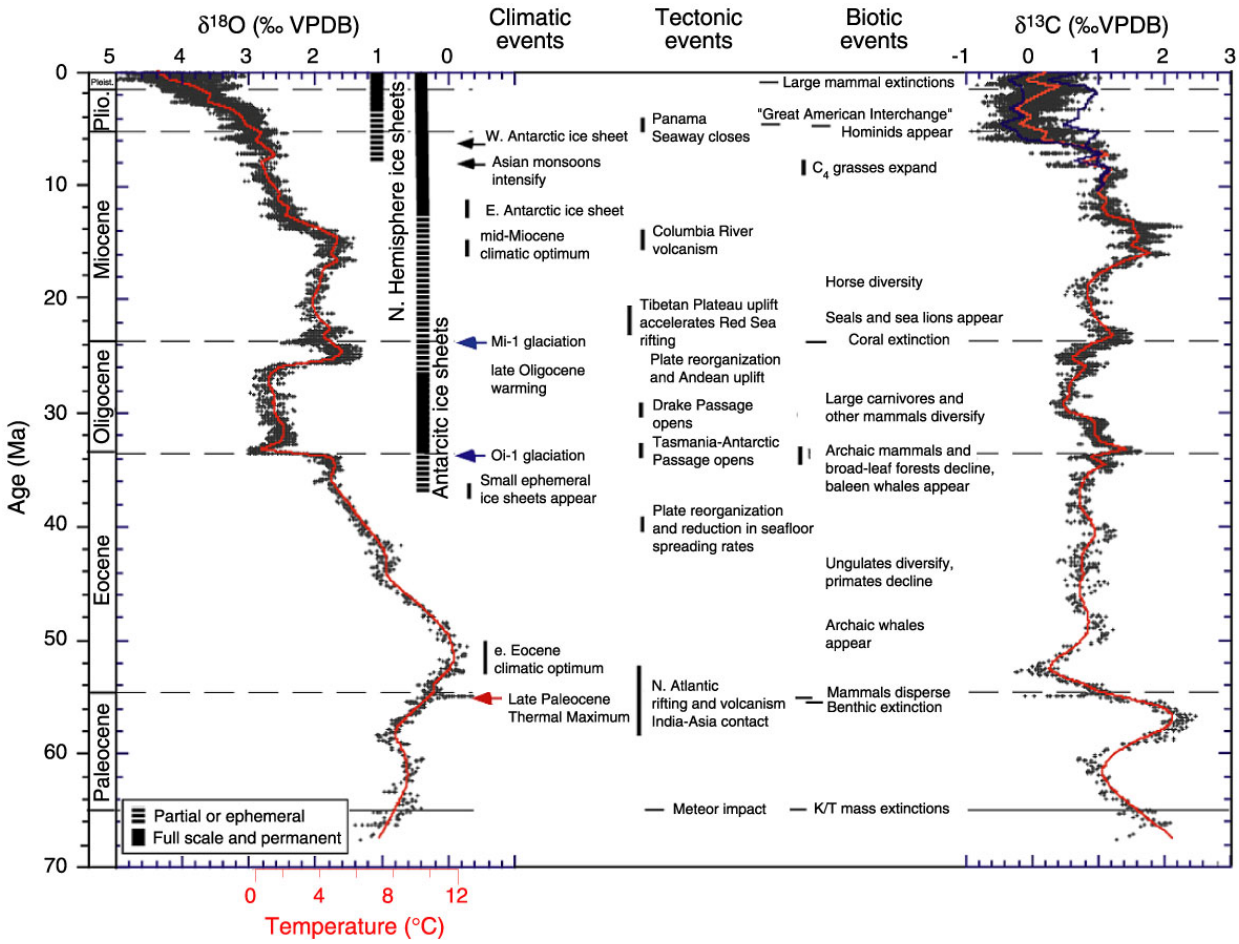

Figure 2: *Global deep-sea oxygen and carbon isotope records based on data compiled from more than 40 DSDP and ODP sites (Zachos et al., 2001).*

Hyperthermal events are linked to massive perturbations of the global carbon cycle related to the input of isotopically light carbon into the exogenic carbon pool (Dickens et al., 1995; Lourens et al., 2005; Zachos et al., 2005, 2010; Nicolo et al., 2007; Westerhold and Röhl, 2009; Galeotti et al., 2010; Galeotti et al., 2017). These extreme events are recorded globally as negative Carbon Isotopic Excursions (CIEs) and are associated with concomitant sediments depleted in calcium carbonate ($CaCO_3$) in deep-sea and shallow marine successions as a response to the sudden rising of the Carbonate Compensation Depth (CCD – Zachos et al., 2005) and the acceleration of the global hydrological cycle (Ravizza et al., 2001), thus runoff, respectively.

The most pronounced of these events is the Paleocene-Eocene Thermal Maximum (PETM), at ~56 Ma (Zachos et al. 2005; Tripati and Elderfield, 2005; Sluijs et al., 2008; Lourens et al., 2005; Westerhold et al., 2007; Galeotti et al., 2010, 2017). The PETM is characterized by the largest Cenozoic extinction of calcareous deep-marine benthic foraminifera (Thomas, 1989; Thomas and Shackleton, 1996) and is associated with a CIE of ~3‰ (Kennett and Stott, 1991; Koch et al., 1992; Thomas et al., 2002; Pagani et

al., 2006) and a negative excursion in $\delta^{18}O$ of benthic foraminifera of ~1.5‰ (Kennett and Stott, 1991; Thomas and Shackleton, 1996; Zachos et al., 2001), which suggests an increase of ~6°C of sea-water temperature concomitant to the CIE. Beside the PETM, at least other two hyperthermal events, Eocene Thermal Maximum (ETM) 2 (also known as ELMO or H1) and ETM3 (also known as K or X event), at ~54.1 and ~52.8 Ma, respectively, occurred during the early Eocene (Lourens et al., 2005; Röhl et al., 2005). However, the associated CIEs are smaller (~2‰ and ~1‰ for ETM2 and ETM3, respectively) and also deep marine carbonate dissolution is less pronounced compared to the PETM (Lourens et al., 2005; Röhl et al., 2005).

Recently, similar events of comparable isotopic excursions have been discovered in the global bulk and benthic isotopic records (Sexton et al., 2011; Kirtland Turner et al., 2014; Lauretano et al., 2016, 2018; Westerhold et al., 2017, 2018). In particular, the Early Eocene Climatic Optimum (EECO), ~51 Ma, seems to be the maximal expression of these transient events. The EECO recorded the highest temperature of the Cenozoic (Zachos et al., 2001, 2008). During this time interval deep-water temperatures at high latitude were higher than present days, with peaks of 15-23°C (Zachos et al. 2010, Huber and Thomas 2008). Moreover, atmospheric pCO_2 level was estimated at ~1000 ppm (Zachos et al., 2001). Based on the available data (Hansen et al., 2008), the EECO is characterized by mean atmospheric CO_2 levels which well approach the RCP8.5 scenario. The interpretation of the EECO is an issue of particular interest because of its potential relevance for understanding the dynamics of this climatic system.

Although the hypothesis of successive releases of huge amounts of carbon as a mechanism for the emplacements of hyperthermals is widely accepted by the scientific community, a debate still exists on the possible sources. Various sources have been proposed, such as the destabilization of methane clathrates (Dickens et al., 1995), burning of terrestrial organic matter as extensive peat and coal deposits (Kurtz et al., 2003) and thawing and subsequent oxidation of the permafrost from the high latitude settings (DeConto et al., 2012). Several authors highlight the importance of the orbital forcing as a trigger mechanism for hyperthermal events (Westerhold and Röhl, 2009; Sexton et al., 2011; Kirtland Turner et al., 2014; Galeotti et al., 2010, 2017; Lauretano et al., 2016). Indeed, an astronomical forcing signature on the succession of hyperthermals allows to develop a cyclostratigraphy at a very high-resolution that permits to correlate each event to their respective counterparts of the Pacific and Atlantic Oceans, by designing a global observation system.

Furthermore, cyclostratigraphic approach permits to obtain an astronomical time scale which allows to verify the phase relationships between the orbital forcing and the sedimentary/geochemical response. The accuracy of the time scale is important for a better estimate of the emission rates of GHGs, in order to provides a crucial elements for the design of climate (paleo)models.

Moreover, the noted amplitude of the astronomical forcing allows to analyze the response of the system to a measurable forcing.

Astronomical Time Scale (ATS)

Determining an accurate age model of the carbon cycle aberrations is critical to explore causes and consequences of past climate change.

High-resolution $CaCO_3$ and carbon isotope Cenozoic records show that the aberrations in the global carbon cycle are paced by periodic oscillations in Earth's astronomical parameters (Zachos et al., 2001; Cramer et al., 2003; Billups et al., 2004; Holbourn et al., 2005; Pälike et al., 2006), determined by Milankovitch cycles. These cyclical variations are mainly represented by the eccentricity long- and short-terms, obliquity and precession with characteristic period of ~400 and ~100, ~41 and ~20 kyr, respectively. Milankovitch cycles directly control the distribution of the Solar Energy on Earth and to a limited extent its total amount. The identification of these cyclic components in the terrestrial and marine sedimentary archives and the development of a cyclostratigraphic record tuned to the newest target curve (Laskar et al., 2011), provide a powerful astrochronological framework which can be used for the calibration of the entire Cenozoic timescale. In particular, the Earth's orbital eccentricity component is widely used for astrochronological calibrations against the astronomical solution and the precision of the Astronomical Time Scale (ATS) strictly depends on the uncertainties in the eccentricity astronomical solution itself (Laskar et al., 2004, 2011). Indeed, Earth's short eccentricity (~100 kyr) cycles are reliable back to ~50 Ma. Beyond this age, the chaotic behavior of large bodies within the asteroid belt makes it uncertain (Laskar et al., 2001, Westerhold et al., 2012). In spite of this, the long eccentricity (~400 kyr) cycle component is stable up to 200 Ma. The best approach for the development of a complete ATS for the early Cenozoic is the identification of the 400 kyr periodic component in the sedimentary archives, thus providing a powerful metronome for the cyclostratigraphic calibration of sedimentary archives and proxy record derived from them (Laskar et al., 2004; Hinnov and Hilgen, 2012).

A cyclostratigraphic/astrochronologic numerical time scale is available for much of Cenozoic time interval (Pälike and Hilgen, 2008; Hinnov and Hilgen, 2012). However, uncertainties still affect the ATS, partly due to the scarcity of well-exposed and continuous geochemical and magnetostratigraphic records, in particular across the silica-rich (McGowran, 1989) EECO interval (Fig.3).

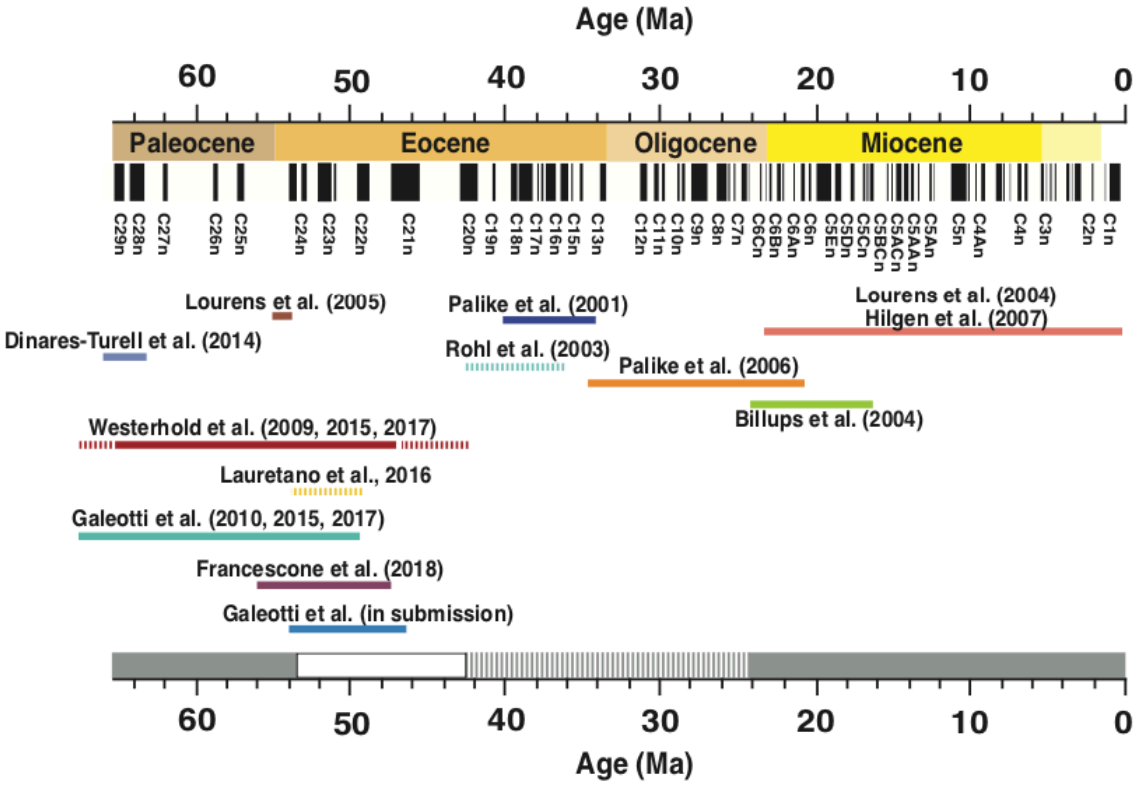

Figure 3: *Summary of orbital timescale calibrations for the Cenozoic era in the context of climatic cycles (Modified from Pälike and Hilgen, 2008). The lowermost horizontal gray line indicates a fairly stable and accurate astronomical age calibration with multiple site coverage (solid line), and more tentative or unverified age calibrations (dashed line). There is a significant gap in the middle Eocene, ~42 to 53 Myr ago (white box).*

In this thesis we present a new high-resolution geochemical and bulk stable carbon isotopic record, integrated with bio- and magneto-stratigraphic analyses, from classic Tethyan successions cropping out in the Umbria-Marche basin (Italy) and from the Possagno section located in Southern Alps.

The main aim of this project was to contribute to the characterization of hyperthermal events across the early-middle Eocene time interval, defining a precise cyclochronological scheme of these events accompanied with the development of an accurate astronomically calibrated age model. It further can aid in closing the existing middle Eocene gap in the ATS (Pälike and Hilgen, 2008), partly due to the scarcity of well-exposed and continuous geochemical and magnetostratigraphic records across the silica-rich EECO interval (McGowran, 1989).

Outline of the Chapters

The early Eocene (~56 to ~48 Ma) is recorded in the pelagic Scaglia Rossa and Variegata Formations (Fms.) of the Umbria-Marche (U-M) Basin (central Italy). In **Chapter I** a high-resolution integrated magneto-chemo- and cyclo-stratigraphic record from two classic Tethyan section, Contessa Road and Bottaccione sections (Gubbio, Central Italy) is presented. The occurrence of a prominent, 10 cm-thick, marly layer laying ~2 m below the C23r-C23n magnetochron boundary has been used as a marker bed to correlate the two outcrops. This allows splicing a continuous high-resolution record spanning the lower part of magnetochron C24r to the upper part of magnetochron C22r. The detection of orbital components in the geochemical record allows establishing a relative cyclochronology of magnetochrons and hyperthermal events across the EECO, thus providing a criterion for its univocal identification in any cyclostratigraphic interpretation of marine successions. Moreover, cycle-counting across C23r and C23n magnetochrons allows solving the discrepancies between time scales based on astrochronological and radioisotopic age interpretation across what has been defined as "problematic interval" by Lauretano et al. (2016).

In **Chapter II** a new detailed integrated stratigraphy for the late early to middle Eocene from the Bottaccione section and a newly drilled core located at Smirra (central Italy) is presented. The new data, combined with the record previously published of Galeotti et al. (2017) from the same area, allowed us to extend it from the lower part of magnetochron C24n to the upper part of magnetochron C21n. The resulting record provides a continuous cyclochronological framework spanning 56.0 to 47.5 Ma. We independently test our age model by using sea-surface magnetic anomaly profiles from different oceanic basins, which provides evidence for the robustness of our astrochronological framework spanning the first 9 Myr of the Eocene. This work contributes to a better definition of the cyclochronology of hyperthermal events and to close the middle Eocene gap in the ATS. Indeed, this interval results to be well-preserved in the indurated limestone of the Umbria-Marche succession.

In **Chapter III** we present a high-resolution isotopic analysis of the early Eocene to middle Eocene (~51-45 Ma) time interval from the Possagno section located in the Southern Alps. The section provides a continuous and undisturbed chemostratigraphic and cyclochronological record across a critical time interval in terms of paleoceanographic and paleoclimatic evolution. Available deep-sea records provide a non-univocal astrochronological interpretation of the surveyed time interval as recently reported by different authors (Lauretano et al., 2016; Galeotti et al., 2017; Westerhold et al., 2017). The Possagno record, together with a core drilled in the same area, contributes to the definition of a correct interpretation of the astrochronology of the early-middle Eocene. Moreover, the good alignment, both on long- and short-trend terms, between Possagno carbon isotope record and coeval records, such as ODP Sites 1258, 1263, 1209 and the U-M basin, evidently results from factors of the carbon cycle which are reflected in the global record.

In **Chapter IV** the covariance between benthic carbon and oxygen stable isotopes during all major early Eocene hyperthermal events, i.e. ETM1 (or PETM), ETM2 ETM3), from South Atlantic (Leg 208, ODP Sites 1262, 1263 and 1265) and Pacific ocean records (ODP Site 1209 - Stap et al., 2010; Lauretano et al., 2015; Westerhold et al., 2018) has been presented. Regression line of stable $\delta^{13}C$ and $\delta^{18}O$ isotope shifts during these events can be used to measure the global warming against the total amount of carbon release, which, in turn, should provide insights on the Climate Sensitivity during the Eocene. Several authors suggest that similar regression slopes in benthic foraminiferal records were caused by carbon release from the same source (Lauretano et al., 2015; Westerhold et al., 2018). In the light of evolving mean background conditions though the early Eocene, we rather point to a gradual depletion in the mass of the isotopically lighter reservoir, implying the existence of more than one reservoir.

INTRODUZIONE

Negli ultimi decenni la concentrazione globale di gas serra ha causato effetti irreversibili sul nostro sistema climatico (Intergovernmental Panel for Climate Change - IPCC - 2014). Una questione di particolare interesse è l'aumento della concentrazione atmosferica di anidride carbonica (CO_2) che ha superato la soglia di 400 parti per milione (ppm), modificando il bilancio radiativo terrestre. Di conseguenza, la temperatura superficiale media globale osservata per il decennio 2006-2015 è stata stimata essere mediamente 0.87°C superiore rispetto alla temperatura media nel periodo 1850-1900 (IPCC, 2014).

Il più recente report dell'IPCC (2014) contempla diversi scenari climatici futuri entro la fine del XXI secolo, caratterizzati da differenti ipotesi di tassi di emissione dei gas ad effetto serra. Questi modelli, definiti come Representative Concentration Pathways (RCP), includono uno scenario di attenuazione rigoroso (RCP2.6), due scenari intermedi (RCP4.5 e RCP6.0) e uno caratterizzato da una concentrazione di GHG molto alta (RCP8.5). In assenza di ulteriori sforzi per limitare le emissioni, lo scenario più probabile è l'RCP8.5 (IPCC, 2014), caratterizzato da una concentrazione di CO_2 atmosferica di ~1000 ppm (Fig.1).

Prevedere la grandezza e il riscaldamento globale è una delle più grandi sfide scientifiche. Infatti, tutti questi modelli sono caratterizzati da enormi incertezze legate alla complessità del sistema climatico. Inoltre, la Sensibilità Climatica, ossia la risposta della temperatura media superficiale globale al raddoppio della concentrazione di CO_2 atmosferica, il cui valore stimato risulta essere compreso tra 1.5 e 4.5°C (IPCC, 2014), è caratterizzata da una grande incertezza. La Sensibilità Climatica sul lungo termine è determinata dalla presenza di meccanismi di feedback interni, sia positivi che negativi, che amplificano o diminuiscono gli effetti dei gas ad effetto serra come risposta alle variazioni dinamiche dello stato di equilibrio.

Il record geologico può fornire importanti informazioni sull''impatto del riscaldamento globale nel sistema accoppiato oceano-atmosfera e sulla relazione tra ciclo del carbonio e clima in mondi caratterizzati da concentrazioni di gas ad effetto serra molto simili a quelle previste dai diversi scenari RCP. Di conseguenza, alcuni intervalli temporali verificatisi in passato forniscono un'opportunità unica per valutare

il modello climatico poiché catturano il comportamento del sistema climatico della Terra in condizioni di concentrazioni di pCO_2 che potrebbero essere raggiunte in futuro. In particolare, alcuni intervalli di tempo ed eventi sono rappresentativi delle condizioni globali medie simili agli scenari più estremi previsti per la fine del secolo (RCP8.5), essendo caratterizzati da livelli uguali o superiori a 1000 ppm. Il periodo geologico più recente caratterizzato da questa concentrazione di gas serra è rappresentato dall'Eocene medio e dai cosiddetti eventi ipertermici, datati tra ~56 e 51 milioni di anni fa (Ma).

L'Eocene medio-inferiore e gli eventi ipertermici

Il clima nel Cenozoico (gli ultimi ~65 milioni di anni - Myr), è stato caratterizzato da una grande variabilità (Fig.2). Come registrato nella curva isotopica $\delta^{18}O$, questo intervallo temporale mostra delle importanti variazioni che si registrano a diverse scale temporali (10^7-10^4 anni) e che possono essere associate a episodi di riscaldamento e raffreddamento (Zachos et al., 2001). La maggior parte della variabilità è espressa attraverso il Paleocene-Eocene. Un riscaldamento globale a lungo termine caratterizza l'evoluzione del sistema climatico di tipo Greenhouse attraverso il Paleocene superiore e l'Eocene inferiore (~60-50 Ma), rendendo l'Eocene inferiore (~56-48 Ma) il periodo più caldo dell'intero Cenozoico. Questo graduale riscaldamento è seguito da un raffreddamento a lungo termine che porta alla collocazione tipica di un sistema climatico di tipo Icehouse alla transizione Eocene/Oligocene (~34 Ma), con la prima comparsa significativa di una calotta polare antartica su scala continentale (Zachos et al., 2008). Il graduale riscaldamento che ha caratterizzato il Paleocene superiore-Eocene inferiore è stato punteggiato da una serie di eventi transienti (10^4-10^5 anni) di riscaldamento globale, chiamati eventi ipertermici (Cramer et al., 2003; Lourens et al., 2005; Galeotti et al., 2010 , 2017; Zachos et al., 2010; Sexton et al., 2011; Littler et al., 2014; Kirtland Turner et al., 2014; Lauretano et al., 2015, 2016, 2018).

Gli eventi ipertermici sono associati a grandi perturbazioni del ciclo globale del carbonio legate all'input di carbonio isotopicamente leggero nel sistema accoppiato oceano/atmosfera (Dickens et al., 1995; Lourens et al., 2005; Zachos et al., 2005, 2010; Nicolo et al., 2007; Westerhold e Röhl, 2009; Galeotti et al., 2010; Galeotti et al., 2017). Questi eventi estremi sono registrati globalmente come escursioni negative nel record isotopico del carbonio (CIE) e sono associati a concomitanti sedimenti impoveriti nel contenuto di carbonato di calcio ($CaCO_3$) nelle successioni marine profonde e superficiali, come risposta all'innalzamento improvviso della profondità di compensazione del carbonato (CCD - Zachos et al., 2005) e all'accelerazione del ciclo idrologico globale (Ravizza et al., 2001), rispettivamente.

Il più pronunciato di questi eventi è il Paleocene-Eocene Thermal Maximum (PETM), a ~56 Ma (Zachos et al., 2005; Tripati and Elderfield, 2005; Sluijs et al., 2008; Lourens et al., 2005; Westerhold et al., 2007; Galeotti et al., 2010, 2017). Il PETM è caratterizzato dalla più grande estinzione cenozoica dei foraminiferi bentonici marini di origine calcarea (Thomas, 1989; Thomas and Shackleton, 1996) ed è associato ad una CIE di ~3 ‰ (Kennett and Stott, 1991; Koch et al., 1992; Thomas et al., 2002; Pagani et

al., 2006) e ad un'escursione negativa nel $\delta^{18}O$ dei foraminiferi bentonici di ~1.5‰ (Kennett and Stott, 1991; Thomas and Shackleton, 1996; Zachos et al. , 2001), suggerendo così un aumento di ~6°C delle temperature delle acque marine in concomitanza con la CIE. Oltre al PETM, almeno altri due eventi ipertermici, l'Eocene Thermal Maximum (ETM) 2 (noto anche come ELMO o H1) e l'ETM3 (noto anche come evento K o X), rispettivamente a ~54.1 e ~52.8 Ma, si sono verificati durante l'Eocene inferiore (Lourens et al., 2005; Röhl et al., 2005). Tuttavia, le CIE associate sono più piccole (~2‰ e ~1‰ per ETM2 e ETM3, rispettivamente), così come anche la dissoluzione del $CaCO_3$ nei sedimenti marini è meno pronunciata rispetto al PETM (Lourens et al., 2005; Röhl et al., 2005) .

Recentemente sono stati scoperti eventi analoghi nei record isotopici bulk e bentonici globali (Sexton et al., 2011; Kirtland Turner et al., 2014; Lauretano et al., 2016, 2018; Westerhold et al., 2017 , 2018). In particolare, l'Early Eocene Climatic Optimum (EECO), ~51 Ma, sembra essere la massima espressione di questi eventi transienti. L'EECO ha registrato la temperatura delle acque marine profonde più alta dell'intero Cenozoico (Zachos et al., 2011, 2008), raggiungendo picchi alle alte latitudini di 15-23°C (Zachos et al. 2010, Huber e Thomas 2008). Inoltre, i livelli di pCO_2 atmosferici erano stimati a ~1000 ppm (Zachos et al., 2001). Sulla base dei dati disponibili (Hansen et al., 2008), l'EECO è caratterizzato da valori medi di CO_2 atmosferica che ben approssimano lo scenario RCP8.5. Lo studio dell'EECO risulta essere, quindi, di particolare interesse grazie alla sua potenziale rilevanza nella comprensione delle dinamiche di tale sistema climatico.

Sebbene l'ipotesi di successivi rilasci di enormi quantità di carbonio come meccanismo determinante la messa in posto degli eventi ipertermici sia ampiamente accettato dalla comunità scientifica, le possibili fonti di carbonio sono ancora molto dibattute. Diverse sono le sorgenti di carbonio proposte, come la destabilizzazione dei metani idrati (Dickens et al., 1995), la combustione di materia organica terrestre derivante da vasti depositi di torba e carbone (Kurtz et al., 2003) e lo scioglimento e successiva ossidazione del permafrost dalle alte latitudine (DeConto et al., 2012). Diversi autori sottolineano l'importanza della forzante orbitale come meccanismo di innesco per gli eventi ipertermici (Westerhold e Röhl, 2009, Sexton et al., 2011; Kirtland Turner et al., 2014; Galeotti et al., 2010, 2017; Lauretano et al., 2016). Un controllo di tipo orbitale nelle successione di eventi ipertermici consente di sviluppare una ciclostratigrafia ad altissima risoluzione che permette di correlare ciascun evento alle rispettive controparti nell'Oceano Pacifico ed Atlantico, disegnando così un sistema di osservazione globale.

Inoltre, un approccio ciclostratigrafico permette di ottenere una scala temporale astronomica che consente di verificare i rapporti di fase tra la forzante orbitale e la risposta sedimentaria/geochimica. L'accuratezza della scala temporale è importante per una migliore stima dei tassi di emissione dei GHG, al fine di fornire elementi cruciali per la progettazione dei modelli (paleo)climatici.

Infine, avendo la forzante orbitale ampiezza nota, consente di studiare la risposta del sistema ad un forcing misurabile.

La Scala Temporale Astronomica

Determinare un modello di età accurato degli eventi di aberrazione del ciclo del carbonio è fondamentale per esplorare le cause e le conseguenze dei cambiamenti climatici del passato.

I records ad alta risoluzione del $CaCO_3$ e degli isotopi del carbonio attraverso il Cenozoico mostrano come le aberrazioni nel ciclo globale del carbonio siano controllate da oscillazioni periodiche nei parametri astronomici della Terra (Zachos et al., 2001; Cramer et al., 2003; Billups et al., 2004; Holbourn et al., 2005; Pälike et al., 2006), determinate dai cicli di Milankovitch. Queste variazioni cicliche sono rappresentate principalmente dall'eccentricità, a lungo e breve termine, obliquità e precessione, con periodi caratteristici di ~400 e ~100, ~41 e ~20 kyr, rispettivamente. I cicli di Milankovitch controllano direttamente la distribuzione dell'energia solare sulla Terra e, in misura limitata, la sua quantità totale. L'identificazione di queste componenti cicliche negli archivi sedimentari terrestri e marini e lo sviluppo di un record ciclostratigrafico sintonizzato alla nuova soluzione astronomica target (Laskar et al., 2011), forniscono un potente impianto astrocronologico che può essere utilizzato per la calibrazione della scala cronologica dell'intero Cenozoico. In particolare, la componente orbitale dell'eccentricità è ampiamente utilizzata per le calibrazioni astrocronologiche sintonizzate alla soluzione astronomica disponibile e la precisione della Scala Temporale Astronomica (ATS) dipende strettamente dalle incertezze nella soluzione astronomica della stessa eccentricità (Laskar et al., 2004, 2011). Infatti, i cicli di eccentricità breve della Terra (~100 kyr) sono affidabili fino a ~50 Ma. Oltre questa età, il comportamento caotico di grandi corpi all'interno della fascia degli asteroidi li rende incerti (Laskar et al., 2001; Westerhold et al., 2012). Nonostante ciò, la componente dei cicli di eccentricità a lungo termine (~400 kyr) è stabile fino a ~200 Ma. L'approccio migliore per lo sviluppo di una ATS completa per il Cenozoico inferiore consiste nell'identificazione della componente periodica dei 400 kyr negli archivi sedimentari, fornendo così un potente metronomo per la calibrazione ciclostratigrafica degli archivi sedimentari e dei proxy record derivati da essi (Laskar et al., 2004; Hinnov and Hilgen, 2012).

Una scala temporale ciclostratigrafica/astrocronologica è già disponibile per gran parte del Cenozoico (Pälike and Hilgen, 2008; Hinnov and Hilgen, 2012). Tuttavia, molte sono le incertezze che caratterizzano l'ATS, dovute alla scarsità di records geochimici e magnetostratigrafici continui e ben esposti soprattutto attraverso l'EECO (McGowran, 1989 - Fig.3).

In questa tesi viene presentato un nuovo record geochimico ad alta risoluzione dell'isotopo stabile del carbonio, integrato con analisi bio- e magneto-stratigrafiche, delle classiche successioni Tetidee che affiorano nel bacino Umbro-Marchigiano (Italia) e dalla sezione Possagno situata nelle Alpi del Sud.

Lo scopo principale di questo progetto è quello di contribuire alla caratterizzazione degli eventi ipertermici attraverso l'Eocene medio-inferiore, definendo un preciso schema ciclocronologico di questi eventi accompagnato dallo sviluppo di un accurato modello di età calibrato astronomicamente.

Inoltre, contribuisce alla chiusura del gap esistente nell'ATS in corrispondenza dell'Eocene medio (Pälike e Hilgen, 2008), dovuto in parte alla scarsità di records ben preservati e continui attraverso l'intervallo ricco di silice dell'EECO (McGowran, 1989).

Sommario

L'Eocene inferiore (~56 a ~48 Ma) è registrato nelle formazioni pelagiche della Scaglia Rossa e Variegata nel bacino Umbro-Marchigiano (Italia centrale). Nel **Capitolo I** è presentato un record integrato magneto-chemo- e ciclo-stratigrafico ad alta risoluzione di due classiche sezioni Tetidee, le sezioni della Contessa Road e del Bottaccione (Gubbio, Italia centrale). La presenza di un prominente strato marnoso di 10 cm di spessore situato a ~2 m sotto il limite del magnetochron C23r-C23 è utilizzato come marker di riferimento per correlare i due affioramenti. Ciò consente di creare un record continuo ad alta risoluzione che si estende dalla parte inferiore del magnetochron C24r alla parte superiore del magnetochron C22r. L'identificazione delle componenti orbitali nel record geochimico consente di stabilire una ciclocronologia flottante dei magnetochrons e degli eventi ipertermici attraverso l'EECO, fornendo così un criterio univoco per la sua identificazione in qualsiasi interpretazione ciclostratigrafica delle successioni marine. Inoltre, il conteggio dei cicli attraverso i magnetochons C23r e C23n consente di risolvere le discrepanze tra le scale temporali basate sull'interpretazione astrocronologica e sull'età radioisotopica attraverso quello che è stato definito "intervallo problematico" da Lauretano et al. (2016).

Nel **Capitolo II** è presentata una stratigrafia integrata dell'Eocene inferiore-medio della sezione Bottaccione e del nuovo record recuperato attraverso un carotaggio effettuato a Smirra (Italia centrale). I dati ottenuti sono stati combinati con il record precedentemente pubblicato da Galeotti et al. (2017) proveniente dalla stessa area, permettendoci così di estendere il record dalla parte inferiore del magnetochron C24n alla parte superiore del magnetochron C21n. Il record risultante fornisce un quadro ciclocronologico continuo che si estende da 56.0 a 47.5 Ma. Inoltre, il nostro modello temporale è testato in modo indipendente utilizzando i profili di anomalia magnetica della superficie del mare provenienti da diversi bacini oceanici, fornendo così una prova della robustezza del nostro inquadramento astrocronologico per i primi 9 Myr dell'Eocene. Questo lavoro contribuisce ad una migliore caratterizzazione della ciclocronologia degli eventi ipertermici e alla chiusura del gap attraverso l'Eocene medio nell'ATS. Infatti, questo intervallo è ben conservato nel calcare della successione Umbro-Marchigiana.

Nel **Capitolo III** presentiamo un'analisi isotopica ad alta risoluzione dell'intervallo compreso tra l'Eocene inferiore e medio (~51-45 Ma) dalla sezione di Possagno situata nelle Alpi meridionali. La sezione fornisce una record chemostratigrafico e ciclocronologico continuo ed indisturbato attraverso un intervallo temporale critico in termini di evoluzione paleoceanografica e paleoclimatica. I record delle acque profonde disponibili forniscono un'interpretazione astrocronologica non univoca dell'intervallo di tempo analizzato,

come recentemente riportato da diversi autori (Lauretano et al., 2016; Galeotti et al., 2017; Westerhold et al., 2017). Il record di Possagno, insieme ad un carota recuperata nella stessa area, contribuisce alla definizione di una corretta interpretazione astrocronologica dell'Eocene inferiore-medio. Inoltre, il buon allineamento, sia a lungo che a breve termine, tra il record isotopo del carbonio di Possagno e records coevi, come i Siti ODP 1258, 1263, 1209 e il bacino Umbro-Marchigiano, deriva da fattori del ciclo del carbonio che si riflettono nel a livello globale.

Nel **Capitolo IV** è stata presentata la covarianza tra gli isotopi stabili bentonici del carbonio e dell'ossigeno attraverso i principali eventi ipertermici dell'Eocene inferiore, ovvero per l' ETM1 (o PETM), l'ETM2 e l'ETM3, provenienti dai records oceanici dell'Atlantico (Leg 208, ODP Sites 1262, 1263 e 1265) e del Pacifico (ODP Site 1209 - Stap et al., 2010; Lauretano et al., 2015; Westerhold et al., 2018). La linea di regressione del $\delta^{13}C$ e del $\delta^{18}O$ durante questi eventi può essere utilizzata per misurare il riscaldamento globale rispetto alla quantità totale di carbonio rilasciata, che, a sua volta, dovrebbe fornire informazioni sulla Sensibilità Climatica durante l'Eocene. Diversi autori suggeriscono che pendenze di regressione simili nei records dei foraminiferi bentonici sono state causate dal rilascio di carbonio proveniente dalla stessa fonte (Lauretano et al., 2015; Westerhold et al., 2018). Alla luce dell'evoluzione delle condizioni di background attraverso l'Eocene inferiore, proponiamo piuttosto un progressivo esaurimento nella massa di carbonio proveniente dal reservoir isotopicamente più leggero, implicando l'esistenza di più di un reservoir.

Chapter I

CYCLOCHRONOLOGY OF THE EARLY EOCENE CARBON ISOTOPE RECORD FROM A COMPOSITE CONTESSA ROAD-BOTTACCIONE SECTION (GUBBIO, CENTRAL ITALY)

Galeotti Simone, Moretti Matteo, Sabatino Nadia, Sprovieri Mario, Ceccatelli Mattia, Francescone Federica, Lanci Luca, Lauretano Vittoria, Monechi Simonetta

Published on Newsletters on Stratigraphy, Vol. 50/3 (2017), 231–244,
DOI: 10.1127/nos/2017/0347.

ABSTRACT: High-resolution geochemical time series from the composite Contessa Road-Bottaccione (CR-BTT) section (central Italy) allows testing the global significance of Early Eocene short- and long-term carbon isotope trends by comparison with available records from oceanic successions. Spectral analysis reveals Milankovitch frequency band fluctuations in the concentration of $CaCO_3$. Extraction of the short- and long- eccentricity orbital periodicities from the wt.% $CaCO_3$ record provides a relative cyclochronology for the interval spanning ~49.5 Ma to ~52.5 Ma corresponding to magnetochron C22r to the top of C24n thus extending the cyclochronology already available from the same section in the interval between ~52.0 to ~56 Ma, spanning the lower C24r to upper C23r. Recognition of orbitally forced sedimentary cycles, corresponding to the long (405 kyr) and short (100 kyr) eccentricity, allows to test the chemostratigraphic alignment with ODP Site 1258 and ODP Site 1263 records and to obtain a correlation of hyperthermal events to an unambiguous magnetostratigraphic record across the interval corresponding to the Early Eocene Climatic Optimum and to refine the astrochronological interpretation of the Ypresian Stage.

1.1 INTRODUCTION

The Early Eocene Climatic Optimum (EECO) recorded the highest mean global temperature of the last 65 millions of years (Myr) (Zachos et al., 2001, 2008). Geochemical and paleontological proxies indicate that high latitude temperatures were much higher than present day with peaks of 15–23°C (Zachos et al., 2010; Huber and Thomas, 2008). Deep-water temperatures were 10–12°C higher than present day, depressing the meridional gradient and the efficiency of global oceanic circulation (Zachos et al., 2001; Huber and Caballero, 2011). The extreme climate of the EECO represents a case study for the so-called super-greenhouse state under very high atmospheric CO_2 concentrations (Pagani et al., 2005). According to Lunt et al. (2011), the EECO is the maximal expression of a series of transient warming events called hyperthermals that punctuated the long-term warming trend starting in the middle Paleocene around 60

million years ago (Ma) and culminating at ~51 Ma. Hyperthermals are geologically brief (10^4–10^5 yr) events characterised by large global temperature increase and negative carbon isotope excursions, caused by the release of massive amounts of isotopically light carbon into the exogenic pool (Zachos et. al., 2005; Lourens et al., 2005; Röhl et al., 2007; Agnini et al., 2007; Nicolo et al., 2009). It has been suggested that these events were triggered by orbital forcing (Cramer et al., 2003; Lourens et al., 2005; Galeotti et al., 2010; Littler et al., 2014; Lauretano et al., 2015). The most important hyperthermal events are represented by the Paleocene–Eocene Thermal Maximum (PETM) at ~56.1 Ma (Kennett and Stott, 1991; Koch et al., 1992; Nicolo et al., 2007; Zachos et al., 2005; Galeotti et al., 2010; DeConto et al., 2012), the Eocene Thermal Maximum 2 (ETM2), at ~54.1 Ma, and the ETM3 at ~52.8 Ma (Cramer et al., 2003; Lourens et al., 2005; Westerhold et al., 2007; Galeotti et al., 2010). Proposed carbon sources for the emplacement of these events on an orbital time scale include oceanic gas hydrates (Dickens et al., 1995), oceanic dissolved organic carbon (Sexton et al., 2011, Kirtland Turner et al., 2014) and permafrost (DeConto et al., 2012). According to Lunt et al. (2011) changing mean boundary conditions across the gradual warming that culminates at the EECO, resulted in diminished magnitude and increasing frequency of hyperthermal events, in response to the climate system getting closer to the threshold for carbon release and decreasing time for the recharging of the gas hydrate reservoir. The scarcity of well-preserved and continuous geochemical records across the early Eocene, particularly across the silica-rich EECO interval (McGowran, 1989) makes it difficult to obtain an observational basis to test this hypothesis. In fact, a univocal cyclostratigraphic interpretation across this interval (problematic interval of Lauretano et al., 2016) has proved to be a challenging task to achieve. Here we present an integrated magneto-, chemo- and cyclo- stratigraphic record from the Bottaccione-Contessa Road composite section, which provides an exceptionally well-preserved archive of orbital forcing signature across this critical interval.

1.2 MATERIAL AND METHODS

1.2.1 The Contessa Road-Bottaccione composite section

Outcrops in the Umbria–Marche Basin of central Italy provide a continuous record of the Paleocene and Early Eocene, which is locally preserved in the pelagic red limestones of the Scaglia Rossa Formation. Well-known early Cenozoic sections in the classic Gubbio area were used to develop magneto- and biostratigraphic relationships that enabled the first calibration of geomagnetic reversals for most of the Paleogene interval (Lowrie et al., 1982; Napoleone et al., 1983). Here we focus on two sections, Contessa Road (lat. 43°22 47 N; long. 12°33 50 E) and Bottaccione (lat. 43° 21 56 N; long. 12° 34 57 E - Fig. 1.1) to build a composite, stratigraphically continuous succession spanning the lower part of magnetochron C24r to the lower part of magnetochron C22r.

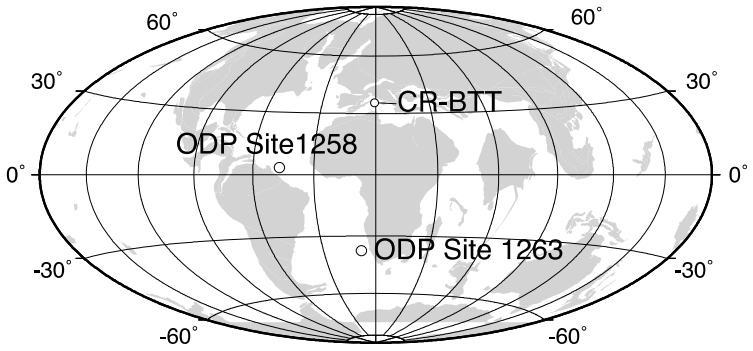

Figure 1.1*: Paleogeographic reconstruction for the Early Eocene (51 Ma) showing the location of the three sites discussed in text. Paleogeographic map is from the Ocean Drilling Stratigraphic Network Plate Tectonic Reconstruction Service: (http://www.odsn.de/odsn/ services/paleomap/paleomap.html).*

The 54.5m-thick Contessa Road section starts at the Cretaceous-Paleogene (K/Pg) boundary, defined as level 0 in the measured section. Previous bio- and magnetostratigraphy of the lower Paleogene portion of the Contessa Road section, which is locally represented by the Scaglia Rossa limestones and marly limestones, have been published by Lowrie et al. (1982) and Galeotti et al. (2000, 2005) from ca. 24 m above the K/Pg boundary to the top of the section at 54.5 m above the K/Pg boundary. The integrated bio-, magneto- and chemostratigraphic analysis of the upper Paleocene to lower Eocene (Galeotti et al., 2010; Coccioni et al., 2012) reveals the occurrence of carbon isotope excursions (CIEs) associated to hyperthermal events as previously described from oceanic successions. A more detailed description of the lower Eocene Contessa Road is given by Galeotti et al. (2000, 2010). The outcrop is poorly exposed from the top of C23r magnetochron, which does not allow an accurate high-resolution sampling. In order to extend the high-resolution geochemical record already available for the Early Eocene at the Contessa Road section (Galeotti et al., 2010), we sampled the overlying stratigraphic interval in the nearby Bottaccione section. In particular, the record of Galeotti et al. (2010), spanning 31.3-47 m above the K/Pg boundary in the Contessa Road section, has been extended by sampling the interval spanning 47-54 m above the K/Pg in the Contessa Road record and 50.2-63.6 m above the K/Pg boundary in the Bottaccione section (see also Fig. 1.2). The lower–middle Eocene at Bottaccione has been previously studied for bio- and magnetostratigraphy by Napoleone et al. (1983). The studied interval is mainly calcareous although a series of marly layers, up to 10 cm-thick, occur, particularly in its lower part. Chert nodules and layers are also present although sparse.

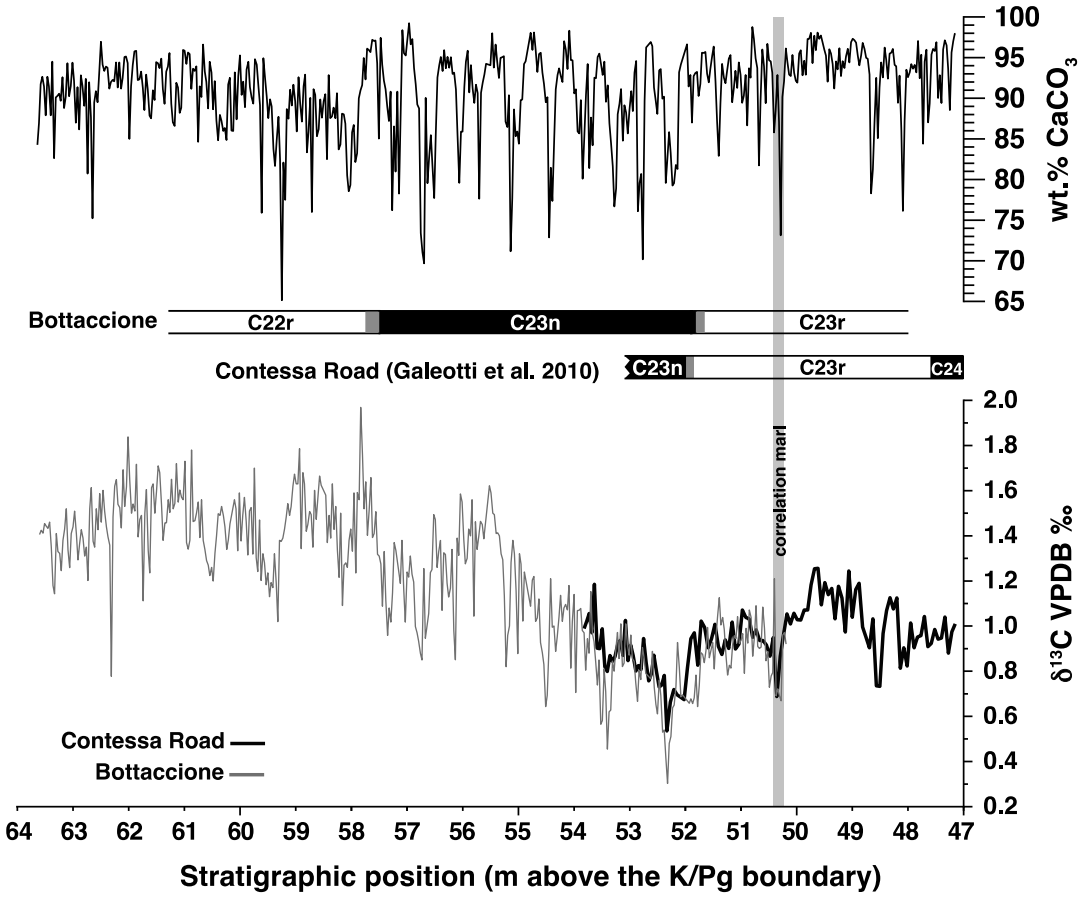

***Figure 1.2**: Wt.% $CaCO_3$ and $\delta^{13}C$ records from the Contessa Road-Bottaccione composite section plotted against the magnetostratigraphy of both sites. The shaded band represents the marly layer used as a lithostratigraphic marker for the correlation between the two sections.*

1.2.2 Magnetostratigraphy

A magnetostratigraphic record of the Contessa Road section up to the lower part of Chron C23n is presented in Galeotti et al. (2010). A highly resolved magnetostratigraphic record was constructed on closely spaced (~25 cm on average) samples taken at Bottaccione in an interval spanning 1.5 m below the marly marker bed to 12.4 m above it, for a total of 61 samples, allowing a precise identification of reversal boundaries with respect to wt.% $CaCO_3$ and stable isotope stratigraphy in the surveyed interval. Measurements followed standard paleomagnetic procedures, the primary magnetization was isolated from the viscous overprint using principal component analysis after stepwise thermal demagnetization at temperature higher than 350°C. All samples gave a reliable paleomagnetic direction, with antipodal directions that pass a reversal test at the 95% confidence level (Normal Direction: 315.4, 38.7, k = 23.56, N = 29; Reversed

Direction: 142.7, –35.9, k = 23.37, N = 50). The tilt-corrected mean Fisher direction (320, 37, a95 = 3.4) is virtually identical to that reported by Napoleone et al. (1983). Magnetic polarity was interpreted after calculation of the virtual geomagnetic polarity latitude.

1.2.3 Geochemistry

Wt.% $CaCO_3$ contents have been measured in a total of 234 samples from the Contessa Road section and 433 samples from the Bottaccione section using a "Dietrich-Frühling" calcimeter with a precision of measurements, based on replicate analyses, within 1%. Sampling resolution was about one sample every 3 cm with a few exceptions across cherty layers where sample resolution was about ~7 cm.

Stable isotope analyses have been carried on bulk samples from the upper part (47.23–54.19 m) of the Contessa Road section encompassing the correlation marl at 50.25 m. Across this interval stable isotope analysis has been conducted on the same sample set used for the analysis of wt.% $CaCO_3$ although with a resolution of 6 cm for a total of 117 sample. The Bottaccione section was sampled at a resolution of 3 cm for a total of 433 bulk samples. Stable isotope analysis was performed at the IAMC–CNR laboratory (Capo Granitola, Italy) using an automated continuous flow carbonate preparation GasBenchII device and a ThermoElectron Delta Plus V Advantage mass spectrometer on powdered bulk rock samples after heating them at 400°C to remove organic components. Replicate analysis provides a precision within 0.06‰. Carbon isotopes values are calibrated to the Vienna Pee Dee Belemnite standard (VPDB) and converted to conventional delta notation ($\delta^{13}C$).

1.2.4 Spectral analysis

Wavelet analysis of the wt.% $CaCO_3$ record was used to compute the evolutionary spectrum in the depth domain using the Wavelet Script of Torrence and Compo (1998) and Morlet mother wavelet with an order of 6.

Further, a power spectrum analysis of the $CaCO_3$ was conducted using a 2π-Multi Taper Method (MTM) with 3 tapers following the method of Ghil et al. (2002). Confidence levels are based on a robust red noise estimation (Mann and Lees, 1996). Moreover, Evolutive Harmonic Analysis (EHA) has been performed on the Contessa Road-Bottaccione (CR-BTT) composite section across the interval that corresponds to the problematic interval defined by Lauretano et al. (2016), to recognise the frequency modulation of the eccentricity components following the method described in Laurin et al. (2016).

1.3 RESULTS

1.3.1 Magnetostratigraphy

An integrated stratigraphic record of C25n–C23n interval of the Contessa Road record, including bio- and magnetostratigraphy is discussed in Galeotti et al. (2000, 2010). Napoleone et al. (1983) published a bio- and magnetostratigraphic record of the Bottaccione Eocene. Identification of the original meter marks used

by the latter authors in the field, allows a straightforward comparison of our new magnetostratigraphic record with the available bio- and magnetostratigraphy (Napoleone et al., 1983). Accordingly, the obtained paleomagnetic record is very similar to that of Napoleone et al. (1983). In particular, we identify two reversals between 51.7–51.8m and 57.5–57.75m above the K/Pg boundary (Fig. 1.2). The ~5.9 m-thick normal polarity interval delimited by these two reversal clearly corresponds to the C23n magnetochron identified by Napoleone et al. (1983) between ~410-415 m depth of the original lithostratigraphic log of Arthur and Fischer (1977), that is ~8 m above the lower boundary of the cherty member of the Scaglia Rossa. Unfortunately, we were not able to identify the short reversal separating C23n.1n from C23n.2n. Because of minor uncertainties in the positioning of the base of C23n at both sites due to the average sampling resolution of magnetostratigraphic samples (~25 cm), we use a prominent, 10 cm-thick marly layer in an otherwise calcareous interval, laying ~2 m below the C23r–C23n magnetochron boundary, whose base is at 50.25 m above the K/Pg boundary in the Contessa Road section, as a marker bed to correlate the two outcrops (Fig. 1.2).

On the other hand, a lithostratigraphic correlation between the two sites can be easily done using distinctive marly intervals and other prominent marly layers that occur in both sections. Comparison of high-resolution carbon isotope records across the supposed overlap interval in both sections validates the litho- and magnetostratigraphic correlations. The $\delta^{13}C$ record from the two sites shows an optimal match that allows to confidently obtain a composite section with a precision in the range of sample resolution adopted for the geochemistry, i.e. 3 cm (Fig. 1.2).

The resulting composite section allowed us to extend the high-resolution record of Galeotti et al. (2010) to the lower C22r magnetochrons by adding a ~10 m-thick segment sampled at Bottaccione.

1.3.2 Geochemical records

The lower Eocene of the Contessa Road section is characterized by a series of CIEs and concomitant dissolution levels corresponding to the well know succession of early Eocene hyperthermal events, including the Eocene Thermal Maximum 1 (ETM1 or PETM), ETM2 and ETM3 (Galeotti et al., 2000, 2010; Coccioni et al., 2012). In this paper we extend the record of Galeotti et al. (2010) to the lower part of magnetochron C22r, across the stratigraphic segment spanning ~47– 63 m above the K/Pg boundary from the Bottaccione section (Fig. 1.2).

Similar to what is observed across the C24r-C23r interval from the Contessa section (Galeotti et al., 2010), the wt.% $CaCO_3$ record shows a large variability ranging from ~70% to ~98% (Fig. 1.2).

Lowest carbon isotope values are observed at the C23r/C23n boundary where the well-known gradual decline of carbon isotope values, characterising the Early Eocene (Zachos et al., 2008), ends. In this interval the $\delta^{13}C$ values range from ~0.3‰ to ~2.0‰, with a rapid rise observed in the middle part of Chron C23n. From here upwards, mean $\delta^{13}C$ is ~1.43‰, which is ~ 0.4‰ higher than in the preceding interval. A similar

increase in the corresponding stratigraphic interval has also been reported by Hilting et al. (2008) based on the analysis of a global stack of benthic data from oceanic records. Moreover, the C23n magnetochron interval is characterized by a series of CIEs (up to 0.6 ‰) similar to those reported for the same age interval at ODP Site 1258 (Demerara Rise) (Kirtland Turner et al., 2014) and ODP Site 1263 (Walvis Ridge - Lauretano et al., 2016).

Notably, as seen in the wt.% $CaCO_3$ record, an interval of increased variance is observed in the $\delta^{13}C$ record across the C23n magnetochron interval. In particular, the $\delta^{13}C$ time series shows a variance of ~0.09‰ across the C23n interval, which is 5 times larger than observed in C23r. Comparison between carbon isotope and wt.% $CaCO_3$ records clearly shows that CIEs correspond to carbonate depleted intervals (Fig. 1.2), suggesting dissolution or dilution across CIEs similar to what observed across hyperthermal events in deeper or marginal settings, respectively.

1.3.3 Spectral analysis

Wavelet analysis of the wt.% $CaCO_3$ record from the CR-BTT composite section reveals that spectral power greater than the 95% confidence limit is confined to distinct frequency intervals with periods of ~23 cm, ~50–60 cm and ~200 cm (Fig. 1.3). A decrease in the frequency of the periodic components - centred at about 55 cm - is evident in the wavelet spectrum at ~55 m above the K/Pg boundary, suggesting a corresponding increase in sedimentation rate of the Scaglia limestones. As already evidenced by Galeotti et al. (2010), much power is confined to a frequency interval corresponding to a period of ~5 m in the lower Eocene Contessa Road record, increasing to ~6 m in the surveyed interval.

The MTM analysis confirms the results obtained with the wavelet method, providing evidence for distinct spectral peaks above the 95% confidence limit at frequency bands centered at ~1.8, ~4.5 and between ~7–11 cycle/m, which correspond to a period of ~0.55 m, ~0.22 m and ~9–14 cm, respectively. Distinct peaks are also observed at frequencies 0.5 cycle/m and 0.18 cycles/m, thus corresponding to the components with a period of ~ 2 m and 5–6 m, respectively, in the wavelet spectrum (Fig.1.4).

Figure 1.3*: Evolutionary wavelet analysis for wt.% $CaCO_3$ values from the CR-BTT composite section for the interval spanning from 47 to 61 m above the K/Pg boundary and magnetostratigraphy (upper panel). White contours indicate the 99% significance level. Lower panel: wavelet spectrum based on the Fe record from ODP Site 1258 (Westerhold and Röhl, 2009). White contours indicate the 95% significance level. Note the transition to a short eccentricity dominated interval in correspondence to C23n, marked by a red dashed line in both spectra. Notice the transition from a long eccentricity (LE) dominated interval to a short eccentricity (SE) dominated interval at the transition between magnetochrons C23r–C23n at both sites.*

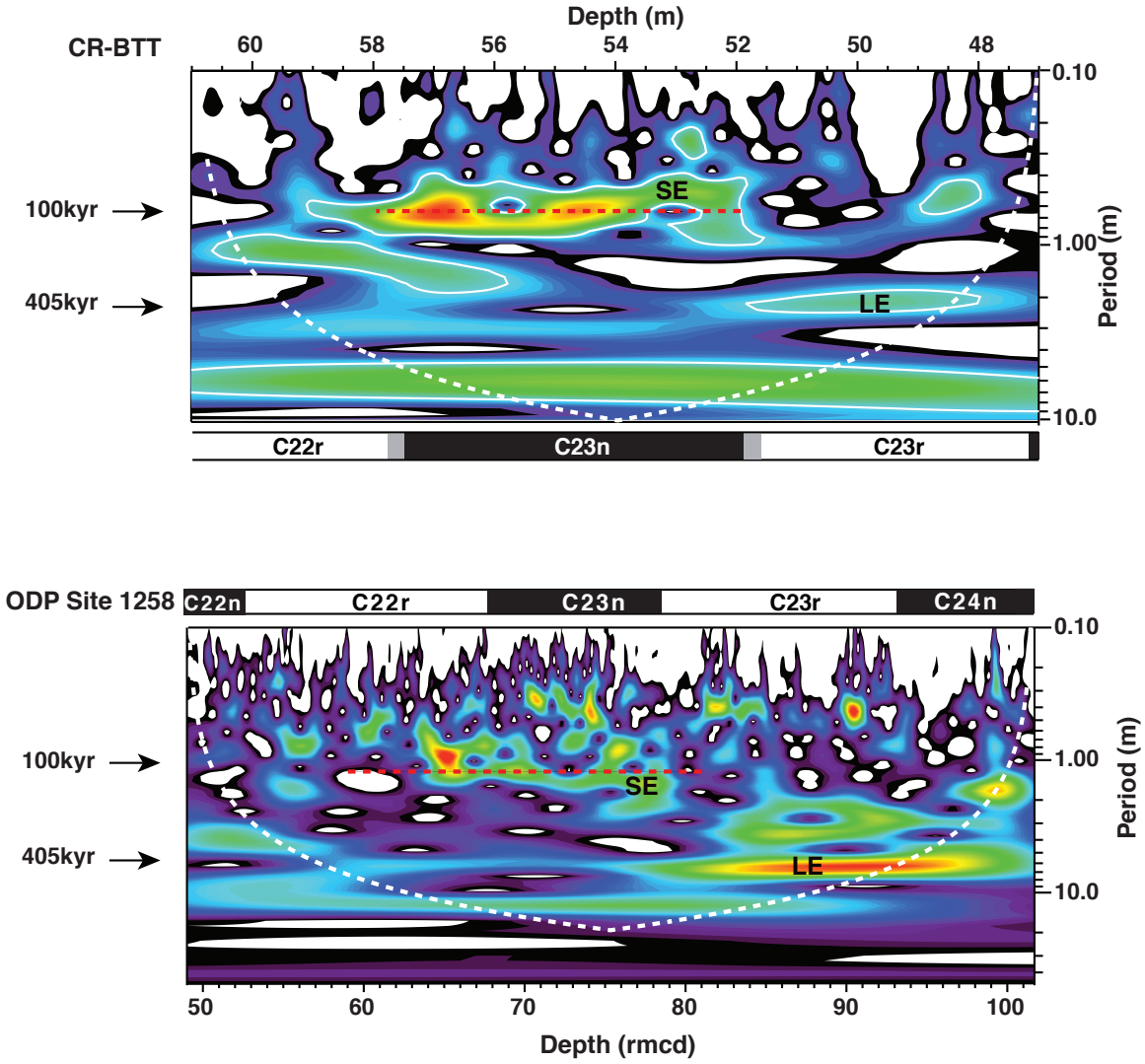

***Figure 1.4**: MTM spectrum of the wt.% $CaCO_3$ record from the CR-BTT composite section. Gray lines indicate 90%, 95% and 99% confidence levels.*

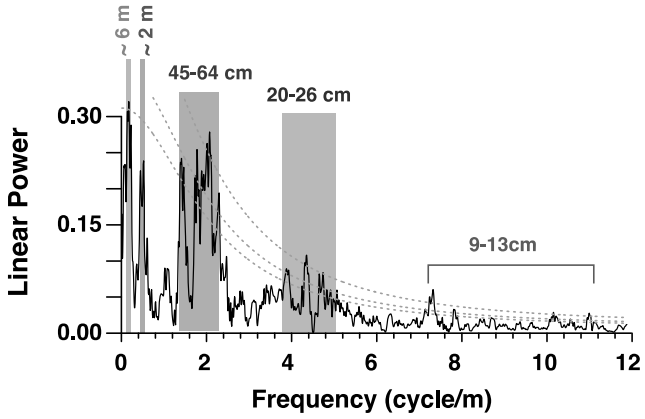

1.4 DISCUSSION

1.4.1 Cyclochronology of the CR-BTT composite section

Both MTM and wavelet analyses provide evidence for the occurrence of periodic components in the wt.% $CaCO_3$ record of the surveyed interval similar to the interval spanning the PETM to the lower part of C23r, which was deposited at a sedimentation rate of ~0.5 cm/kyr based on the cyclochronology (Galeotti et al., 2010). A similar sedimentation rate value is obtained for the 10 m-thick C23 magnetochron (Fig. 1.2), which according to Vandenberghe et al. (2012) spans ~2 Myr. On this basis, the periodic component recognised through wavelet and MTM spectral analysis can be ascribed to orbital forcing. In particular, the peak with a period centred at ~55cm corresponds to the 100 kyr eccentricity; the peak centred at 22 cm corresponds to obliquity. Moreover, the peaks spread over a frequency range spanning ~7–11 cycle/m are in the precession band.

On the same basis, the large spectral density peaks with periods of ~2m and ~6m correspond to ~400kyr and 1.2Myr. The latter term has already been evidence in the lower Eocene Scaglia Rossa at Gubbio and attributed to a long-term beat of obliquity (Galeotti et al., 2010; DeConto et al., 2012).

The power of these two peaks remains below the 90% confidence limit in the MTM spectrum possibly due to the fact that much power is confined to the short eccentricity component, particularly across C23n, as revealed by the wavelet evolutionary spectrum. However, both peaks are above the 95% confidence limit in the wavelet spectrum. Filtering of the long eccentricity components, hence, can be used to astronomically tune the CR-BTT composite record.

1.4.2 Correlation with ODP Site 1258 and ODP Site 1263

The bulk carbon isotope record from the CR-BTT composite section can be compared to the bulk $\delta^{13}C$ record from ODP Site 1258, Demerara Rise (Kirtland Turner et al., 2014) and the benthic $\delta^{13}C$ record from ODP Site 1263, Walvis Ridge (Lauretano et al., 2016). Minor differences in the positioning of individual CIEs with respect to magnetostratigraphy are observed between our record and ODP Site 1258. In particular, C23rH3, or N of Lauretano et al. (2016), which can be easily identified as it occurs at the end of a longer-term decreasing trend in carbon isotope values, falls at the top of C23r at Site 1258 (Kirtland Turner et al., 2014), whereas it is positioned within the lower C23n at Gubbio (Fig. 1.5).

Moreover, the C22rH1 event, or Q according to Lauretano et al. (2016), which occurs at the base of C22r at Site 1258 (Kirtland Turner et al., 2014), falls at the top of C23n at Gubbio (Fig. 1.5).

Unfortunately, no magnetostratigraphy is available from Site 1263 to unravel these minor discrepancies. However, the alignment of the three records is relatively straightforward, which provides a solid basis for chemostratigraphic correlation of the three sites, hence for testing the cyclochronological interpretations

adopted by different authors. This is particularly relevant for the so-called "problematic interval" as defined by Lauretano et al. (2016) whose cyclochronological interpretation is still debated. Different interpretations of the number of orbital cycles within individual magnetochrons (particularly the upper C23r and C23n) obviously impact the cyclochronology of the subtended hyperthermal events and the interpretation of their phasing with respect to long-term modulation(s). As reported by Lauretano et al. (2016), the comparison of astronomical and radio-isotopic age models, available in the Geologic Time Scale 2012 (GTS2012) for this time interval, reveals a large discrepancy in the interpretation of the duration of magnetochron C23n, which results in a propagation of a ~0.5 Myr offset between the two age models up to Chron C21r (Vandenberghe et al., 2012). One possibility is that cycle counting across the problematic interval, and particularly within C23n, has been incorrectly carried out, although problems related to intersite magnetostratigraphic correlation cannot be excluded. The CR-BTT composite section provides an excellent integrated magnetostratigraphic and carbon isotope record, which can be directly compared to existing orbitally tuned time series. The problematic interval spans 266–253mcd at ODP Site 1263 (Lauretano et al., 2016). Chemostratigraphic correlation based on the alignment of $\delta^{13}C$ records allows to clearly identify the same interval at ODP Site 1258 where it spans 86-71 rmcd, thus the lower Chron C23r to lowermost of subchron C23n.1n (Lauretano et al., 2016) (Fig. 1.5). Based on the cyclochronological interpretation of Site 1258 by Westerhold and Röhl (2009), the problematic interval contains two 405-kyr eccentricity maxima. Lauretano et al. (2016) have later revisited the cyclochronology of magnetochron C23r–C23n by testing three different age models that include one, two or three 405-kyr maxima within the problematic interval, respectively. They conclude that the cyclochronological interpretation of Westerhold and Röhl (2009) was the most plausible based on the observation that the other two options would entail changes in sedimentation rate, for which there is no evidence at both sites. However, the cyclochronological interpretation of the problematic interval is not straightforward, particularly because of a weak signal in the long-eccentricity band – possibly related to a minimum in the 2.4 million-long modulation of eccentricity across it (Westerhold and Röhl, 2009).

Figure 1.5*: Chemostratigraphic ($\delta^{13}C$) and magnetostratigraphic correlation of the CR-BTT composite section with ODP Site 1263 (Lauretano et al. 2016) and ODP Site 1258 (Kirtland Turner et al. 2014). The red dashed line box represents the "problematic interval" as identified by Lauretano et al. (2016) at ODP Site 1263. The grey bands correspond to CIEs. The latter are labelled according to Kirtland Turner et al. (2014) on the ODP Site 1258 record. We use the labelling of Cramer et al. (2003) and Lauretano et al. (2016) for the CR-BTT record.*

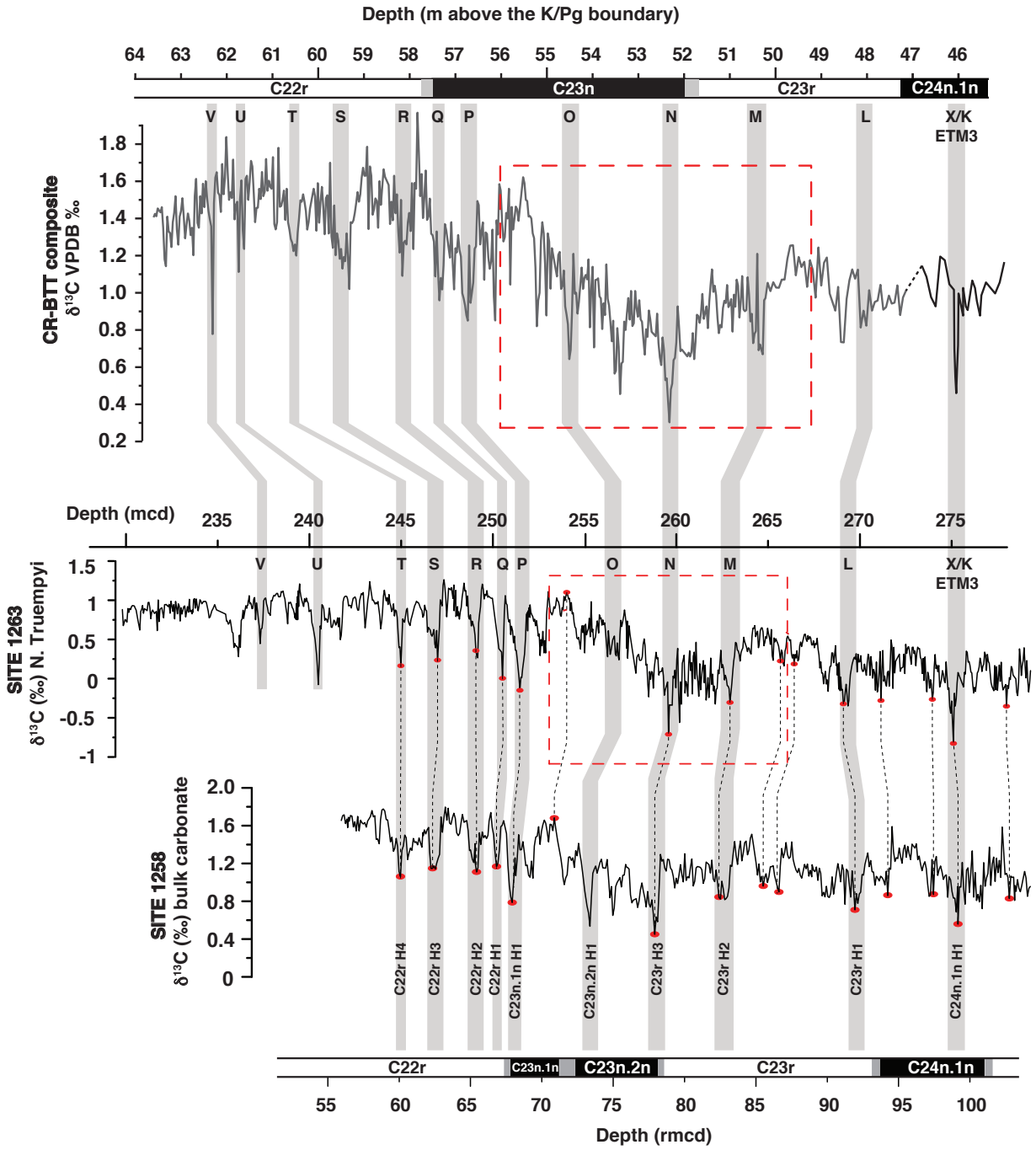

In order to overcome this problem, we complement the method used by Westerhold and Röhl (2009) and Lauretano et al. (2016) which are based on cycle counting and the observation of their amplitude modulation (AM) with the analysis of frequency modulation (FM) of the short eccentricity component as recently done by Laurin et al. (2016) in the lower Eocene Contessa Road record (Fig.1.6).

We first identify the problematic interval in the CR-BTT composite succession by aligning our carbon isotope record to those from ODP Sites 1258 and 1263. On this basis, the problematic interval spans 49.2-

56 m above the K/Pg Boundary in our record (Fig. 1.5). The chemostratigraphic correlation is relatively easy as the problematic interval starts between two prominent CIE corresponding to events L (Cramer et al., 2003) and M (Lauretano et al., 2016) (Fig. 1.5) corresponding to the middle C23r. To determine a short eccentricity-based cycle counting within the problematic interval, we filter the 0.55 m period component, which corresponds to ~100 kyr from the wt.% $CaCO_3$ record using a Gaussian filter centred at the frequency of 1.8 cycle/m with a bandwidth of ±15%. The filtered component shows a clear modulation of the long eccentricity (Fig. 1.6), as expected based on theoretical models of astronomical forcing (Laskar et al., 2011). Within the problematic interval (shaded area in Fig. 1.6) we count 13 short eccentricity cycles with peaks of maximal AM at 48, 50, 52, 54.5 and 57m suggesting an increase in sedimentation rate between 52 and 54.5 m, in line with the results obtained by wavelet spectral analysis. This result provides evidence for the presence of three 405-kyr maxima within the problematic interval that, based on our cycle counting, has a total duration of ~1.2 Myr. The evolutive harmonic spectral analysis carried out on the wt.% $CaCO_3$ record provides a clear identification of the FM of the two components of short eccentricity (E2 and E3 in Fig. 1.6) for the upper part of the surveyed interval, where nodes of minimal modulation are observed at ~53, ~56 and ~ 58.5 m. The lower part of the analysed segment, between 46–51 m, shows a less distinct FM signal although nodes of minimal modulation can be identified at ~47, ~49 and ~51 m, therefore between peaks of maximal AM detected in the filtered short eccentricity component. This exercise confirms the difficulties in thoroughly determining the number of long-eccentricity cycles within the problematic interval, as reported by Lauretano et al. (2016), largely because of the weaker amplitude modulation across a 2.4 Myr node (Laskar et al., 2011). However, the documentation of AM and FM provides univocal evidence for the identification of 405 kyr maxima. We conclude that, in spite of the less distinctive character of the FM signal in the lower part of the problematic interval, the integrated observation of the AM and FM provides evidence for the presence of three 405 kyr maxima within the "problematic interval", differently than suggested by Westerhold and Röhl (2009) and the 2-cycle age model by Lauretano et al. (2016), but in agreement with the 3-cycle age model by Lauretano et al. (2016).

Figure 1.6*: Results of the spectral analysis of magnetochrons C23r–C23n (A) encompassing the 'problematic interval' in the CR-BTT composite section. B) wt.% $CaCO_3$ record; C) filter of the ~0.5 m-long periodic component of the wt.% $CaCO_3$ record, corresponding to short eccentricity. Eccentricity maxima correspond to wt.% $CaCO_3$ minimum values (Galeotti et al., 2010). The amplitude modulation of the short eccentricity component allows to identify maximal modulation peaks of the 405-kyr eccentricity indicated by the arrows (D), counted starting from maximum 9, which corresponds to event L of Cramer et al. (2003) following Westerhold and Röhl (2009) and Lauretano et al. (2016). E) Evolutive MTM spectrum of the wt.% $CaCO_3$ record. The trace of the E2+E3 signal exhibits systematic alternations of intervals of positive and negative interference, in the upper part of the section. These junctions and bifurcations exhibit the same rhythm as the long-eccentricity modulation of the ~0.5 m filter and are therefore interpreted as maxima and minima, respectively, of the 405-kyr eccentricity cycle. The E2+E3 signal is poorly distinguishable in the interval 46–50 m, coincident with a minimum in the very long-term cycle of*

eccentricity modulation in La2010d (Westerhold et al. 2012). The shaded area represents the extent of the problematic interval defined by Lauretano et al. (2016).

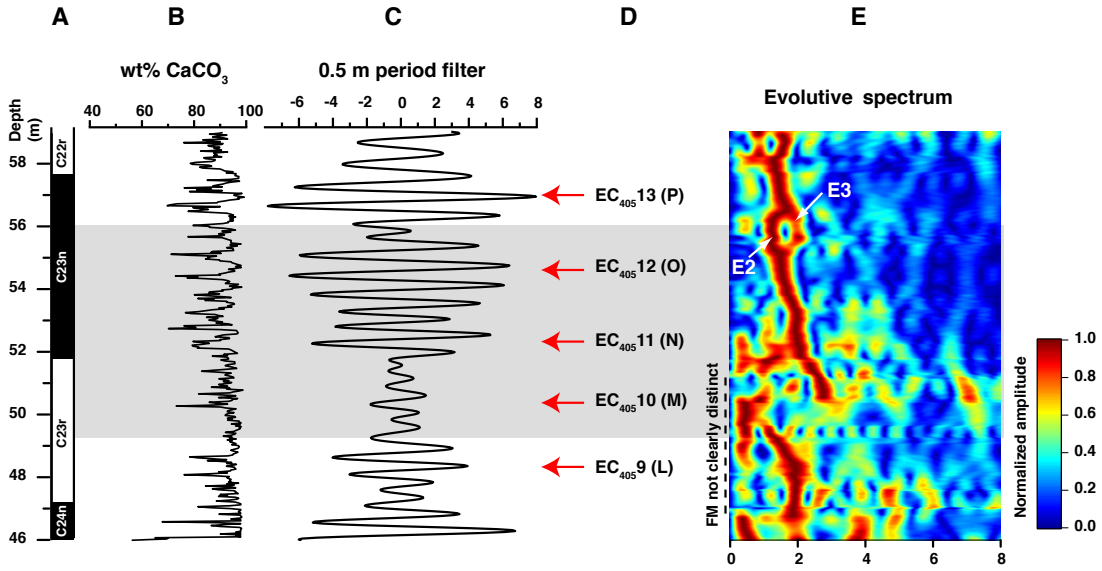

1.4.3 Implications for the astrochronological interpretation of the early Eocene

The detection in the Early Eocene from the Scaglia Rossa at Gubbio of a different number of 405-kyr cycles than previously proposed by Westerhold and Röhl (2009) and according to the 2-cycle option by Lauretano et al. (2016) has obvious implications for the cyclochronology of the surveyed interval. According to Westerhold and Röhl (2009), C23n has a cyclochronological duration of ~675 kyr. The cyclochronological analysis of the CR-BTT composite record, allows to identify ~10.5 short eccentricity cycles within C23n. Assuming an average duration of 105 kyr for short eccentricity, we estimate a total duration of C23n of ~1.1 ±0.05 Myr considering the uncertainties in the positioning of the magnetochron boundary. Our estimate, therefore, is in line with that of Cande and Kent (1995) and Vandenberghe et al. (2012) and largely differs from that of Westerhold and Röhl (2009) based on the cyclochronology of ODP Site 1258. However, our estimate of the duration of C23r, which is ~840 ±50 kyr based on counting short eccentricity cycles, is in line with the estimate provided by Westerhold and Röhl (2009), who suggested a duration of ~800 kyr for this magnetochron.

In order to provide an astrochronological estimate of the absolute age of different events observed in the CR-BTT composite, we filter the long eccentricity component (period of ~2 m) using a Gaussian filter centred at a frequency of 0.55 cycles/m with a bandwidth of ±15% and tune it to the La2010d astronomical solution (Laskar et al., 2011). As a tie point for the tuning we use an absolute age estimate of 54.09 Ma for ETM2 (Westerhold et al., 2007, option 2). Based on the cyclochronological record of the Contessa Road section (Galeotti et al., 2010), this age propagates to an absolute age of 52.62 Ma for the upper boundary

of Chron C24n (Fig. 1.7). Considering a total duration of ~170 kyr for the associated geochemical anomaly (Röhl et al., 2007), the inferred age for the onset of the PETM is ~56.1 Ma, which is midway between the terrestrial calibration of this chronohorizon from the Green River Formation (Tsukui and Clyde, 2012) that provides an age of 56.33 Ma for the P/E boundary, and the most recent radioisotopic U/Pb age of 55.83 ±0.1 Ma from bentonite layers within the PETM interval at Spitzbergen (Charles et al., 2011). Combined with the assumption that the Paleocene Epoch spans 24.5 long (405 kyr) eccentricity as recently suggested by cyclostratigraphic analysis of land-based and oceanic successions (Hilgen et al., 2010; Dinarès-Turell et al., 2014; Galeotti et al., 2015), our observation suggests an age of ~66.02 Ma for the K/Pg boundary, which matches the astrochronological estimate of 66.0225 ±0.0040 Ma provided by Dinarès-Turell et al. (2014) and the $^{40}Ar/^{39}Ar$ radio- isotopic age of 66.043 ± 0.043 Ma (Renne et al., 2013) for this chronohorizon.

The duration of individual magnetochron, and the absolute age of CIEs and magnetochron boundaries obtained after tuning the record to the La2010d solution are reported in Table 1.1 and Table 1.2, respectively. In general, the cyclochronological estimate of the magnetochron duration is in line with estimates reported in the Geological Polarity Time Scale (GTS) 2012 (Ogg, 2012; Vandenberghe et al., 2012). As already discussed, we find major discrepancies with the estimate of the duration of C23n provided by Westerhold and Röhl (2009) and Lauretano et al. (2016) for Site 1258. However, particularly when the uncertainties implied in the positioning of individual magnetochrons and subchrons are considered, there is a rather satisfactory match between our estimate and those reported in Westerhold and Röhl (2009) for the interval spanning C24n and C23r. The cyclochronological estimate of the duration of magnetochron reported by Tsukui and Clyde (2012) is systematically shorter than what we observe in the CR-BTT composite record. Chemostratigraphic correlation between our record and ODP Site 1258 (Fig. 1.5) provides independent evidence that the large discrepancy between our estimate of the duration of C23n compared to what reported by Westerhold and Röhl (2009) can be to a very minor extent attributed to the problematic positioning of C23n at that Site (Suganuma and Ogg, 2006). Combined magnetostratigraphy and chemostratigraphy, in fact, suggest that the inconsistency between the two sites is limited to a minor (100 kyr) difference in the positioning of CIE C22r H1 relative to magnetochron C23n. We, therefore, conclude that the observed large discrepancy is due to a different cyclochronological interpretation across the problematic interval.

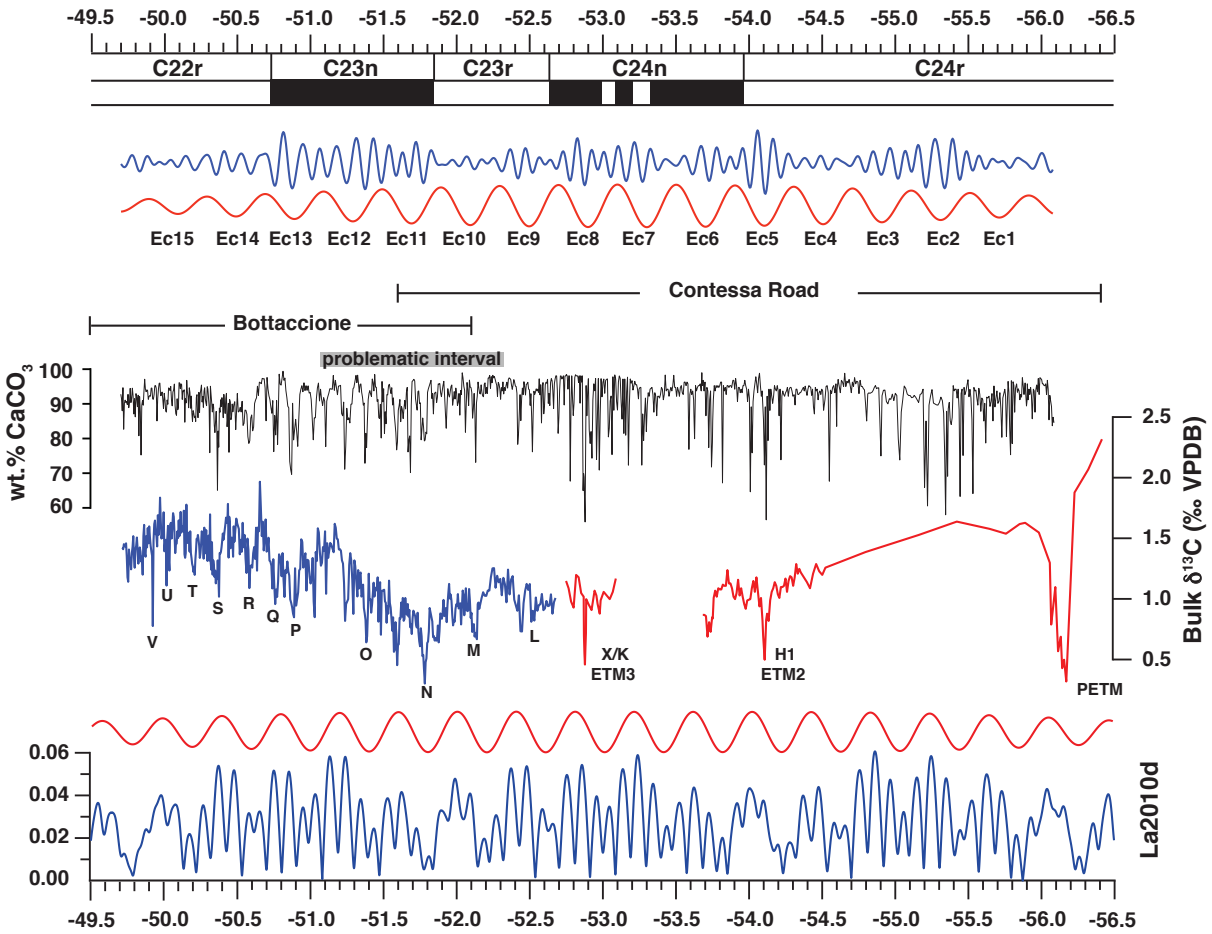

***Figure 1.7**: Astrochronological calibration of the CR-BTT record. The tuning has been carried out using the ~2 m-long periodic component corresponding to the 405-kyr eccentricity. From top to bottom: Magnetostratigraphy of the CR-BTT record; Filters of the short (blue line) and long (red line) eccentricity; wt.% $CaCO_3$ and $\delta^{13}C$ records from the CR-BTT composite section. The interval analysed by Galeotti et al. (2010) corresponds to the red lined carbon isotope record; the 405-kyr (red line) and short (blue line) eccentricity component extracted from the La2010d astronomical solution (Laskar et al., 2011). The duration of the geochemical anomaly associated to the PETM is based on Röhl et al. (2007) as we have not carried out a cyclochronological analysis of the corresponding interval at Gubbio.*

	CK95	GTS2012			WR09	TC2012	Lauretano et al. (2016)		This study	
		astro	radio	combined			2 cycles	3 cycles	Tuning	Cycle counting
C23n	965	675	1210	1210	675	930	509	676	1180	1120
C23r	621	800	790	790	800	570	781	1016	760	840
C24n.1n	299	390	380	450	390	270	458	458	390	420
C24n.1r	94	125	120	130	125	110	162	162	90	
C24n.2n	44	75	60	80	75	50	67	67	100	
C24n.2r	102	142	130	140	142	110	142	142	130	
C24n.3n	444	567	560	570	567	500	561	561	650	630
C24n $_{(total)}$	983	1299	1250	1370	1299	1040	1390	1390	1360	1417

***Table 1.1**: Estimated duration (kyr) of individual magnetochrons for the surveyed interval according to different authors: CK95 = Cande and Kent (1995); GTS2012 = Geological Time Scale 2012 (Vandenberghe et al. 2012); WR09 = Westerhold and Röhl (2009); TC2012 = Tsukui and Clyde (2012). For Lauretano et al. (2016) the 2 cycle and 3 cycle options are reported.*

Event	Age
PETM	56.10
ETM2	54.09
C24n.3n (base)	53.90
C24n.2r (base)	53.25
C24n.2n (base)	53.12
C24n.1r (base)	53.02
C24n.1n (base)	52.93
ETM3	52.80
C23r (base)	52.54
L	52.44
M	52.05
C23n (base)	51.78
N	51.70
O	51.31
P	50.81
Q	50.69
C22r (base)	50.60
R	50.50
S	50.30
T	50.14

***Table 1.2**: Astrochronological age of hyperthermal events – labelled following Cramer et al. (2003) and Lauretano et al. (2016) – and magnetochron boundaries, based on the cyclochronological analysis of the CR-BTT composite record.*

1.4.4 Orbital forcing, dissolution cycles and the EECO

Previous data and spectral analysis of $\delta^{13}C$ records from various sites provide evidence that all major hyperthermal events initiated on peculiar orbital configurations corresponding to short eccentricity maxima (Lourens et al., 2005; Westerhold et al., 2007; Galeotti et al., 2010). This finding suggests that orbital forcing was a triggering mechanism for the associated episodes of carbon release (Lourens et al., 2005).

As already evidenced by Galeotti et al. (2010), the AM of the filtered short eccentricity component shows that maximal orbital forcing is associated with depleted wt.% $CaCO_3$ intervals at Gubbio, i.e. more pronounced $CaCO_3$ content minima correspond to short- and long eccentricity maxima, mainly as a consequence of dissolution, similar to what observed at several lower Eocene deep-sea sites (Lourens et al., 2005; Westerhold et al., 2007; Sexton et al., 2011; Kirtland Turner et al., 2014; Laurin et al., 2016). Larger hyperthermals such as ETM2 and ETM3 seem to be part of a continuum of dissolution events paced by a

~1.2 Myr periodic component, which corresponds to the long-term modulation of obliquity, possibly suggesting high-latitude feedbacks in the emplacement of hyperthermals (DeConto et al., 2012). It is worth noticing that the ~1 Myr-long stratigraphic interval of enhanced AM of the short eccentricity, corresponding to enhanced variance in both the $\delta^{13}C$ and wt.% $CaCO_3$ records, starts on a maximum of the 1.2 Myr component – interpreted by Galeotti et al. (2010) as an evidence for the influence of the long-term modulation of obliquity on the succession of the hyperthermal events – thus with an orbital geometry similar to that associated with the emplacement of ETM2 and ETM3. Importantly, within this interval, which corresponds to the entire C23n, each short eccentricity cycle seems to trigger significant dissolution associated with CIEs of up to –0.6 ‰ (Fig. 1.7). Such a prominent feature of this stratigraphic interval is also observed at ODP Site 1258 as revealed by the wavelet analysis of the Fe-counts record by Westerhold and Röhl (2009) (Fig. 1.3) and at ODP Site 1263 (Lauretano et al., 2016), although the amplitude of CIEs in the benthic record from the latter is not as large as observed in the bulk records from CR-BTT and Site 1258. The increase in the frequency of dissolution events and associated CIEs in both bulk and benthic records is indicative of enhanced sensitivity to orbital forcing of the global carbon cycle across this ~1 million year-long time interval. In particular, the absence of a clear long-eccentricity modulation together with the strength of the short-eccentricity component is suggestive of a non-linear response of a highly sensitive system to the 100-kyr forcing associated with a threshold mechanism. This would explain the observation of events of dissolution and $\delta^{13}C$ negative excursions of similar amplitude at each short-eccentricity cycle. In line with the model proposed by Lunt et al. (2011), this observation entails that mean background conditions were close to a thermodynamic threshold during the extreme climate state of the EECO so that each short eccentricity cycle, independently of its amplitude (modulated by the 405 kyr forcing) was effective in triggering the carbon release episodes recorded by the CIEs.

Independently of the mechanism favouring enhanced sensitivity to the short eccentricity forcing, this element provides a mean for a more objective definition of the EECO interval, which has been somewhat loosely defined as a relatively long interval of extreme climate of different duration (from 2 to 3 Myr) by different authors (Zachos et al., 2008; Westerhold and Röhl, 2009; Lauretano et al., 2015) likely because of the lack of objective criteria to define its stratigraphic upper and lower boundary. We, thus, propose to define the EECO in correspondence of the time interval of enhanced sensitivity to short eccentricity, which provides an easy criterion for its univocal identification in any cyclostratigraphic interpretation of marine successions. Moreover, this interval coincides with magnetochron C23n, which makes it easily identifiable also in terrestrial successions.

1.5 CONCLUSIONS

The integrated stratigraphic analysis of the CR-BTT composite section in the Umbria–Marche basin provides a well-defined magneto-, bio- and cyclostratigraphy of the Early Eocene, from the Paleocene/Eocene boundary to the lower part of magnetochron C22r. The detection of orbital components in the geochemical record allows establishing a relative cyclochronology (i.e. cycle counting) of magnetochrons and hyperthermal events across the Early Eocene Climatic Optimum. Comparison of our new (bulk) $\delta^{13}C$ record with similar time series from ODP Site 1258 and ODP Site 1263 confirms the global significance of both long-term trends and transient episodes in the carbon isotope record, which reflect global dynamics of the carbon cycle. Cycle-counting across C23r and C23n, however, reveals a number of eccentricity cycles largely different than previously reported from the two latter ODP sites and in line with the GTS2012. This finding contributes solving the existing discrepancies between time scales based on astrochronological and radioisotopic age interpretation for the Early Eocene interval.

A neat transition to a short eccentricity dominated succession of dissolution events and associated episodes of negative carbon isotope excursion is identified across a 1Myr-long interval, corresponding to C23n. This feature is suggestive of a global carbon cycle characterised by enhanced sensitivity to orbital forcing during the peak warmth of the EECO, in line with models proposing a threshold mechanism for carbon release causing hyperthermal events. The peculiar character of this time interval in terms of carbon dynamics and sedimentary response provides an operational criterion to define the EECO interval, which we propose to restrict to the duration of Chron C23n.

Acknowledgements

This research benefitted from funds provided by MIUR-PRIN grant 2010X3PP8J_005 to SG. We thank Dyke Andreasen and Chih-Ting Hsieh for assistance with stable isotope analyses. We thank two anonymous reviewers for their constructive criticism that contributed improving an earlier version of this paper.

Chapter II

A 9 MILLION-YEAR-LONG ASTROCHRONOLOGICAL RECORD OF THE EARLY-MIDDLE EOCENE CORROBORATED BY SEAFLOOR SPREADING RATES

Francescone Federica, Lauretano Vittoria, Bouligand Claire, Moretti Moretti, Sabatino Nadia, Schrader Cindy, Catanzariti Rita, Hilgen Frits, Lanci Luca, Turtù Antonio, Sprovieri Mario, Lourens Lucas, Galeotti Simone

Published on Geological Society of America Bulletin, https://doi.org/10.1130/B32050.1

ABSTRACT: The early-middle Eocene (~56–41 Ma) is recorded in the pelagic Scaglia Rossa and Variegata Formations of the Umbria-Marche basin (central Italy). Geochemical and magnetostratigraphic alignment between the Bottaccione section (Gubbio, central Italy) and the Smirra core (Cagli, central Italy) allow us to generate a continuous and well-preserved new record that, combined with previously published data from the same area, creates a continuous high-resolution record from the Paleocene-Eocene Thermal Maximum (~56 Ma) to the lower part of Chron C21n. Comparison with carbon isotope records from ODP Sites 1258 and 1263 reveals a satisfactory match, providing further evidence of the global significance of the long-term trend and superposed perturbations captured by the $\delta^{13}C$ records. The identification of astronomically forced geochemical cycles allow us to develop a 405–kyr tuned age model, thereby extending the astrochronology from ~56.0 to ~47.5 Ma. Marine magnetic anomaly profiles from major oceanic basins characterized by high seafloor spreading rates are used to independently test the astronomical polarity time scale associated with our tuning as well as other polarity time scales. Our age model suggests the existence of periods of relatively constant seafloor spreading rates separated by rapid changes, while the other time scales generate more gradual variations and also include large and short-term deviations in spreading rates that occur simultaneously in different oceanic basins, implying errors in polarity reversal ages. The Umbria-Marche age model further contributes to the closure of the middle Eocene gap in the Astronomical Time Scale.

2.1 INTRODUCTION

The early-middle Eocene (~56–41 million years ago or Ma) time interval is characterized by a series of transient global warming events, recorded in both marine and continental settings. These short-lived ($10^{4–5}$ yrs) events, known as hyperthermals, are linked to large perturbations in the global carbon cycle, marked by carbon isotope excursions (CIEs) which track the injection of massive amounts of isotopically light carbon into the exogenic carbon pool (Lourens et al., 2005; Zachos et. al., 2005; Nicolo et al., 2007;

Westerhold and Röhl 2009; Galeotti et al., 2010; Zachos et. al., 2010; Galeotti et al., 2017). The most important of these events are the Paleocene-Eocene Thermal Maximum (PETM) or Eocene Thermal Maximum 1 (ETM1) at ~56 Ma, ETM2 at ~54 Ma and ETM3 at ~52.8 Ma (Kennett and Stott, 1991; Röhl et al., 2004; Lourens et al., 2005; Tripati and Elderfield, 2005; Zachos et al. 2005; Westerhold et al., 2007; Sluijs et al., 2008; Galeotti et al., 2010; Dunkley-Jones et al., 2013; Galeotti et al., 2017). CIEs are associated with increased temperature, recorded as negative excursions in oxygen isotope records, and concomitant $CaCO_3$ dissolution/dilution observed in deep-sea/shallow marine successions. The records show a remarkable imprint of astronomically forced geochemical and lithological cycles (Galeotti et al., 2010; Sexton et al., 2011; Kirtland Turner et al., 2014; Galeotti et al., 2015; Lauretano et al., 2015, 2016; Galeotti et al., 2017; Westerhold et al., 2017). These cycles have provided a robust astrochronological framework for the early Paleogene through their calibration to eccentricity target curves calculated by means of the newest La2010 and La2011 solutions (Laskar et al., 2011a, 2011b; Westerhold et al., 2012, 2017). A robust astrochronological time frame is critical to fully understand the dynamics related to hyperthermal events and to aid in closing the Eocene gap in the Astronomical Time Scale, or ATS (Pälike and Hilgen, 2008). However, uncertainties still affect the time scale partly due to the scarcity of well-exposed and continuous geochemical and magnetostratigraphic records, in particular across the silica-rich (McGowran, 1989) Early Eocene Climatic Optimum (EECO) interval (see also Lauretano et al., 2016; Galeotti et al., 2017). The bathyal pelagic Scaglia Rossa Formation (Fm.) in the Umbria-Marche basin has produced an exceptionally well-preserved and continuous, magnetobiostratigraphic record of the entire Paleogene. Astronomically controlled cycles provide a robust cyclochronology for the early Paleocene corresponding to magnetochron C29r to C27n (Galeotti et al., 2015) and the early Eocene, corresponding to magnetochron C24r-C23n (Galeotti et al., 2010, 2017). Here we extend the already available cyclochronological record of the continuous Scaglia Rossa Fm. by analyzing the interval spanning magnetochron C22r to C21n (~50.5–47.5 Ma) in the Bottaccione section (Gubbio, Italy) and in the newly drilled Smirra core (Turtù et al., 2017). Our results, together with previous data from the Contessa Road-Bottaccione composite section (Galeotti et al., 2010, 2017), provide a continuous 9 million year (Myr)-long astrochronological record of the Scaglia Rossa Fm. spanning from the PETM to the lower part of C21n. Finally, we compare the temporal variations of seafloor spreading in different oceanic basins estimated from the resulting polarity time scale and for other time scales. For this purpose, we use a database of chron widths derived from sea-surface magnetic anomaly profiles (Bouligand et al., 2006) and recently published seafloor spreading curves (Cande and Patriat, 2015; Wright et al. 2016b). The minimization of seafloor spreading variations at multiple localities has long been used as a tool for constructing, refining or correcting the polarity timescale (e.g., Cande and Kent, 1992; Huestis and Acton, 1997; Malinverno et al. 2012; Cande and Patriat, 2015). Here, we prefer to use seafloor spreading rates as a test of the polarity timescale, with the idea that large and short-term deviations in seafloor spreading rate that occur

simultaneously in all the basins point to an error in the time scale. This approach has previously been successfully applied in constructing the Neogene ATS (e.g. Wilson, 1993; Krijgsman et al., 1999).

2.2 GEOLOGICAL SETTING

2.2.2 The Bottaccione Section

In the Umbria-Marche (U-M) basin (Italy), the lower to middle Eocene is locally preserved in the pelagic Scaglia Rossa Fm., characterized by the alternation of well-bedded pink to reddish pelagic limestones and marly limestones. In this study, we extend previously published results from the original sample set of Galeotti et al. (2017), focusing on the well-known Tethyan succession of the Bottaccione (BTT) section at Gubbio (lat. 43°21'56'' N; long. 12°34'57'' E; central Italy; Fig. 2.1B; Arthur and Fisher, 1977; Napoleone et al., 1983; Galeotti et al., 2015, 2017). The studied 15 m interval, spanning 63.6–78.4 m above the Cretaceous/Paleogene (K/Pg) boundary (level 0 of the log in Galeotti et al., 2000), therefore extends the available lower Eocene stratigraphy of Galeotti et al. (2010, 2017) to the top of magnetochron C21r, obtaining a ~48 m–thick continuous and well-preserved record that spans the interval from the PETM to the upper part of magnetochron C21r.

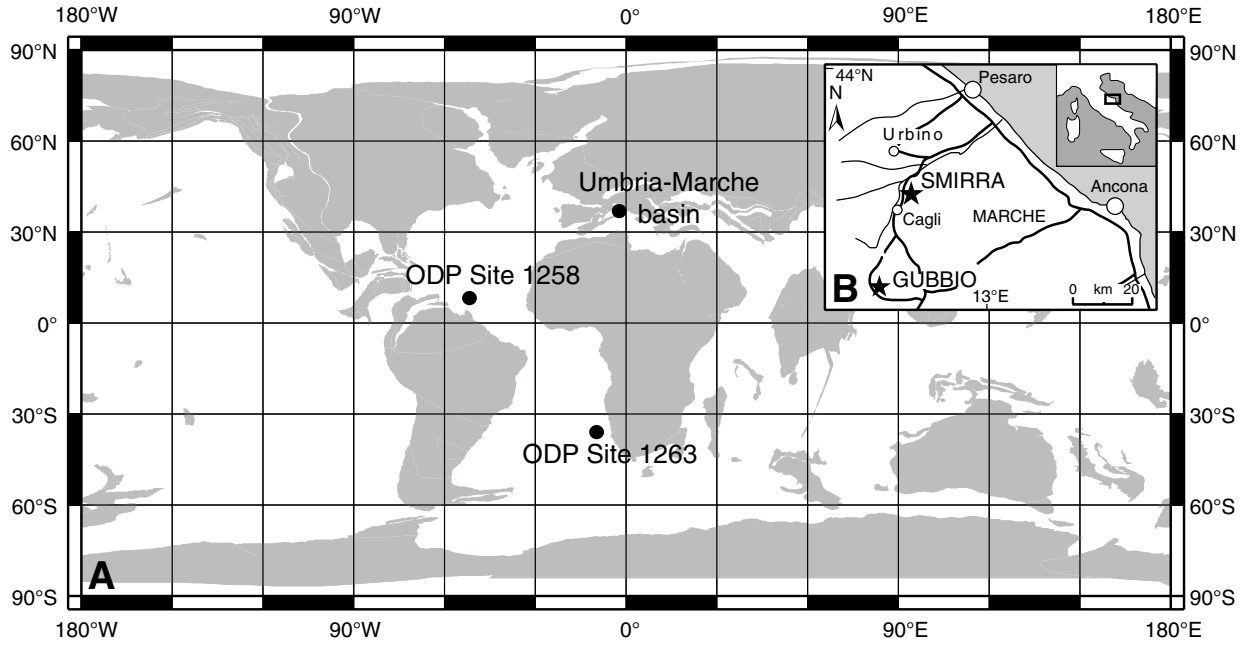

Figure 2.1: *A) Paleoceanographic reconstruction for the early Eocene (50 Ma) showing the position of U-M basin, ODP Site 1258 and ODP Site 1263. Paleogeographic map is from the Ocean Drilling Stratigraphic Network Plate Tectonic Reconstruction Service: (http://www.odsn.de/odsn/services/paleomap/paleomap.html). B) Location map of Gubbio (lat. 43°21'56'' N; long. 12°34'57'' E) and Smirra (lat. 43°35'09.40''N; long. 12°40'37.30''E).*

2.2.3 The Smirra Core

The lower to middle Eocene stratigraphic interval is also well exposed in a small abandoned quarry close to the village of Smirra (lat. 43°35'09.40''N; long. 12°40'37.30''E), in the U-M basin (Fig. 2.1B). The lower Eocene succession is represented by the Scaglia Rossa Fm., while the middle Eocene is recorded by the overlying Scaglia Variegata Fm., composed of whitish to reddish marly limestones and marls with a significant increase in the siliciclastic fraction (~20–30%). In this work, we focus on the succession recovered in Hole 1, hereinafter referred to as Smirra 1, or S1, for a total of 41 m of rock drilled from the top of the exposed outcrop of the quarry, corresponding to level 0 in the log (for more details see Turtù et al., 2017).

2.3 MATERIAL AND METHODS

2.3.1 Magnetostratigraphy

A high-resolution magnetostratigraphic record of the Contessa Road-Bottaccione composite section (CR-BTT) has already been analyzed from magnetochron C24r up to the middle part of magnetochron C22r (Galeotti et al., 2010, 2017). In this work, we have analyzed a total of sixteen samples aimed to detect the exact stratigraphic position of the C22r/C22n and C22n/C21r reversal at the BTT outcrop, in an interval between 63.6 and 78.4 m above the K/Pg boundary, where they were expected to occur according to Lowrie et al. (1982). The rock-magnetic properties of the Scaglia Rossa Fm. are well known (e.g. Lowrie et al., 1982) and paleomagnetic analyses have been carried out following standard procedure (Kirschvink, 1980). The Natural Remanent Magnetization (NRM), ranging from 3.665×10^{-4} A/m to 5.485×10^{-5} A/m, was thermally demagnetized in 15 steps up to a maximum temperature of 625°C where the samples appeared completely demagnetized. The remanent magnetization was measured after each heating step, using a 2G DC-SQUID Cryogenic Magnetometer hosted in a magnetically shielded room, and the characteristic magnetization was computed with principal component analysis, using the PuffinPlot software package (Lurcock et al. 2012). At least 7 points were used to compute the characteristic magnetization.

From the S1core, a total of 143 paleomagnetic samples were collected at a ~30 cm average resolution. Samples were drilled perpendicularly to the vertical core axis and therefore a dip of 0° was assigned to all cylindrical samples, as downhole logs indicate that the borehole did not deviate from the vertical by more than 2–3°. Samples were then cut for NRM analysis (for more details see Turtù et al., 2017).

All paleomagnetic measurements were conducted at the Alpine Laboratory of Paleomagnetism (ALP, Peveragno, Italy).

2.3.2 Geochemistry and Physical Properties

2.3.2.1 Bottaccione Section

Wt.% $CaCO_3$ values of 500 samples have been analyzed at a 3 cm resolution from the interval spanning 63.6 m to 78.4 m above the K/Pg boundary in the BTT section. Calcimetric analyses have been carried out using a "Dietrich-Fruhling" calcimeter. The precision of measurements, based on replicate analyses, is within ±1%. Stable isotope analyses have been carried out on bulk samples from the same interval at 6 cm resolution on a total of 250 samples. Carbon isotope analyses have been performed at the IAMC-CNR laboratory (Capo Granitola, Italy) using an automated continuous flow carbonate preparation GasBenchII device and a ThermoElectron Delta Plus V Advantage mass spectrometer. Analyses were conducted on powdered bulk rock samples after heating them at 400°C to remove organic components. Replicate analyses provide a precision within ±0.06‰. Values are calibrated to the Vienna Pee Dee Belemnite standard (VPDB) and converted to conventional delta notation ($\delta^{13}C$).

2.3.2.2 Smirra 1 Core

Magnetic susceptibility (MS) of S1 core was measured using a Bartington magnetic susceptibility system mounted in the XRF Core Scanner at the Royal Netherlands Institute for Sea Research (NIOZ). The MS2E high-resolution point-sensor has a footprint of 4x10 mm. Sensor drift correction algorithms are implemented in the Avaatech Magsus acquisition software (avaatech.com). Carbon stable isotope values were measured on 548 bulk sediment samples between 0 and 41 m depth. The cores were sampled at ~10 cm resolution using an 8 mm rock drill to collect dry powder sediment core samples in the limestone intervals. Samples from marly layers were collected by hand and were freeze-dried before crushing to obtain homogenized dry samples. Isotope measurements were carried out on 80–1000 μg of dry material at Utrecht University using a CARBO-KIEL automated carbonate preparation device linked to a Thermo-Finnigan MAT253 mass spectrometer and a Finnigan GasBench-II, with an analytical precision of 0.04‰.

2.3.3 Spectral Analysis

Wavelet analysis was used to compute the evolutionary spectra of data series in the depth domain, using the wavelet script of Torrence and Compo (1998) and a Morlet mother wavelet with an order of 6. In the CR-BTT composite section, wt.% $CaCO_3$ content encompassing the lower part of magnetochron C24r to the upper part of C21r was evaluated, and for the S1 core the MS series was analyzed from the upper part of C22r to C21n. In addition, power spectral analysis of the BTT $CaCO_3$ record, after a 2^{nd} order polynomial detrending, and of the MS record from the S1 core, was conducted via the Multi Taper Method (MTM) with 3 tapers and a time-bandwidth product of 2, using the Astrochron Package (Meyers, 2014); this

approach allows the identification of periodic components exceeding the 95% confidence level, according to the robust noise estimation algorithm of Mann and Lees (1996).

2.3.4 Seafloor Spreading Rates

The U-M age model obtained in this study, as well as other published age models such as Cande and Kent (1995), or CK95, Geologic Time Scale (GTS) 2004 (Ogg and Smith, 2004), GTS2012 (Ogg, 2012; Vandenberghe et al., 2012) and Westerhold et al. (2017), or Wetal17, were tested by constructing curves of the seafloor spreading rate, using the database of magnetic anomaly width from Bouligand et al. (2006). To construct this database, sea-surface magnetic anomaly profiles were first corrected for the main magnetic field, reduced to the pole, and projected in the direction of seafloor spreading, and are assumed constant in a given area (see Bouligand et al., 2006 for details). Geomagnetic reversals recorded by the oceanic crust were then located by searching for the maximum gradient along these profiles. The data used here come from the Indian, North Pacific and South Pacific Oceans, and originates from 6 main spreading centers (Fig. 2.2). For each spreading center, we estimated an averaged value and its 95% confidence interval for chron width (measured in the spreading rate direction) and then deduced from the age model the same quantities for the spreading rate. For spreading centers where data from both conjugate flanks are available, we first computed the averaged values and 95% confidence intervals of the half-spreading rates for each flank and then deduced the same quantities for the average of both flank values. This approach takes into account possible spreading asymmetry (e.g., Müller et al., 2008).

The method described here for estimating seafloor spreading curves is simpler than the usual method relying on the estimation of the rotation parameters (e.g. Hellinger, 1981). We decided however to use the dataset of Bouligand et al. (2006) because its temporal sampling is larger than recently published sea-floor spreading curves available for the Indian (Cande and Patriat, 2015) and Pacific Oceans (Wright et al., 2016b). Although the selected areas are characterized by a relatively constant spreading direction during the investigated period, some of the spreading rate variations deduced from the database of chron widths of Bouligand et al. (2006) could reflect small directional changes. For this reason, we also compared these curves with published spreading rates based on rotation parameters (Cande and Patriat, 2015; Wright et al. 2016b) that we adjusted to the different timescales.

The resolution of sea-surface magnetic profiles is limited by water depth, which is ~5000 m for the period 47.7–53.9 Ma investigated here (according to Parsons and Sclater, 1977). This resolution limit prevents us, using the method mentioned above, from correctly locating reversals that are bounding chrons whose widths are shorter than ~5000 m (i.e. ~125 kyr for a sea-floor spreading rate of 40 km/Myr). This is due to the fact that sea-surface magnetic anomalies caused by such short chrons have a width controlled by the water depth (5000 m) and not by the true chron width. For this reason we did not include, for the construction of spreading rate curves, the reversals from very short subchrons C23n.1r and C24n.2n, whose

durations (51 kyr and 100 kyr respectively in the new U-M age model) are shorter than the resolution of sea-surface magnetic profiles.

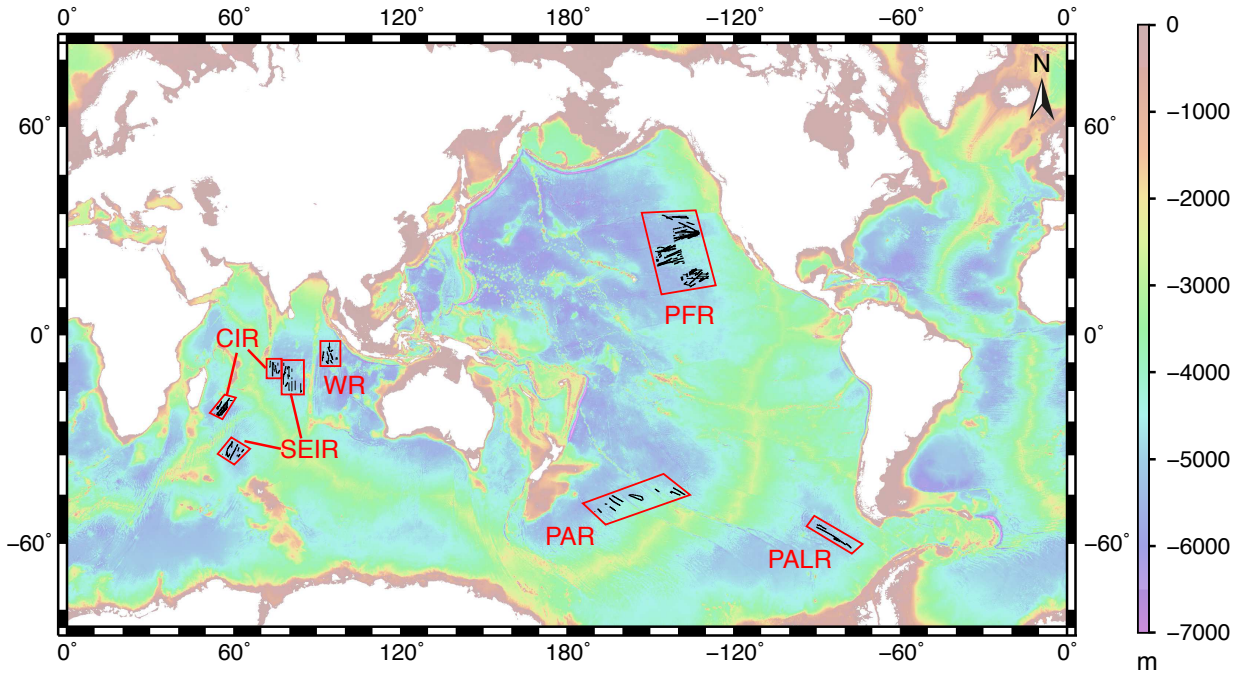

Figure 2.2: *Location of selected areas (red polygons) and magnetic profiles (black) over bathymetry from Smith and Sandwell (1997). Data originating from the same spreading center have been grouped together (see Cande and Patriat, 2015; Wright et al., 2016; Royer and Sandwell, 1989): CIR: Central Indian Ridge; SEIR: South East Indian Ridge; WR: Wharton Ridge; PFR: Pacific Farallon Ridge; PAR: Pacific Antarctic Ridge; PALR: Pacific Aluk Ridge.*

2.3.5 Comparison of synthetic and observed magnetic profiles

The duration of the short subchrons in C23n and C24n was tested by comparing the overall shape of stacks of observed magnetic anomaly profiles and synthetic profiles deduced from the age models with the assumption of a constant spreading rate and of a magnetized crust with a constant thickness and magnetization intensity. Before stacking, magnetic profiles were stretched between tie-points (chron boundaries) to match the averaged chron width within each area. We used $C22r_{(base)}$, $C23n.1n_{(base)}$, $C23n.1r_{(base)}$, and $C23n.2n_{(base)}$ boundaries as tie-points for Chron C23n and $C23r_{(base)}$; $C24n.1n_{(base)}$, $C24n.2r_{(base)}$, and $C24n.3n_{(base)}$ boundaries were used for Chron C24n. Synthetic profiles were computed at the pole (i.e. assuming a vertical direction for the magnetic field and magnetization), assuming that the seafloor topography follows the relation with age of Parsons and Sclater (1977), and using the algorithm of Talwani and Heirtzler (1964) with the method of Tisseau and Patriat (1981) to model off-axis intrusions and lava flows. We then shifted and rescaled the magnetic anomaly values in the stack to obtain a best-fit (in the least-square sense) to the synthetic profiles, to assist with our comparison. This was needed because

observed profiles were only partially corrected to the pole (correction of their skewness but not of their amplitude, see Bouligand et al., 2006 for more details) and possibly included the effect of a regional field that had not been corrected for, introducing a constant shift in the magnetic anomaly values. Finally, similarities between stacks and synthetic profiles were quantified by computing their Pearson correlation coefficients.

2.4 RESULTS

2.4.1 Bottaccione Section

2.4.1.1 Magnetostratigraphy

The results previously published by Galeotti et al. (2017) from the BTT section clearly show two reversals between 51.75–51.8 and 57.02–57.28 m above the K/Pg boundary (Fig. 2.3A). As already identified by different authors (Arthur and Fisher, 1977; Napoleone et al., 1983), these two reversals correspond to the C23r/C23n and C23n/C22r magnetochron boundaries. In addition to the 3 magnetozones detected by Galeotti et al. (2017), we identify two additional reversals between 66.24–66.31 and 71.60–72.00 m above the K/Pg boundary. In agreement with the original sampling of Arthur and Fisher (1977), the ~5.5 m–thick normal polarity interval between these magnetochron boundaries corresponds to magnetochron C22n. However, our paleomagnetic analysis does not allow us to define the top of this polarity chron with a precision better than ~40 cm, which corresponds to a ~50 kyr uncertainty considering the total duration of Chron C22n (Cande and Kent, 1995).

2.4.1.2 Geochemistry

Geochemical records show a large variability across the surveyed interval with wt.% $CaCO_3$ content ranging between ~68 and ~99%, with an average value of ~92.8% (Fig. 2.3A), and carbon isotope values ranging between ~1.0 to ~1.8‰, with CIEs up to ~0.5‰ (Fig. 2.4). On a long-term trend, following the rapid increase of average carbon isotope values in the upper half of C23n (Galeotti et al., 2017), $\delta^{13}C$ values vary across an average of ~1.5‰. Both records show an evident cyclicity, which has already been shown to be related to astronomical forcing both in the U-M succession and oceanic records (Westerhold and Röhl, 2009; Galeotti et al., 2010, 2017; Westerhold et al., 2017). In particular, periods of depleted $\delta^{13}C$ values and concomitant impoverishment of wt.% $CaCO_3$ related to carbonate dissolution correspond to a maximal forcing (Lourens et al., 2005; Westerhold and Röhl, 2009; Galeotti et al., 2010, 2017; Westerhold et al., 2017).

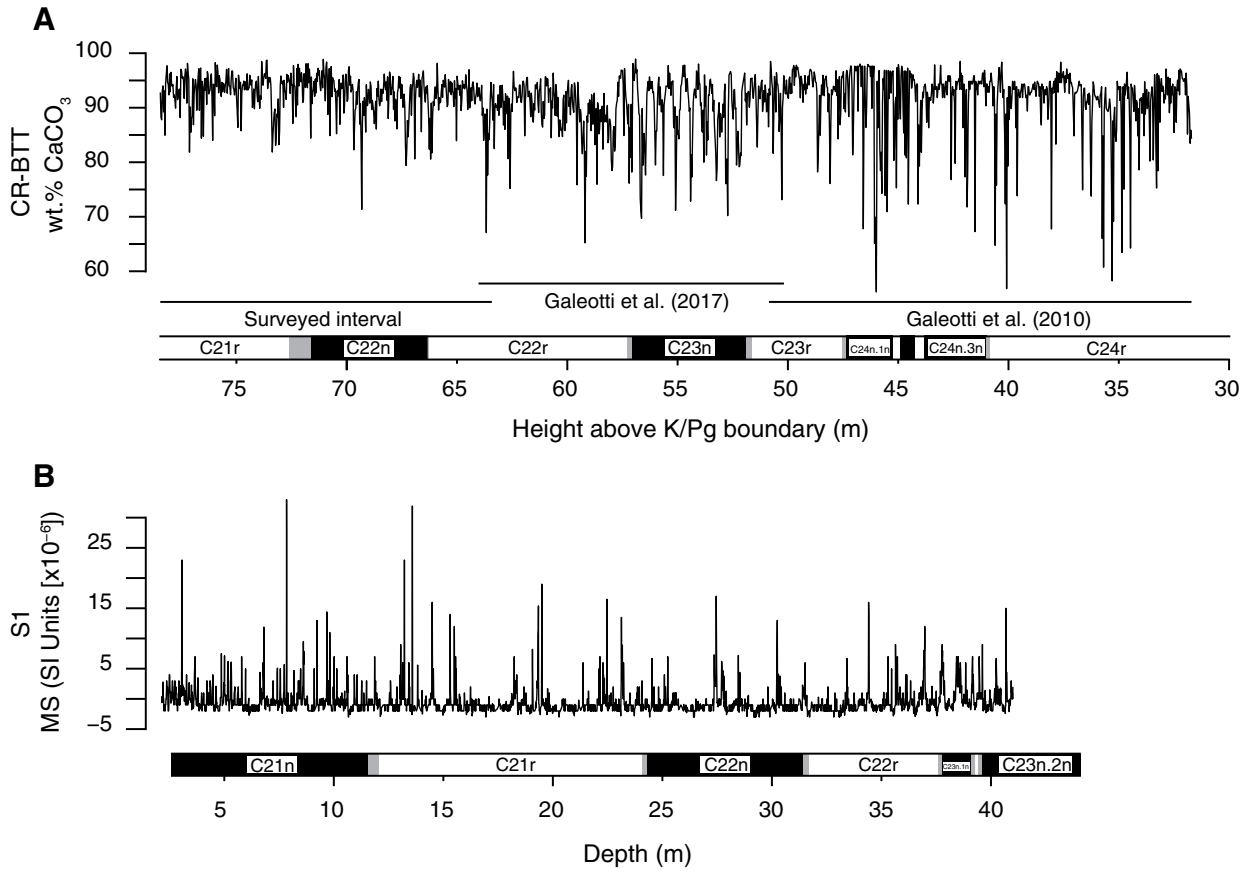

Figure 2.3: *A) Wt.% $CaCO_3$ record from the Contessa Road-Bottaccione composite section plotted against the magnetostratigraphy and B) MS values from Smirra 1 plotted against the magnetostratigraphy.*

2.4.2 Smirra 1 Core

2.4.2.1 Paleomagnetism

A detailed magnetic stratigraphy has been obtained by identifying the characteristic remanent magnetization (ChRM). The newly produced paleomagnetic record of the S1 core, which spans from Chron C21n to C23n (Turtù et al., 2017), is in good agreement with records obtained from other deep-sea cores for the same stratigraphic interval, allowing detailed comparison (Westerhold and Röhl, 2009; Galeotti et al., 2010; Sexton et al., 2011; Galeotti et al., 2017). In particular, the magnetostratigraphic record from S1 is consistent with BTT and the thickness differences between magnetozones are generally limited to ~0.5 m. A larger discrepancy is observed for magnetochrons C22r and C22n, which are respectively ~2.5 m shorter and ~1.5 m longer compared to the same magnetochrons at the BTT section (Fig. 2.3B). These differences might be related to undetected tectonic deformations at Smirra, although no evidence of faulting can be observed in the cores nor in the optical logs (Turtù et al., 2017).

2.4.2.2 Bulk $\delta^{13}C$ and Magnetic Susceptibility Records

The bulk $\delta^{13}C$ record shows a large variability (Fig. 2.4). From the interval encompassing C23n.2n, average baseline carbon isotope values undergo a gradual increase of ~0.5‰ with heavier values persisting to the top of C21r, from which we can also observe a transition towards lighter values up to the top of the core. Superimposed on the long-term trends, the Smirra $\delta^{13}C$ record is punctuated by short-term negative carbon isotope excursions as found in coeval deep-sea records (Galeotti et al., 2010; Sexton et al., 2011; Kirtland Turner et al., 2014; Lauretano et al., 2016; Galeotti et al., 2017). These CIEs vary in amplitude between ~0.4 and ~1.0‰ and are associated with higher MS values.

2.5 GEOCHEMICAL CORRELATION OF THE UMBRIA-MARCHE RECORDS WITH ODP SITE 1258 AND ODP SITE 1263

Carbon isotope records provide a robust means for inter-site geochemical correlation, as hyperthermal events and dynamics regulating changes in seawater $\delta^{13}C$ have a global significance. We apply this exercise to the carbon isotope profiles of the S1 and BTT records for a local comparison, followed by their comparison with ODP Site 1258 at Demerara Rise (Sexton et al., 2011; Kirtland Turner et al., 2014) and ODP Site 1263 at Walvis Ridge (Lauretano et al., 2016 - Fig. 2.4). We label prominent CIEs following Cramer et al. (2003) up to the lowermost magnetochron C23r, including H1 to L, and use the Lauretano et al. (2016) nomenclature between the middle C23r and the lower C22n, including M to W. For the rest of the studied interval (middle C22n to upper C21r) we follow the labelling of Sexton et al. (2011), revised by Westerhold et al. (2017). Comparison of the S1 with the BTT record shows a very good match of both the long-term trend and individual CIEs. Moreover, this carbon isotope stratigraphy correlation allows us to test the discrepancies observed in the thickness of C22n and C22r magnetochrons between the two sites. In particular, a very good match of the $\delta^{13}C$ records is observed within C22n, which is ~1.5 m longer at Smirra. However, a slightly higher average sedimentation rate is observed at S1 (Turtù et al., 2017) compared to Bottaccione (Galeotti et al., 2010, 2017), and also for other magnetostratigraphic intervals. It is more difficult, thus, to explain the occurrence of a shorter C22r at Smirra. Furthermore, the carbon isotope record at BTT is characterized by two prominent CIEs, correlated with S and T of Lauretano et al. (2016), which are found at 59.2 m and 60.3 m above the K/Pg boundary. Despite the easy recognition of these events, we are not able to identify them at S1. Accordingly, the comparison between the carbon isotope records suggests that a gap of at least 3 m occurs in S1, even though there is no direct evidence for tectonic disturbance, but this does not exclude the possibility of a sedimentary hiatus or slump scar. By contrast, the U event (Lauretano et al., 2016), characterized by a prominent CIE that occurs in the upper part of magnetochron C22r, is well recognizable in both carbon isotope records. From here upwards, the chemostratigraphic correlation between S1 and BTT is straightforward up to the middle part of Chron C21r,

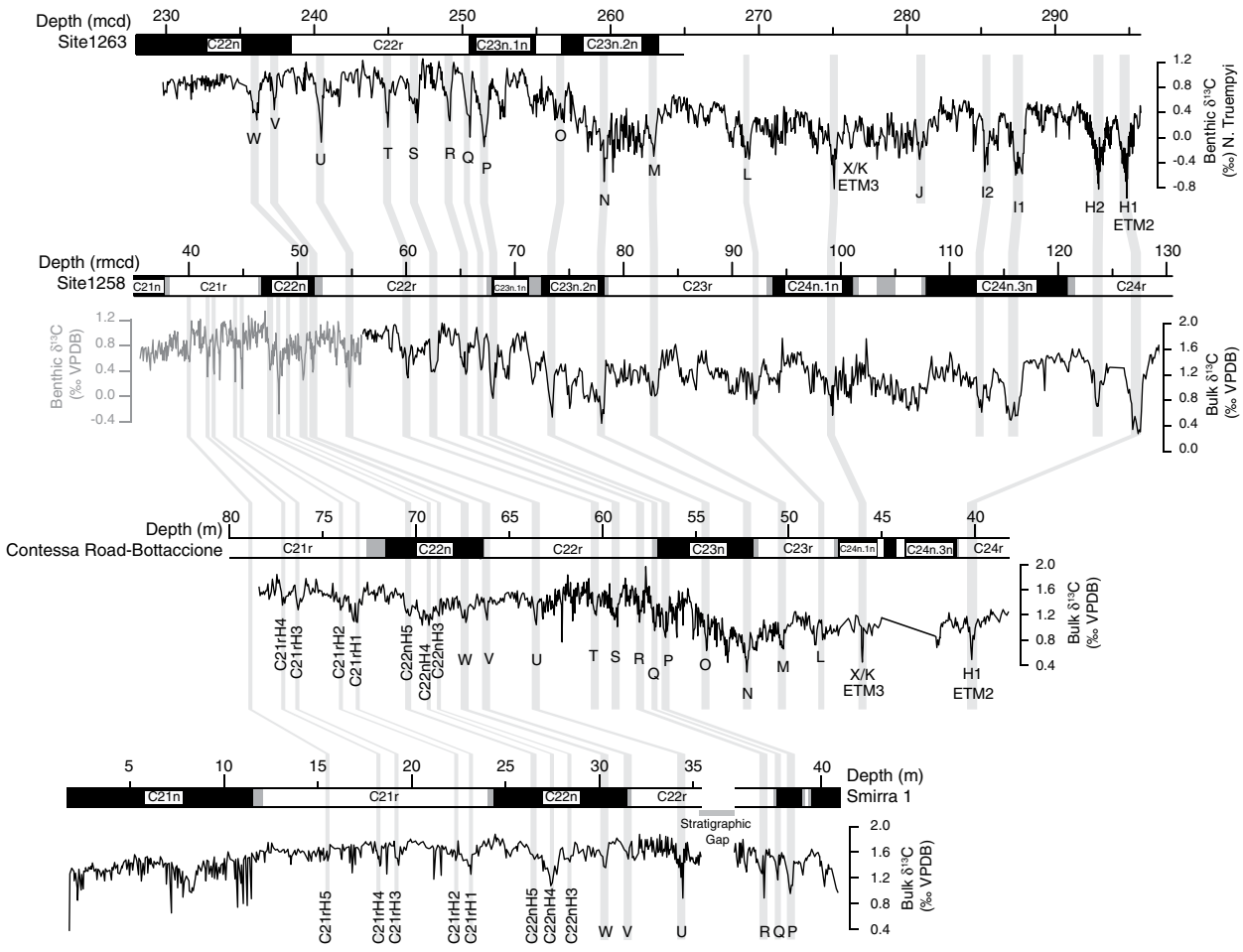

Figure 2.4: *Chemostratigraphic ($\delta^{13}C$) and magnetostratigraphic correlation between ODP Site 1263 (Lauretano et al., 2016), ODP Site 1258 (Sexton et al., 2011 - grey line - and Kirtland Turner et al., 2014 - black line), Contessa Road-Bottaccione composite section and Smirra 1.*

as depicted in Figure 2.4. For this reason, the spectral analysis of S1 has been performed only on the stratigraphic interval that spans 2.3 to 33 m. This still allows building a composite and continuous cyclochronological record of CIEs from the U-M basin up to magnetochron C21n. Moreover, comparison of the U-M record with ODP Site 1258 at Demerara Rise (Sexton et al., 2011; Kirtland Turner et al., 2014) and ODP Site 1263 at Walvis Ridge (Lauretano et al., 2016) shows a remarkably good match between the carbon isotope profiles including both longer-term trends and CIEs within individual magnetochrons (Fig. 2.4). Minor differences are observed in the positions of a few CIE events with respect to the magnetostratigraphy at each site. Following the integration with the S1 record, we reexamined the stratigraphic position of each magnetochron in the CR-BTT composite record of Galeotti et al. (2017). This inspection reveals that all the magnetochrons have been correctly located in the spliced succession with the exception of magnetochron C23n, which has been re-studied and whose upper limit occurs ~50 cm below

the estimate of Galeotti et al. (2017), based on a splice with the record of Galeotti et al. (2010). Accordingly, C22rH1 or Q (Kirtland Turner et al., 2014; Lauretano et al., 2016) now consistently falls in the lowermost part of magnetochron C22r both at Smirra and Bottaccione, similar to what is observed at Site 1258 and 1263 (Westerhold et al., 2017). However, C22nH1 or V (Kirtland Turner et al., 2014; Lauretano et al., 2016), which coincides with the C22r/C22n magnetochron boundary in the U-M records, falls in the lowermost part of C22n at ODP Site 1263 (Lauretano et al., 2016; Westerhold et al., 2017) and at ODP Site 1258 (Sexton et al., 2011; Kirtland Turner et al., 2014). Despite these minor differences in the position of the C22nH1/V event, the good alignment of the Umbria Marche record with that of ODP Site 1258 (Sexton et al., 2011; Kirtland Turner et al., 2014) and ODP Site 1263 (Lauretano et al., 2016; Westerhold et al., 2017) evidently results from the global significance of factors controlling the carbon cycle.

2.6 CYCLOSTRATIGRAPHY

2.6.1 The Bottaccione Record

The wavelet spectrum of the wt.% $CaCO_3$ content from the CR-BTT reveals high spectral density above the 95% confidence limit corresponding to wavelengths of ~50 cm and ~2 m between 32 to 57 m. These cycles have been linked to correspond to the short and long eccentricity cycles, respectively, by Galeotti et al. (2017 - Fig. 2.5). Much of the spectral power is centered at a longer wavelength of ~4.5 m, which, based on the analysis of the same succession, has been interpreted to track the long-term (~1.2 Myr) modulation of obliquity (Galeotti et al., 2010; DeConto et al., 2012). This component is also evident in the amplitude modulation of the short eccentricity, which shows maxima at ~35, ~40 and 45m, i.e. between ~55–52 Ma. A similar long-term modulation of the short eccentricity has been reported to occur in sedimentary cycles from various ODP Sites across the same interval possibly suggesting a transition from libration to circulation (Westerhold et al., 2017), which is contemplated in the La2010b and La2010c astronomical solutions (Laskar et al., 2011a). A large increase in sedimentation rate is clearly indicated in the wavelet spectrum at 57 m, observed as a shift in the wavelength of the dominant spatial cycles, corresponding to the C23n/C22r magnetochron boundary. From here upwards, the interpreted astronomical components shift to lower frequencies, in line with an average sedimentation rate of ~0.85 cm/kyr in the 8.5 m–thick C22r magnetochron compared to ~0.5 cm/kyr in the C23n magnetochron, based on the Cande and Kent (1995) GPTS. The wavelet spectrum shows a strong amplitude modulation of both the ~50 cm component up to ~57 m above the K/Pg boundary and the ~90 cm component for the interval from 57 to 78.4 m above the K/Pg boundary. Assuming that the ~50 cm cycles below 57 m and the ~90 cm cycles above represent short eccentricity, the observed amplitude modulation can be ascribed to the 405–kyr period eccentricity cycles being expressed by a wavelength of ~2 m up to the base of C23n and of ~3.5 m in the interval spanning the lowermost C22r to middle C21r magnetochron. Due to this, spectral analysis has been conducted with only

a little overlap with the interval analyzed by Galeotti et al. (2017), which is entirely characterized by an average sedimentation rate of ~0.5 cm/kyr.

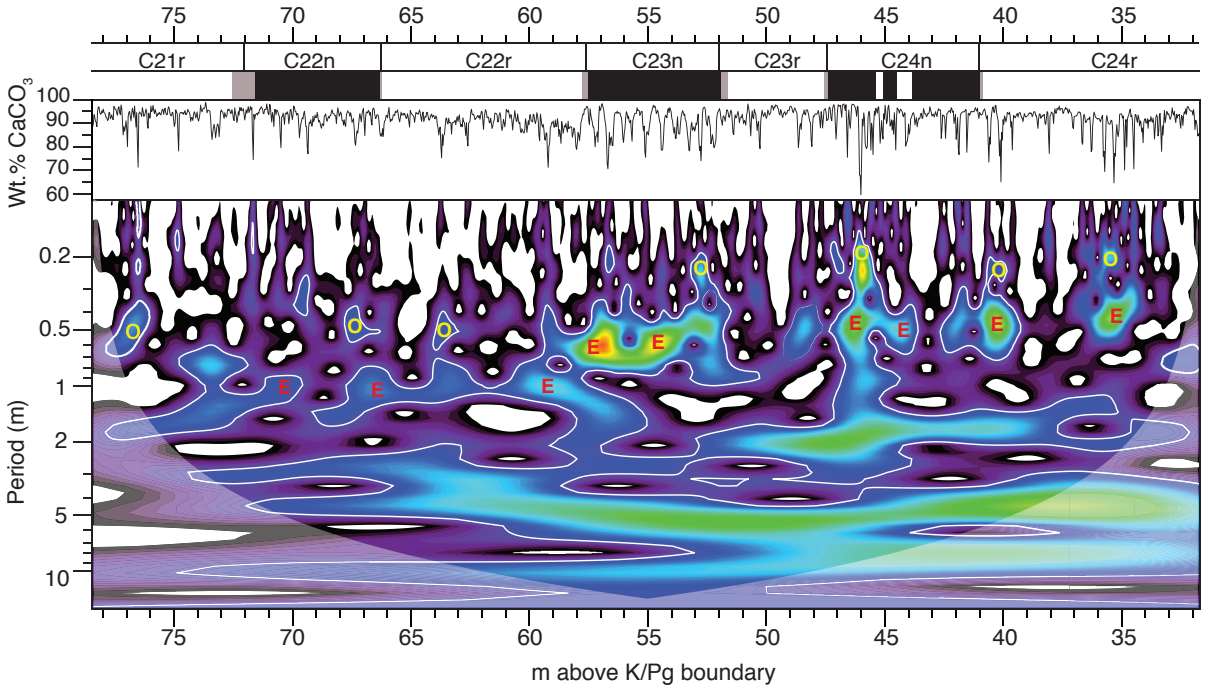

Figure 2.5: *Evolutionary wavelet analysis for wt.% $CaCO_3$ content from the Contessa Road-Bottaccione composite section for the interval spanning from 32 to 78.4 m above the K/Pg boundary and magnetostratigraphy. White contours indicate the 95% confidence level for a red-noise model. "E" identifies the interpreted short eccentricity terms, and "O" the interpreted obliquity terms.*

MTM spectral analysis of the interval spanning 57 to 78.4 m above the K/Pg boundary confirms the interpretation of the wavelet analysis, with a spectral peak corresponding to a frequency of 0.265 cycles/m (wavelength of 380 cm) and a double peak at frequencies of ~0.85 and 1.15 cycles/m (wavelengths of 118 and 87 cm, respectively; Fig. 2.6A). Based on an average sedimentation rate of ~0.85 cm/kyr, these frequencies are interpreted to represent the long eccentricity E1 term and the E2 and E3 terms of the short eccentricity, respectively. Astrochronological testing through the Evolutive Average Spectral Misfit technique (E-ASM; Meyers and Sageman, 2007; Meyers et al., 2012) on the lower Eocene of the CR-BTT composite section (Laurin et al., 2016) confirms this interpretation.

On this basis, the spectral peaks occurring at frequencies of 2.15 and 2.62 cycle/m, corresponding to wavelengths of 46 cm and 38 cm, might represent the two main terms of obliquity (54 and 41 kyr), although the 54–kyr term is predicted to be weakly expressed in sedimentary records (Laskar et al., 2004). Spectral peaks are also present in the frequency range expected for precession, but these are not as clearly expressed as the peaks associated with eccentricity and obliquity.

2.6.2 The Smirra 1 Core Record

The wavelet analysis of the MS record from the 2.3–33 m interval shows components, above the 95% confidence level, similar in frequency to the upper part at BTT. In particular, these components have wavelengths centered at ~100, ~40 and ~20 cm up to the lower part of C21n (Fig. 2.7). According to Cande and Kent (1995), the C22n-C21r magnetochron interval has an average sedimentation rate of 1.09 cm/kyr. On this basis, the observed components represent the sedimentary expression of the astronomical forcing related to short eccentricity, obliquity and precession. A shift towards shorter wavelengths is observed at ~9 m up to the top of the record, within magnetochron C21n, suggesting a substantial decrease in sedimentation rate. Based on results from wavelet analysis, MTM analysis has been carried out on two distinct stratigraphic segments spanning from 2.3–9 m and 9–33 m (Fig. 2.6).

The MTM spectrum for the stratigraphic segment spanning from 9–33 m confirms the interpretation of the wavelet analysis, providing evidence for distinct peaks exceeding the 95% confidence level with frequencies centered at ~0.278 and ~1.03 cycles/m, and five peaks centered at ~5.79 cycles/m (Fig. 2.6B). These frequencies correspond to cyclic components with wavelengths of 360, 97 and 17 cm, respectively. Based on the average sedimentation rate, this implies periods of ~400, ~100 and ~20 kyr, respectively. The best fit sedimentation rate obtained using the TimeOpt routine (Meyers, 2015) on the MS record is ~1 cm/kyr, which provides further evidence that the periodic components revealed by MTM are astronomically controlled (Fig. 2.8).

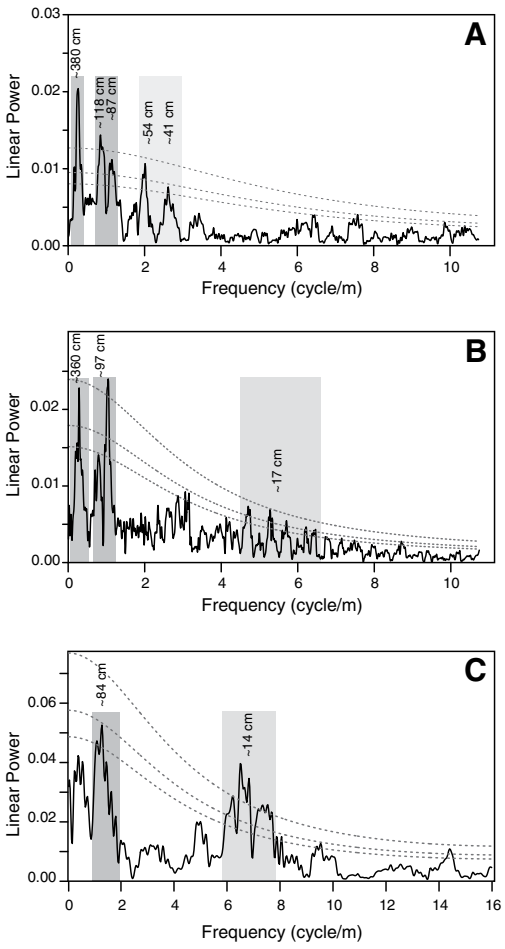

MTM analysis of the upper segment (2.3–9 m) reveals distinct peaks exceeding the 90% confidence level at ~1.18 cycles/m (wavelength of 84 cm) and a dominant component exceeding the 99% confidence level centered at ~7.18 cycles/m (wavelength of 14 cm; Fig. 2.6C). The decrease in sedimentation rate detected by wavelet analysis suggests that these signals could be ascribed to the short eccentricity and precessional components, respectively. However, we have not included this interval in the final astrochronology because of its limited thickness and because the available record does not reach the top of C21n.

Figure 2.6: *Results of MTM spectral analyses carried out (A) on the $CaCO_3$ content from the Bottaccione section for the interval spanning 57 to 78.4 m above the K/Pg boundary, (B) on MS values from Smirra 1*

for the stratigraphic interval from 9 to 33 m and (C) on MS values from Smirra 1 for the stratigraphic interval from 2.3 to 9 m. Dashed lines represent the 90%, 95% and 99% confidence levels for robust red noise (Mann and Lees, 1996).

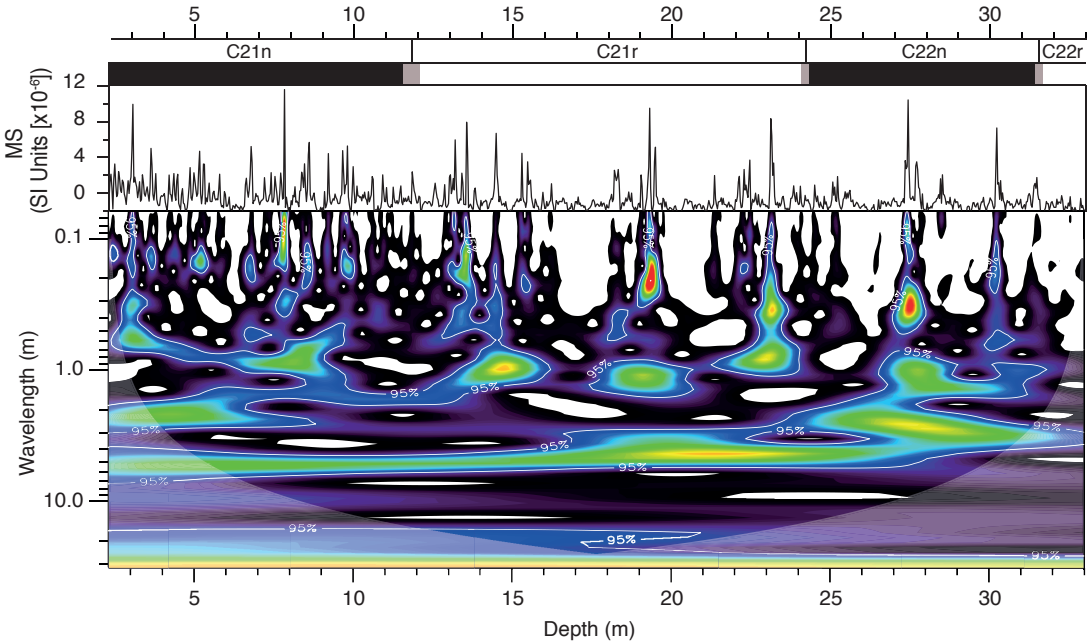

Figure 2.7: *Evolutionary wavelet analysis for MS values from the Smirra 1 for the interval spanning from 2.3 to 33 m. White contours indicate the 95% confidence level for a red-noise model. "E" identifies the interpreted short eccentricity terms.*

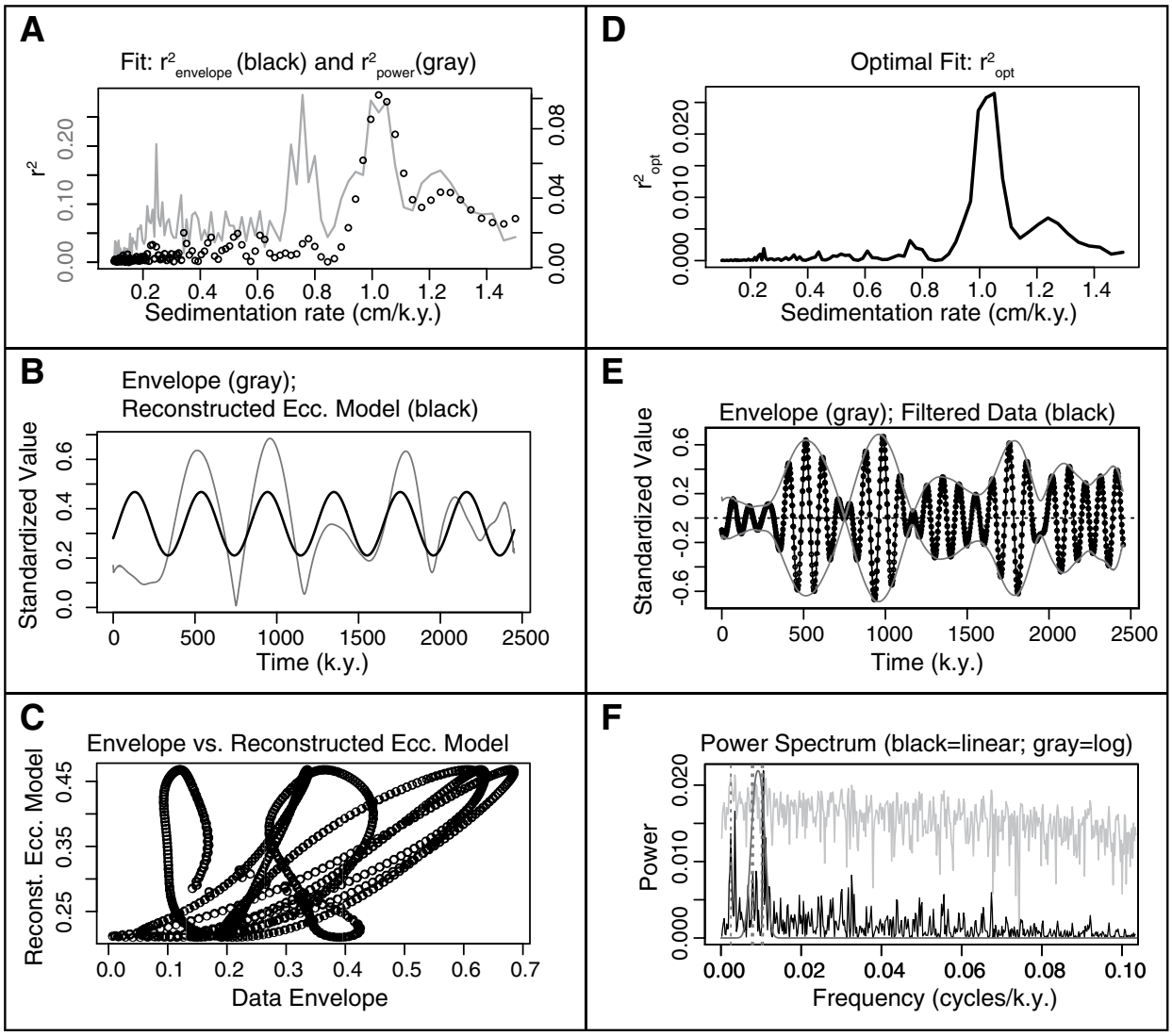

Figure 2.8: *TimeOpt analysis on the MS at Smirra 1 for the interval spanning from 9 to 33 m. A) Squared Pearson correlation coefficient for the amplitude envelope fit (r^2 envelope - black dots) and the spectral power fit (r^2 spectral - gray line) at each evaluated sedimentation rate. B) Comparison of the data amplitude envelope (gray) and the TimeOpt-reconstructed eccentricity model (black). C) Cross plot of the data amplitude envelope and the TimeOpt-reconstructed eccentricity model in panel (B). D) Combined envelope and spectral power fit (r^2_{opt}) at each evaluated sedimentation rate. E) Comparison of the band-passed eccentricity signal (black), and the data amplitude envelope (gray) determined via Hilbert transform. F) Periodogram spectrum for the Bottaccione section, given the TimeOpt derived sedimentation rate of ~1 cm/kyr (black line = linear spectrum; gray line = log spectrum). Gray dashed lines indicate the eccentricity target periods.*

2.7 ASTROCHRONOLOGY AND THE UMBRIA-MARCHE AGE MODEL

2.7.1 C22r-C21r Magnetochron Interval

To conduct the eccentricity-based cycle counting within the stratigraphic interval encompassing C22r-C21r magnetochrons in the U-M basin, we use the cycle component corresponding to the long eccentricity (E1) term with a duration of 405 kyr. Based on the MTM spectral analysis results, a component with a wavelength of ~4 m has been extracted from the wt.% $CaCO_3$ record of the BTT section and the MS record of S1 using the AnalySeries program (Paillard et al., 1996) and applying a Gaussian filter with a bandwidth of ±15%. This allowed us to establish a floating cyclochronology for the studied interval. Based on the obtained floating cyclochronology, we count 2.75 and 1.75 405–kyr cycles in magnetochrons C22r and C22n at BTT, respectively (Fig. 2.9). The same result is obtained for magnetochron C22n at S1, where we also count 2.75 405–kyr cycles in magnetochron C21r (Fig. 2.10). Filtering of the E2+E3 short eccentricity components (~1 m wavelength) shows the expected amplitude modulation by the 405–kyr eccentricity in both records.

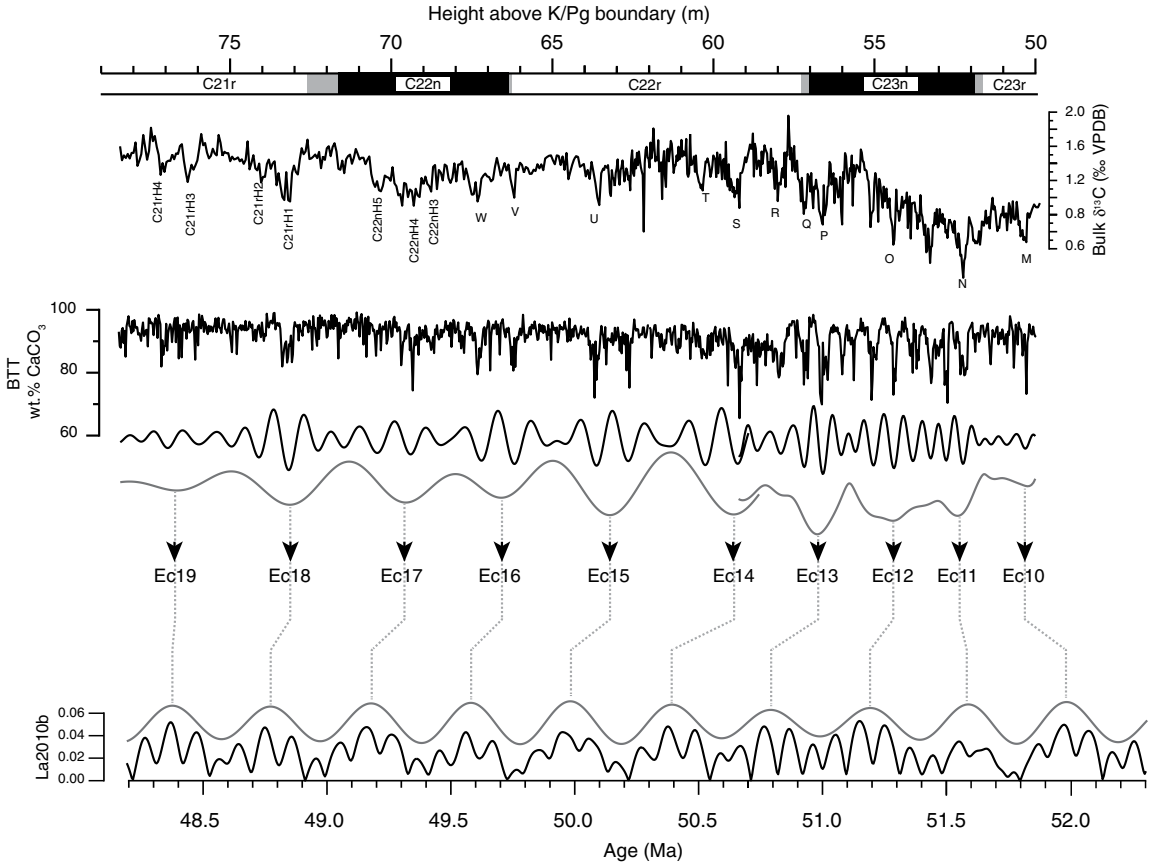

Figure 2.9: *Long eccentricity (grey line) and short eccentricity (black line) filters for the interval spanning 50 to 78.4 m at Bottaccione section plotted against the La2010b (Laskar et al., 2011a) astronomical solution. Long eccentricity maxima are labelled following the numbering of Galeotti et al. (2017). For the*

interval spanning the uppermost part of C23r to the uppermost part of C22r magnetochrons, we identify long eccentricity maxima and minima from the amplitude and frequency modulations of the short eccentricity term (Galeotti et al., 2017).

A very good match between the two sites is also obtained when comparing short eccentricity cycles across the overlapping interval, i.e. C22n, providing further evidence of the robustness of the cyclochronological interpretation. Assuming an average duration of 100 kyr for the short eccentricity cycles, we obtain a total duration of 1010 and 700 kyr for magnetochrons C22r and C22n, respectively. Because of uncertainty in the stratigraphic position of the top of C22n at BTT, the estimated duration of C22n is based only on the S1 record, where we can count 7 complete short eccentricity cycles, for a total of 710 kyr. The S1 record allows extending the cycle counting up to include magnetochron C21r, where we count 12 short eccentricity cycles for a total of 1200 kyr.

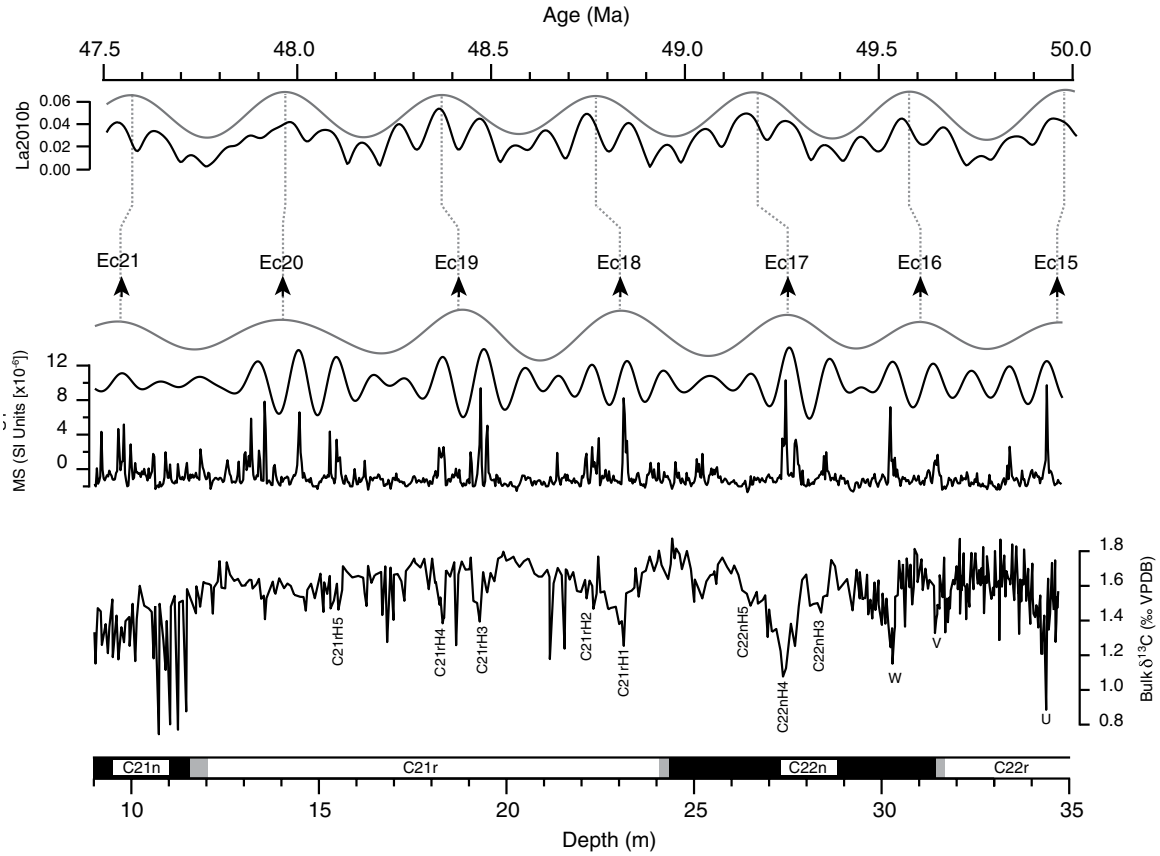

Figure 2.10: *Long eccentricity (grey line) and short eccentricity (black line) filters for the interval spanning 35 to 9 m in the Smirra 1 core plotted against the La2010b (Laskar et al., 2011a) astronomical solution. Long eccentricity maxima are labelled following the numbering of Galeotti et al. (2017).*

The obtained cyclochronology provides the basis for an astronomical tuning of the U-M record from C22r to C21n magnetochrons. For this goal, we tune the 405–kyr eccentricity filtered component to the most recent astronomical solution of La2010b (Laskar et al., 2011a), allowing an optimal comparison

with recently published results from the same time interval (Westerhold et al., 2017). Because of the absence of a clear long eccentricity cycle from the uppermost part of C23r to the uppermost part of C22r, we tune the long eccentricity maxima identified from the amplitude and frequency modulations of the short eccentricity cycle, following the method reported by Laurin et al. (2016) and adopted by Galeotti et al (2017). As a tie point we use the age of the C 23r/C23n magnetochron boundary, i.e. 51.78 Ma (Galeotti et al., 2017), corrected to 51.72 Ma, following a new linear age interpolation based on the observation of the maximal amplitude and frequency modulation interval of the E2+E3 terms of eccentricity (Figs. 2.11 and 2.12).

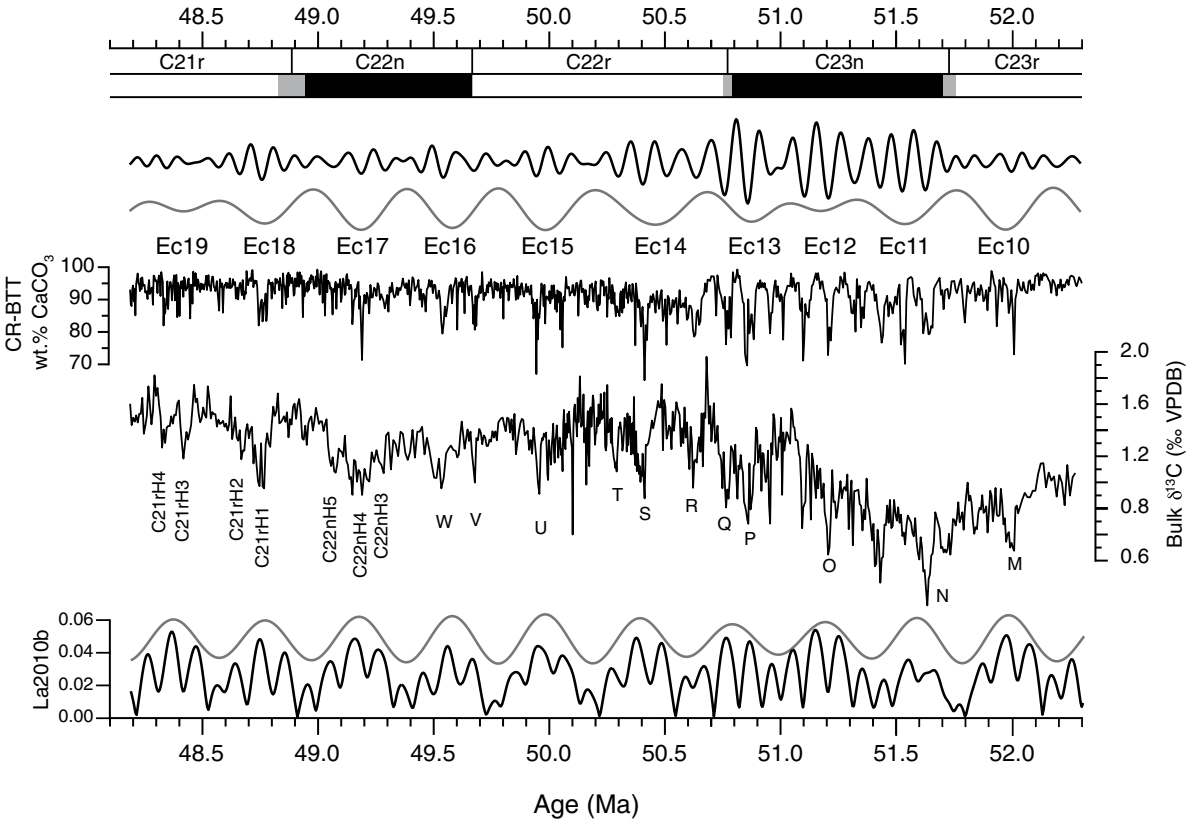

Figure 2.11: *Astrochronologic calibration of the Contessa Road-Bottaccione composite sections plotted against chemostratigraphic and magnetostratigraphic records. The tuning has been performed using the ~4 m (E1) component. The lower panel represents the short eccentricity (black line) and long eccentricity (grey line) components extracted from the La2010b (Laskar et al., 2011a) astronomical solution. All components are reported in time domain.*

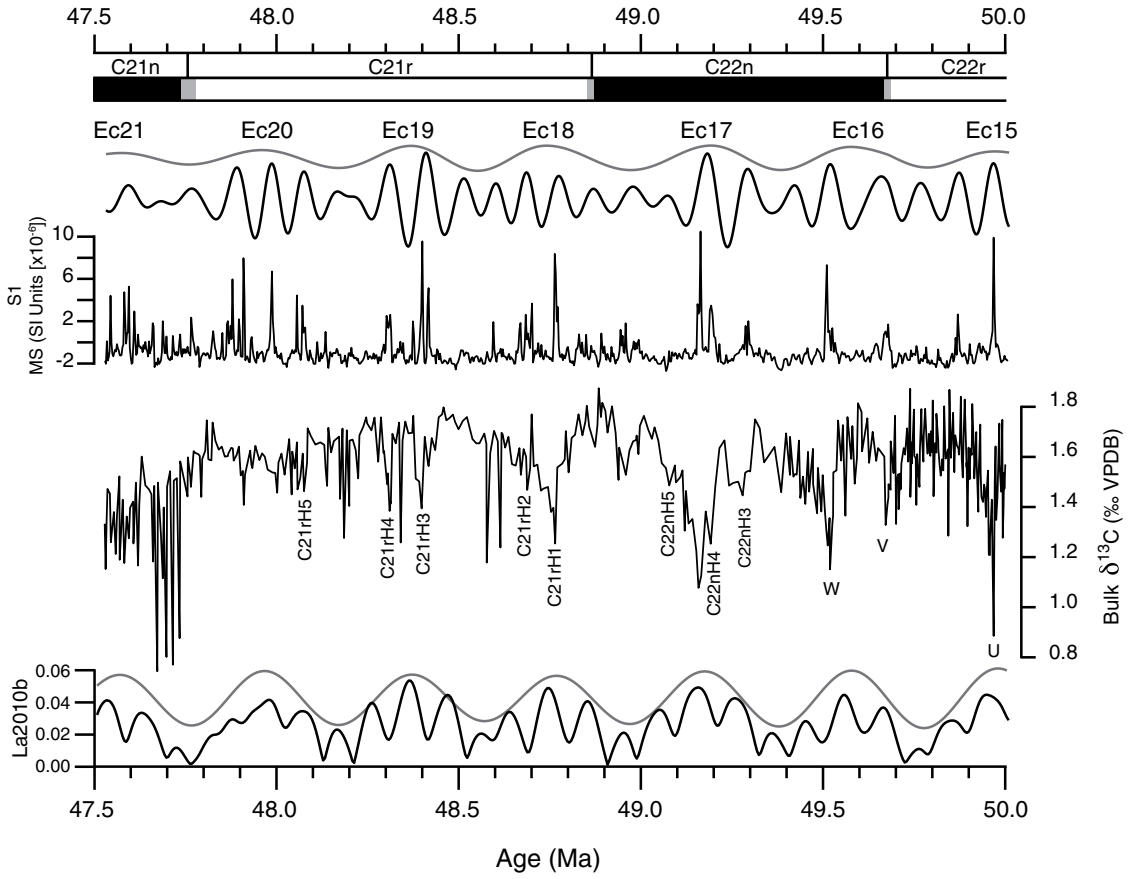

Figure 2.12: *Astrochronologic calibration of the Smirra 1 core together with the bulk carbon isotope and magnetostratigraphic records. The tuning has been performed using the ~360 cm (E1) component. The lower panel represents the short eccentricity (black line) and long eccentricity (grey line) from the La2010b (Laskar et al., 2011a) orbital solution.*

2.7.2 Seafloor Spreading Rates

The U-M age model was tested by plotting seafloor spreading rate curves associated with different spreading centers in the Indian, North Pacific and South Pacific Oceans (Fig. 2.13). Although the U-M age model encompasses only Chrons C21n to C24n, spreading curves were computed for Chrons C19r to C26n after merging our new age model with the ages from Wetal17 (from Chrons C19r to C20r) and GTS2012 (from Chrons C24r to C26n - see Table 2.1). For comparison, we also present similar spreading rate curves using the CK95, GTS2004, GTS2012, and Wetal17 (merged with GTS2012 from Chrons C24r to C26n) age models.

Chron	CK95	GTS2004	GTS2012	Wetal17*	This study†
C19r $_{(base)}$	42.536	41.590	42.301	42.196	42.196
C20n $_{(base)}$	43.789	42.774	43.432	43.507	43.507
C20r $_{(base)}$	46.264	45.346	45.724	46.235	46.235
C21n $_{(base)}$	47.906	47.235	47.349	47.834	47.760
C21r $_{(base)}$	49.037	48.599	48.566	48.994	48.878
C22n $_{(base)}$	49.714	49.427	49.344	49.695	49.666
C22r $_{(base)}$	50.778	50.730	50.628	50.777	50.767
C23n.1n $_{(base)}$	50.946	50.932	50.835	50.942	50.996
C23n.1r $_{(base)}$	51.047	51.057	50.961	51.025	51.047
C23n.2n $_{(base)}$	51.743	51.901	51.833	51.737	51.724
C23r $_{(base)}$	52.364	52.648	52.620	52.628	52.540
C24n.1n $_{(base)}$	52.663	53.004	53.074	52.941	52.930
C24n.1r $_{(base)}$	52.757	53.116	53.199	53.087	53.020
C24n.2n $_{(base)}$	52.801	53.167	53.274	53.123	53.120
C24n.2r $_{(base)}$	52.903	53.286	53.416	53.403	53.250
C24n.3n $_{(base)}$	53.347	53.808	53.983	53.899	53.900
C24r $_{(base)}$	55.904	56.665	57.101	57.101	57.101
C25n $_{(base)}$	56.391	57.180	57.656	57.656	57.656
C25r $_{(base)}$	57.554	58.379	58.959	58.959	58.959
C26n $_{(base)}$	57.911	58.737	59.237	59.237	59.237

Note: CK95—Cande and Kent (1995); GTS2004—Geological Time Scale 2004 (Ogg and Smith, 2004); GTS2012—Geological Time Scale 2012 (Ogg, 2012; Vandenberghe et al., 2012); Wetal17—Westerhold et al. (2017); this study—Contessa Road–Bottaccione composite section and Smirra 1 core.

*Westerhold et al. (2017) merged with GTS2012 from chron C24r to chron C26n.

†CR-BTT and S1 merged with Westerhold et al. (2017) from chron C19r to chron C20r and GTS2012 from chron C24r to chron C26n.

Table 2.1: *Age of magnetochron boundaries according to different authors: CK95: Cande and Kent (1995); GTS2004: Geological Time Scale 2004 (Ogg and Smith, 2004); GTS2012 (Ogg, 2012; Vandenberghe et al., 2012); Wetal17: Westerhold et al. (2017); This study (Contessa Road-Bottaccione composite section and Smirra 1 core).*

Chron	CIR*	SEIR*	WR	PFR	PAR	PALR
C19r	0	2 (2-0)	0	24	6	0
C20n	2 (0–2)	3 (3–0)	1	25	6	0
C20r	2 (0–2)	3 (3–0)	3	35	6	1
C21n	1 (0–1)	5 (5–0)	3	36	7	1
C21r	4 (2–2)	8 (7–1)	3	38	7	1
C22n	5 (2–3)	10 (7–3)	3	41	7	1
C22r	6 (2–4)	6 (4–2)	2	38	7	1
C23n	10 (3–7)	8 (5–3)	3	34	7	2
C23r	13 (5–8)	10 (5–5)	1	29	6	3
C24n.1n	12 (5–7)	9 (6–3)	3	28	5	3
C24n.1r–C24n.2r	12 (5–7)	9 (6–3)	3	28	5	3
C24n.3n	14 (5–9)	9 (6–3)	2	27	5	3
C24r	9 (4–5)	4 (2–2)	3	23	8	1
C25n	13 (3–10)	9 (4–5)	4	23	10	2
C25r	11 (3–8)	8 (4–4)	5	23	10	2
C26n	12 (4–8)	8 (4–4)	6	29	11	2

Note: CIR—Central Indian Ridge; SEIR—South East Indian Ridge, WR—Wharton Ridge; PFR—Pacific-Farallon Ridge; PAR—Pacific Antarctic Ridge; PALR—Pacific Aluk Ridge.

*Number of profiles for north and south flank are given in parentheses.

Table 2.2: *Number of profiles used for different magnetochrons.*

Figure 2.13 shows that spreading rates deduced from the chron width database of Bouligand et al. (2006) are generally consistent with spreading rate curves based on rotation parameters (Cande and Patriat, 2015; Wright et al., 2016b); 95% confidence intervals generally overlap. Differences are nevertheless observed and can be due to the higher temporal sampling in the Bouligand et al. (2006) database, to small changes in spreading direction not taken into account in Bouligand et al. (2006), to the small number of profiles available for some chrons and areas in Bouligand et al. (2006; see Table 2.2), or to the distance between the flowlines used to predict the spreading rates from rotational parameters and the areas selected in Figure 2.2. For instance, data used for the Pacific Antarctic Ridge (PAR) in Figure 2.2 are located north of the data and flowline used by Wright et al. (2016b). Note that spreading rate curves deduced from Cande and Patriat (2015) and Wright et al. (2016b) show only minor differences when computed for the recent U-M or Wetal17 age models, but significant differences when computed with previous age models (CK95, GTS2004, GTS2012). On the other hand, spreading curves obtained using the database of Bouligand (2006) show significant differences for the U-M and Wetal17 age models, due to the higher temporal sampling. In the following, we will therefore only discuss the curves deduced from Bouligand et al. (2006).

Large temporal variations of seafloor spreading rates (by up to a factor of ~4) and of their uncertainty (represented by the 95% confidence intervals) are observed for all spreading centers (Fig. 2.13). The spreading rate uncertainty might be due both to uncertainties in reversal location and local variability in the seafloor spreading rate. Abrupt changes in spreading rates and larger than 95% confidence intervals are also often observed for short chrons, as their width and duration are characterized by larger relative uncertainties and also short-term variability in spreading rates may not have been averaged out due to the short duration of the chron. As noted earlier, our method for locating geomagnetic reversals is inadequate for reversals bounding chrons that are shorter than the spatial resolution of the sea-surface magnetic profiles (~5000 m). For such chrons, our method would tend to artificially increase the apparent chron width and spreading rate. We note however that the spreading rates in Figure 2.13 associated with short chrons, such as C25n or C26n, do not appear to be systematically higher, suggesting that these polarity events are not below the resolution of our sea-surface magnetic profiles.

Although the evolution of seafloor spreading rates shows significant differences among the different spreading centers (especially when considering different oceans), we observe the existence of large deviations in spreading rates that are synchronous for all spreading centers, suggesting that these variations are not real, but instead reflect errors in the polarity time scale, which will be discussed further below. The spreading rate evolution deduced from the U-M age model shows significant differences from the evolution predicted by other polarity timescales. In particular, the new age model suggests the existence of periods of relatively constant spreading rates separated by rapid variations of spreading rate, while other

age models suggest a rather gradual evolution of spreading rates (see for instance the C22n-C24n.1n for the Pacific Farallon Ridge and C22r-C24n.1n for the South East Indian Ridge).

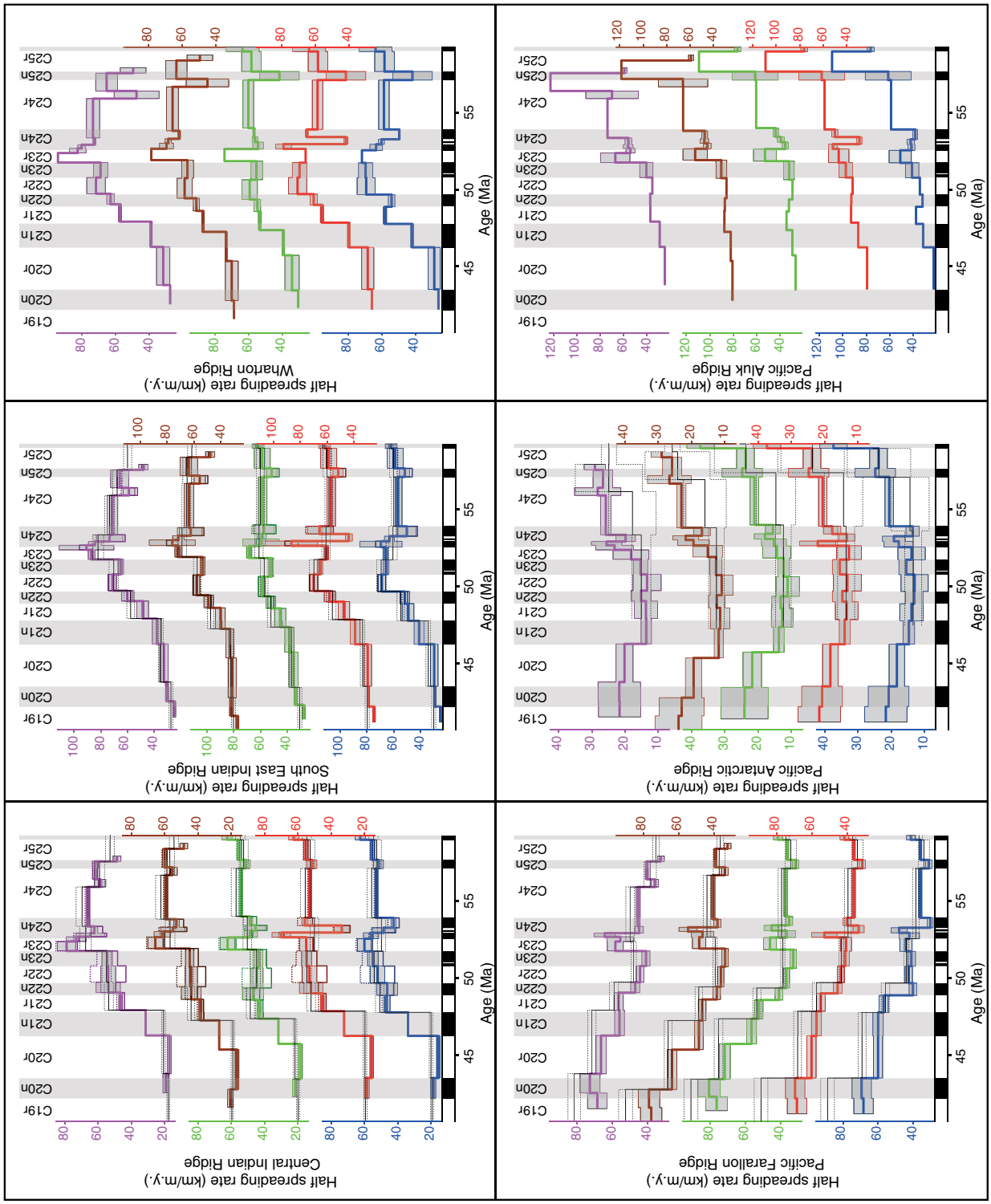

Figure 2.13: *Colored curves and grey bands represent averaged half-spreading rates and 95% confidence*

intervals deduced from the magnetic profiles located in areas defined in Figure 2.2 and according to the age model of different authors (ordered from top to bottom): Cande and Kent (1995 - pink line), GTS2004 (brown line), GTS2012 (green line), Westerhold et al. (2017 - red line) and this study (Contessa Road-Bottaccione composite section and Smirra 1- blue line). Number of profiles used for each area and magnetochron are reported on Table 2.2. Note that 95% confidence intervals deduced from a small number of profiles may be artificially small and not representative of the overall spatial spreading rate variability and uncertainty. For CIR and SEIR, the dark thick curves show the spreading rates associated with the north (solid line) and south (dotted lines) flanks. Black solid and dotted lines represent published spreading rate curves and their 95% confidence interval deduced from rotation parameters that have been adjusted to each age model (CIR and SEIR from Cande and Patriat (2015) and PFR and PAR from Wight et al. (2016b)).

2.8 DISCUSSION

The U-M age model is compared to other radioisotopic and astronomically calibrated age models. Cyclochronological interpretation of magnetochron C22r from the U-M basin is consistent with the estimate proposed by CK95, on the basis of anomaly profiles, which, in turn, agrees with the new estimate of Wetal17 from ODP Site 1258. This number is slightly different from that in GTS2004 and GTS2012, both proposing a ~300 kyr longer duration for C22r. Cycle-counting across magnetochron C22n, whose duration is 710 kyr at S1 and 700 kyr at BTT, is slightly shorter with respect to the estimate of GTS2004 (<100 kyr). Moreover, in our cyclochronological interpretation, C21r is in line with the duration proposed in GTS2012 but has a ~100 kyr longer duration compared to CK95 and Wetal17, while it is slightly shorter with respect to GTS2004. The cyclochronological duration and the astrochronological ages of magnetochron boundaries and individual CIE events are reported in Tables 2.3, 2.4 and 2.5, along with previous estimates proposed by other authors. Compared to Galeotti et al. (2017), to which our time scale is tied via the astronomical age of the C23r/C23n magnetochron boundary (i.e. 51.78 Ma in Galeotti et al., 2017, slightly modified to 51.72 Ma), the age of some events around the C23n/C22r magnetochron boundary are different as the shape of the 405–kyr filter changes based on the observation of a large sedimentation rate increase at the base of Chron C22r. The largest differences with the most recent astrochronological estimates of Wetal17 and Lauretano et al. (2016) are limited to one short eccentricity cycle across C23n.2nH1, C22rH3, C21rH1 and C21rH2 events. Considering the good match between our astrochronology and that of Wetal17 at the resolution of the 405–kyr cycles, the slightly different ages of these hyperthermal events can be ascribed to a slightly different interpretation of the relative position of individual geochemical events within each long eccentricity cycle. In the absence of a stable solution of short eccentricity for the studied time interval, this level of discrepancy is unavoidable. The astrochronological ages of the magnetochron boundaries show a very satisfactory match between our estimates and Wetal17, with moderate discrepancies at the C22n/C21r and C21r/C21n magnetochron boundaries that, in our astrochronological model, are 100 kyr younger than reported by Westerhold et al. (2017).

Chron	Standard GPTS			Cycle counting	Astronomically calibrated		Cycle counting*		Astronomically calibrated†	
	CK95	GTS 2004	GTS 2012	Lau3c§	Wetal17	Galetal17#	Bottaccione	Smirra 1	Bottaccione	Smirra 1
C21r	1131	1364	1217	N.D.**	1161	N.D.**	N.D.**	1200	N.D.**	1110
C22n	677	828	778	N.D.**	700	N.D.**	700	710	770	800
C22r	1064	1303	1284	N.D.**	1082	N.D.**	1010	N.D.**	1100	N.D.**
C23n	965	1171	1205	676	961	1180	1000	N.D.**	950	N.D.**
C23r	621	747	787	1016	890	760	840	N.D.**	820	N.D.**
C24n.1n	299	356	454	458	314	390	420#	N.D.**	390#	N.D.**
C24n.1r	94	112	125	162	145	90	N.D.**	N.D.**	90#	N.D.**
C24n.2n	44	51	75	67	36	100	N.D.**	N.D.**	1000#	N.D.**
C24n.2r	102	119	142	142	280	130	N.D.**	N.D.**	130#	N.D.**
C24n.3n	444	522	567	561	496	650	630#	N.D.**	650#	N.D.**
C24n $_{(total)}$	983	1160	1363	1390	1271	1360	1417#	N.D.**	1360#	N.D.**

Note: GPTS—geomagnetic polarity time scale; CK95—Cande and Kent (1995); GTS2004—Geological Time Scale 2004 (Ogg and Smith, 2004); GTS2012—Geological Time Scale 2012 (Ogg, 2012; Vandenberghe et al., 2012); Lau3c—three-cycle option of Lauretano et al. (2016); Wetal17—Westerhold et al. (2017); Galetal17—Galeotti et al. (2017).

*Floating time scale.

†Calibrated to Laskar 2010b astronomical solution (Laskar et al., 2011a).

§Three-cycle option taken from Lauretano et al. (2016).

#Galeotti et al. (2017).

**N.D.—not determined.

Table 2.3: *Estimated duration (kyr) of individual magnetochrons for the surveyed interval according to different authors: CK95: Cande and Kent (1995); GTS2004: Geological Time Scale 2004 (Ogg and Smith, 2004); GTS2012: Geological Time Scale 2012 (Ogg, 2012; Vandenberghe et al., 2012); Lau3c: 3–cycle option of Lauretano et al., (2016); Wetal17: Westerhold et al. (2017); Galetal17: Galeotti et al. (2017); This study (Contessa Road-Bottaccione composite section and Smirra 1).*

Chron	CR-BTT	S1	Wetal17
C21n $_{(base)}$	N.D.*	47.76	47.834
C21r $_{(base)}$	48.89	48.87	48.994
C22n $_{(base)}$	49.66	49.67	49.695
C22r $_{(base)}$	50.77	N.D.*	50.777
C23n $_{(base)}$	51.72	N.D.*	51.737
C23r $_{(base)}$	52.54	N.D.*	52.628
C24n.1n $_{(base)}$	52.93	N.D.*	52.941
C24n.1r $_{(base)}$	53.02	N.D.*	53.087
C24n.2n $_{(base)}$	53.12	N.D.*	53.123
C24n.2r $_{(base)}$	53.25	N.D.*	53.403
C24n.3n $_{(base)}$	53.90	N.D.*	53.899

Note: Age of magnetochron boundaries are listed according to this study (Contessa Road-Bottaccione section [CR-BTT] and Smirra 1 core [S1]) and most recent astrochronological estimates of Wetal17 (Westerhold et al., 2017).

*N.D.—not determined.

Table 2.4: *Age of magnetochron boundaries according to this study (Contessa Road-Bottaccione section and Smirra 1) and the most recent astrochronological estimates of Wetal17 (Westerhold et al., 2017).*

Event	CR-BTT	S1	Lau3c*	Wetal17
PETM	56.10	N.D.†	N.D.†	55.93
ETM2	54.09	N.D.†	54.14	54.05
ETM3	52.80	N.D.†	52.83	52.84
L, C23rH1	52.44	N.D.†	52.41	52.46
M, C23rH2	52.00	N.D.†	51.88	51.97
N, C23n.2nH1	51.63	N.D.†	51.55	51.55
O, C23n.2nH2	51.21	N.D.†	51.28	51.23
P, C23n.1nH1	50.85	N.D.†	50.80	50.86
Q, C22rH1	50.76	N.D.†	50.73	50.76
R, C22rH2	50.62	N.D.†	50.63	50.67
S, C22rH3	50.40	N.D.†	50.47	50.48
T, C22rH4	50.29	N.D.†	50.32	50.37
U, C22rH5	49.96	49.96	49.96	49.95
V, C22nH1	49.67	49.67	49.70	49.68
W, C22nH2	49.53	49.52	49.6	49.58
C22nH3	49.29	49.29	N.D.†	49.38
C22nH4	49.19	49.19	N.D.†	49.25
C22nH5	49.08	49.07	N.D.†	49.14
C21rH1	48.76	48.77	N.D.†	48.85
C21rH2	48.66	48.69	N.D.†	48.76
C21rH3	48.41	48.40	N.D.†	48.45
C21rH4	48.32	48.31	N.D.†	48.36
C21rH5	N.D.†	48.08	N.D.†	48.07

Note: Age of hyperthermal events are listed according to this study (Contessa Road–Bottaccione section [CR-BTT] and Smirra 1 [S1] core) and the most recent astrochronological estimates of the three-cycle option of Lau3c (Lauretano et al., 2016) and Wetal17 (Westerhold et al., 2017). PETM—Paleocene-Eocene thermal maximum; ETM2—Eocene thermal maximum 2; ETM3—Eocene thermal maximum 3; L–W—carbon isotope excursions according to Cramer et al. (2003) and Lauretano et al. (2016).

*Three-cycle option taken from Lauretano et al. (2016).

†N.D.—not determined.

Table 2.5: *Age of hyperthermal events according to this study (Contessa Road-Bottaccione section and Smirra 1) and the most recent astrochronological estimates of the 3–cycle option of Lau3c (Lauretano et al., 2016) and Wetal17 (Westerhold et al., 2017).*

In order to identify possible errors in the age models, we compare the spreading rate curves for different spreading centers as calibrated with different time scales (Fig. 2.13). In particular, large variations in spreading rates that are synchronous for all investigated spreading centers within the Indian and Pacific Oceans are unlikely and probably point to errors in the age models. As shown in Figure 2.13, Chron C23r is systematically characterized by a higher spreading rate for CK95, GTS2004 and GTS2012, suggesting that the duration of this chron is too short in these age models. On the other hand, the Wetal17 and U-M age models suggest a shorter duration for Chron C23r and do not show such a systematic increase in spreading rates associated with C23r. However, these two age models show rapid changes in spreading rate during Chron C24n among all spreading centers, suggesting errors in the subchron durations. In particular, the ages of Wetal17 lead to very fast oscillations in spreading rate during this chron, whereas the U-M age model shows a systematic decrease in spreading rate for Chron C24n.3n. However, it must be taken into account that these discrepancies in the U-M age model could be due to the sampling resolution, which is very close to the short duration of the subchrons.

The duration of subchrons within C24n and C23n is further investigated through a comparison of stacks of magnetic profiles and synthetic profiles deduced from the different age models (Fig. 2.14; Table 2.6). This comparison is only performed for the South East Indian Ridge (SEIR), Central Indian Ridge (CIR) and Wharton Ridge (WR) in the Indian Ocean and for the Pacific Aluk Ridge (PALR) in the South Pacific Ocean (see locations on Fig. 2.2), which are the only areas where the spreading rate is high enough to distinguish the anomalies associated with subchron C24n.2n. We first note that the synthetic profiles deduced from the previous polarity timescales CK95, GTS2004 and GTS2012 reproduced already very well the stacks of profiles, especially in the CIR and SEIR (Pearson correlation coefficient >0.9). This is due to the fact that the durations of short events in Chrons C23n and C24n for these polarity time scales were derived using the sequence of magnetic anomaly widths compiled by Cande and Kent (1992), which for Chrons C23n and C24n are based on a stack of two profiles from CIR and SEIR in the Indian Ocean. However, we notice some differences, the most obvious being the larger amplitude of anomaly C23n.1r in the synthetic profiles, suggesting that the duration of C23n.1r is too long in CK95, GTS2004 and GTS2012. Such discrepancies are due to the fact that only two magnetic profiles were used to constrain the duration of C23n and C24n subchrons in these time scales, while we use stacks composed of a larger number of profiles (see number of profiles in Table 2.2). Looking now at the synthetic profiles deduced from the U-M age model, we see that this age model best reproduces the amplitude and location of the C23n.1r anomaly observed in the stacks (black dashed and solid curves) from the Indian Ocean compared to the other age models (largest Pearson correlation coefficient for C23n obtained with the U-M age model in Table 2.6). On the other hand, the synthetic profiles deduced from the U-M age model for Chron C24n show significant differences with the observed stacks (with slightly lower Pearson correlation coefficients for C24n obtained with the U-M age model than with CK95, GTS2004 and GTS2012). In particular, we observe that the synthetic anomaly associated with C24n.2n has an amplitude about twice as large and is shifted toward younger ages compared to the stacks from the Indian Ocean. The difference in amplitude suggests that the duration of C24n.2n in the U-M age model (100 kyr) is about twice too long, although this discrepancy could also be partly due to a lower intensity of the Earth's magnetic field during the short polarity event C24n.2n. Note, however, that, because of a sampling resolution of ~30 cm for magnetostratigraphic samples, the uncertainty is ~25 kyr, which may explain some of the discrepancies. With respect to the temporal shift of C24n.2n, we notice that Chron C24n corresponds to a period of increase in spreading rates at SEIR, CIR and WR (Fig. 2.13). Since synthetic profiles in Figure 2.14 are computed assuming a constant spreading rate, the temporal shift of C24n.2n between the synthetic profiles and stacks might just reflect this increase in spreading rate. This is confirmed by the stack obtained for PALR, whose location of anomaly C24n.2n is more consistent with the U-M age model (Fig. 2.14; Table 2.6). A better estimation of the duration of subchrons within C24n would however require a detailed magnetostratigraphic study with a much higher sampling resolution, while the resulting durations could be tested with the use of high-

resolution near-bottom marine magnetic profiles (as is done for instance by Bowles et al., 2003 for chron C5).

The refinement of the polarity timescale and of the spreading rate curves during the early to middle Eocene is important for a better understanding of the cause of the seafloor spreading evolution during this period. Indeed, major absolute and relative plate motion changes are observed worldwide around 50 Ma (e.g., Müller et al., 2016). This includes for instance a significant decrease in spreading rates followed by a reorganization of spreading centers in the Indian Ocean near the onset of India-Eurasia collision (Patriat and Achache, 1984; Patriat and Segoufin, 1988; Cande and Patriat, 2015) and an increase of the Pacific-Farralon spreading rates following the complete subduction of the Izanagi plate (Whittacker et al. 2007; Seton et al., 2015) and the initiation of the Izu-Bonin-Mariana subduction (Arculus et al., 2015). The bend in the Hawaii-Emperor chain occurred also near the same period, possibly reflecting both a change in the motion of the Hawaiian hotspot and in plate motion (Tarduno, 2007; Wright et al., 2015; Wilson, 2016; Wright et al., 2016a). Finally, ~50 Ma also coincides with the Early Eocene Climatic Optimum characterized by very high temperatures and pCO_2, followed by a long-term decrease in temperatures and pCO_2 during the Eocene (e.g., Zachos et al., 2001). Refinement of the polarity time scale is therefore critical to address important research questions such as the consequence of the worldwide plate motion reorganization for ocean chemistry, atmospheric pCO_2 and global climate on the long-term (10^6 yr) time scale (e.g., Kasting and Richardson, 1985; Rea et al., 1990; Müller et al. 2013, 2014; Norton and Lawver, 2014).

The U-M age model suggests a significantly different evolution of seafloor spreading rates than other age models (Fig. 2.13). In the Indian Ocean, the new age model suggests a period of constant spreading rate during Chrons C23r to C22r, followed by a decrease in spreading rates after $C22n_{(base)}$ (~50 Ma) for the South East Indian Ridge (SEIR) and Wharton Ridge (WR). For the Central Indian Ridge (CIR), spreading rate seems to slowly decrease from C23r to C21r, followed by a faster decrease after $C21n_{(base)}$ (~48 Ma). In the North Pacific Ocean, the new age model suggests stepwise changes in spreading rates for the Pacific-Farallon Ridge (PFR) with the existence of several periods of constant spreading rates (Chrons C24n.1n to C22n, Chrons C21r to C20r, and possibly Chrons C26n to C24r) separated by rapid changes in spreading rates (around $C21r_{(base)}$, i.e. ~49 Ma, and $C24n.2r_{(base)}$, i.e. ~53 Ma). These results tend to confirm that large oceanic plates are characterized by short periods of rapid changes separating long periods of constant or slowly changing spreading rates, as suggested by Wilson (1993) and Krijgsman et al. (1999) for the last 10 Myr. Defining the timing of changes in spreading rates (long-term versus abrupt changes) is of particular interest as it might be an indicator of the different mechanisms involved (ridge-plume interactions versus tectonic collision events).

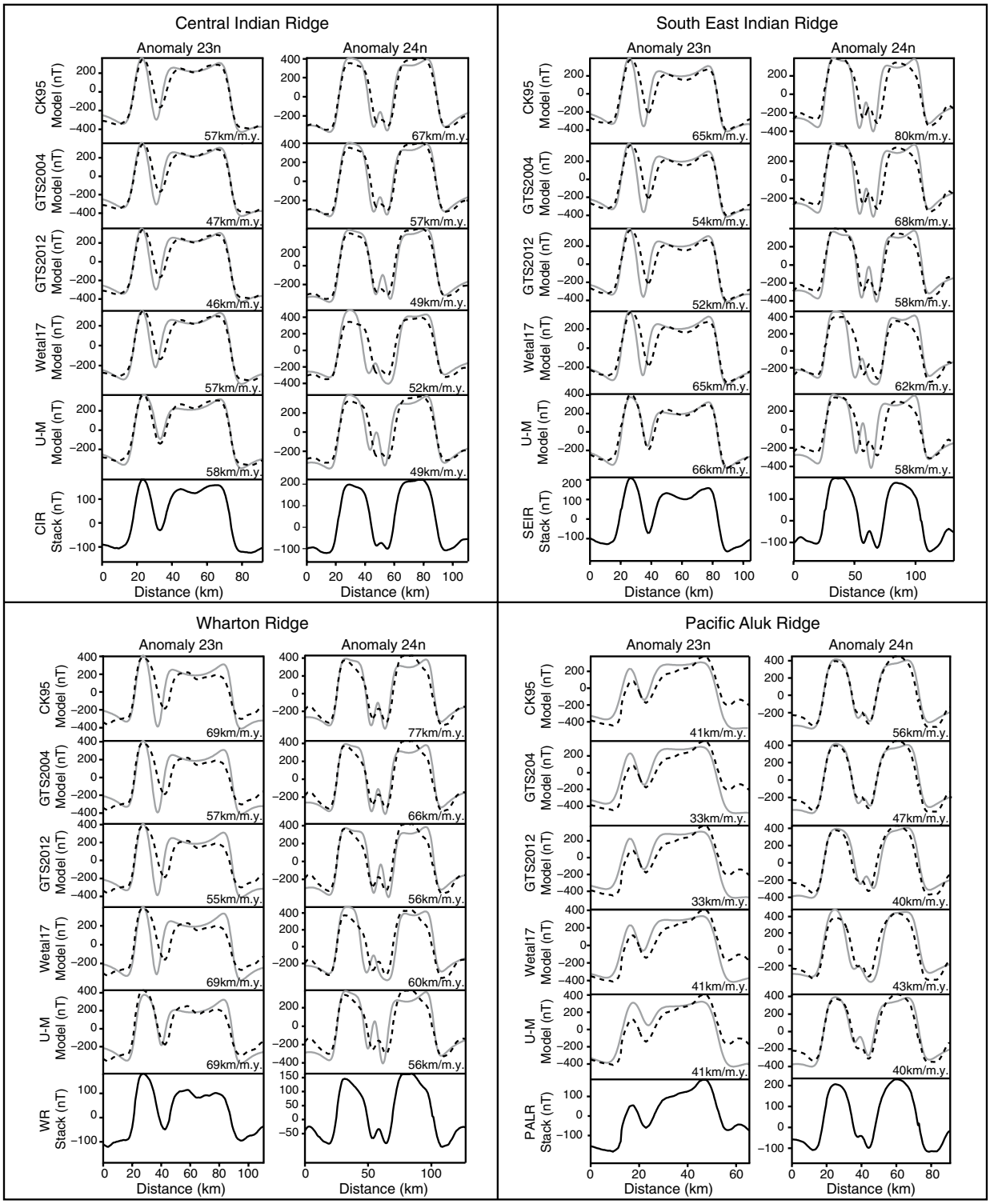

Figure 2.14: *Comparison of stacks of marine magnetic profiles (black solid curves) from areas CIR SEIR, WR and PALR with synthetic anomaly profiles (grey solid curves) for Chrons C23n and C24n. The synthetic profiles are obtained assuming a constant spreading rates (see value on the bottom-right corner of plots) and are predicted for different age models. The black dashed curve corresponds to the stacks after*

multiplying them by a constant factor and adding a constant vertical shift to obtain a best fit to the synthetic profiles in the least-square sense.

	C23n				C24n			
	WR	CIR	SEIR	PALR	WR	CIR	SEIR	PALR
CK95	0.86	0.97	0.93	0.85	0.96	0.98	0.91	0.98
GTS2004	0.86	0.97	0.93	0.85	0.96	0.98	0.92	0.98
GTS2012	0.86	0.97	0.93	0.85	0.95	0.98	0.96	0.96
Wetal17	0.85	0.96	0.92	0.87	0.92	0.92	0.90	0.94
U-M	0.94	0.99	0.99	0.85	0.92	0.95	0.85	0.97

Note: Pearson correlation coefficients between stacks and synthetic anomaly profiles are represented in Figure 14. WR—Wharton Ridge; CIR—Central Indian Ridge; SEIR—South East Indian Ridge; PALR—Pacific Aluk Ridge; CK95—Cande and Kent (1995) age model; GTS2004—Ogg and Smith (2004) geologic time scale; GTS2012—Ogg et al. (2012) geologic time scale; Wetal17—Westerhold et al. (2017) age model; U-M—Umbria-Marche Basin age model.

Table 2.6: *Pearson correlation coefficients between stacks and synthetic anomaly profiles represented in Figure 2.14 for WR, CIR, SIR and PALR spreading centers.*

2.9 CONCLUSIONS

The new integrated stratigraphic analysis from the Bottaccione section and Smirra core provides a continuous high-resolution record of the early to middle Eocene, spanning the PETM to the lower part of magnetochron C21n. The carbon isotope analysis of the U-M record allows the detection of carbon isotope excursions and their comparison with similar excursions observed in $\delta^{13}C$ records of other deep-sea settings, i.e. ODP Site 1258 and ODP Site 1263. The alignment of carbon isotope stratigraphies for the entire interval spanning C24r to C21n shows a very good match, reflecting the global dynamics of the carbon cycle, both on short- and on long-time scales. The lack of the C22rH3 and C22rH4 events at Smirra is interpreted to reflect a stratigraphic gap in magnetochron C22r.

Moreover, astronomically induced cyclicity has been detected in the wt.% $CaCO_3$ of the Bottaccione section (from C22r to C21r magnetochron interval) and the MS record of the Smirra core (for the interval between C22r and C21r magnetochrons). The eccentricity related cycles in the proxy records of the overlapping interval between the two U-M sites reveal a very good match. These cycles were used to develop a floating cyclochronology and extend the existing astronomically calibrated age model for the U-M basin by 2.3 million years up to 47.5 Ma. This allows a comparison of the duration and the age of individual magnetochrons and events with other radioisotopic and astronomically calibrated age models. The astrochronological estimates across C22r and C21r magnetochrons reveal durations that are in line with the estimates proposed by CK95 and Wetal17, but are shorter with respect to GTS2004 and GTS2012. Magnetochron C22n, instead, is slightly shorter than in GTS2004, but in agreement with estimates in CK95, GTS2012 and Wetal17.

Spreading rates deduced from the U-M model do not display large deviations that are correlated among the different ocean basins, with the exception of the subchrons in C24n that will require a higher-resolution magnetostratigraphy to be resolved. We therefore conclude that the U-M basin records provide a valuable cyclochronological and astrochronological estimate for the duration of the interval spanning ~56 to ~47 Ma.

The seafloor spreading rates deduced from the new age model suggest a significantly different evolution compared to other age models, and in particular point to the existence of rapid variations separating long period of constant or slowly varying spreading rates. Refining the timing of these spreading rate changes is very important as it may help determine the causative mechanism for such changes, especially around ~50 Ma, a period of worldwide changes in the seafloor spreading, which also coincides with the beginning of a long-term decrease in temperature and atmospheric pCO_2.

Acknowledgments

This research benefited from funds provided by MIUR-PRIN grant 2010X3PP8J_005 to SG and 2010X3PP8J_004 to MS, by PhD Grant of the Italian Minister for Research to FF, by NWO-ALW grant (project number 865.10.001) to LJL and by NESSC grant 024.002.001 to CS and LJL.

We thank J. Dyment who provided us with the code to compute synthetic profiles of marine magnetic anomalies. We are grateful to the Royal Netherlands Institute for Sea Research (NIOZ) and Rineke Gieles for technical help and analytical support. We thank Arnold van Dijk at Utrecht University for technical support. The database of magnetic anomaly picks from Bouligand et al. (2006) that we used in this study to construct spreading rate curves will be posted online at https://hal.archives-ouvertes.fr/hal-01812932. During the course of this study, C. Bouligand was a visiting scientist at the U.S. Geological Survey in Menlo Park, CA, USA and benefited from a CRCT from CNU (section 35) and a delegation to CNRS. ISTerre is part of Labex OSUG@2020 (ANR10 LABX56).

Chapter III

STRATIGRAPHY OF EARLY TO MIDDLE EOCENE HYPERTHERMALS FROM POSSAGNO, SOUTHERN ALPS (ITALY) AND COMPARISON WITH GLOBAL CARBON ISOTOPE RECORDS

Galeotti Simone, Sprovieri Mario, Rio Domenico, Moretti Matteo, Francescone Federica, Sabatino Nadia, Fornaciari Eliana, Giusberti Luca, Lanci Luca

To be submitted to Palaeogeography, Palaeoclimatology, Palaeoecology

ABSTRACT: The late early Eocene to middle Eocene ~51–45 Million years ago (Ma) time interval in the middle bathyal, pelagic/hemipelagic succession of the western Tethys Possagno section in the Carcoselle quarry (Southern Alps, northeastern Italy), contains several episodes of negative carbon isotope excursions (CIEs) and concomitant dissolution of carbonates. Comparison with previously published carbon isotope records from deep-sea successions allows the identification of long-term trends and short-term events in our record, which provides a sound chemostratigraphic basis for correlation against the robust bio- and magnetostratigraphic scheme available for the studied succession.

Spectral analysis indicates that CIEs and associated lithological cycles are paced by orbital forcing, similar to what previously observed on the same interval in other deep-sea successions.

Keywords: Eocene, Possagno, Orbital forcing, Hyperthermals

3.1 INTRODUCTION

A succession of transient global warming events occurred during the late Paleocene and early Eocene, ~59-50 Ma (Agnini et al., 2006; Galeotti et al., 2010; Lourens et al., 2005; Nicolo et al., 2007; Röhl et al., 2007; Zachos et. al., 2005). These short-lived (10^4-10^5 yr) events, known as hyperthermal, are linked to large perturbations of the global carbon cycle recorded by negative carbon isotope excursions (CIEs) in both marine and continental settings and concomitant $CaCO_3$ dissolution in deep-sea sediments (Zachos et al., 2005; Zeebe and Zachos, 2007). Hyperthermals are considered to be caused by successive massive and rapid injections of ^{13}C-depleted carbon into the atmosphere, boosting dramatic warming and causing ocean acidification by pCO_2 re-equilibration across the atmosphere/ocean system. The most important of these events are the Paleocene-Eocene thermal maximum, or Eocene thermal maximum 1 (ETM1) at ca. 56 Ma, ETM2 at ca. 54 Ma, and ETM3 at ca. 52.8 Ma (Agnini et al., 2009; Dunkley-Jones et al., 2013; Galeotti et al., 2010, 2017; Kennett and Stott, 1991; Lourens et al., 2005; Röhl et al., 2004; Sluijs et al., 2008; Tripati

and Elderfield, 2005; Westerhold et al., 2007; Zachos et al., 2005). CIEs, although variable in magnitude, are astronomically forced (Cramer et al., 2003; Francescone et al., 2018; Galeotti et al., 2010, 2015, 2017; Kirtland Turner et al., 2014; Lauretano et al., 2015, 2016; Lourens et al., 2005; Sexton et al., 2011; Westerhold and Röhl, 2009; Westerhold et al., 2015, 2017) and are superimposed on the long-term warming trend that culminates at the Early Eocene Climatic Optimum (EECO) (Galeotti et al., 2017; Zachos et al., 2008). "Hyperthermal-like" events (i.e., CIEs associated with increased temperature and $CaCO_3$ dissolution observed in deep sea successions) have been reported to occur during and after the EECO time interval at Demerara Rise (Ocean Drilling Program - ODP - Site 1258 - Kirtland Turner et al., 2014; Sexton et al., 2011), at Walvise Ridge (ODP Site 1263 – Lauretano et al., 2016), at Shatsky Rise (ODP Site 1209 - Westerhold et al., 2018) and in the Umbria-Marche (U-M) basin (Francescone et al., 2018; Galeotti et al., 2010, 2017). Post-EECO hyperthermals are more numerous than previously documented and paced by the eccentricity of Earth's orbit (Sexton et al., 2011). However, also because of the difficulty of recovering suitable oceanic successions with well-preserved geochemical records across the silica-rich extended EECO interval (the so-called "silica burp" of McGowran, 1989), the occurrence of these events in the $\delta^{13}C$ record has yet to be confirmed at other sites while their orbital chronology needs further investigations (Westerhold et al., 2015). Indeed, different cyclochronological interpretations of the late early Eocene interval, particularly across magnetochrons C23r-C22r, have been proposed recently by different authors (Francescone et al., 2018; Galeotti et al., 2017; Lauretano et al., 2016; Westerhold and Röhl, 2009; Westerhold et al., 2017). For this study, we present a new high-resolution record from Southern Alps in the Possagno section combined with the original data of Agnini et al. (2006) to provide an orbital chronology of CIEs spanning the upper part of magnetochron C24r to the lower part of Chron C20r. The main goal of this work is to provide one more record of the global carbon cycle aberrations captured by CIEs in the surveyed interval and contribute to the astrochronological definition of individual events.

3.2 MATERIAL AND METHODS

3.2.1 Geological setting

A record of the lower Paleocene to middle Eocene is well preserved in the Possagno section located in an active quarry (Carcoselle quarry: 45 51.0' N; 11 51.6'E), very close to the town of Possagno (Treviso province, northern Italy – Fig. 3.1). The Lower Paleocene and the middle part of the Lower Eocene is recorded in the pelagic/hemipelagic red limestone and marl succession of the Scaglia Rosssa Formation (Fm.). The upper part of the Lower Eocene and the Middle Eocene is comprised in the overlying Scaglia Variegata, composed of whitish to greyish marly limestones and marls, followed by clay-rich limestones of the Scaglia Cinerea Fms. The 66 m-tick succession has been originally examined for its stratigraphy by Agnini et al. (2006), with a resolution of one sample every 5-10 cm from -2.5 to 1m, every 20 cm up to the

25 m and every 1-2 m throughout the rest of the section (for further details see Agnini et al., 2006). Good quality bio- and magnetostratigraphic data show that the succession encompasses calcareous nannofossil Zones CNP11-CNE10 of Agnini et al. (2014 – equivalent to NP9-NP15 pars of Martini, 1971) and magnetochrons C24r to C20r. Stable carbon and oxygen isotope data and a detailed description of the evolutionary response of the planktonic foraminiferal to changing environmental conditions from the same section have been presented separately by Luciani et al. (2016). Here we complement the previously published stratigraphic results of Agnini et al. (2006) and Luciani et al. (2016) with a wt.% $CaCO_3$ record from the same section (Fig. 3.2).

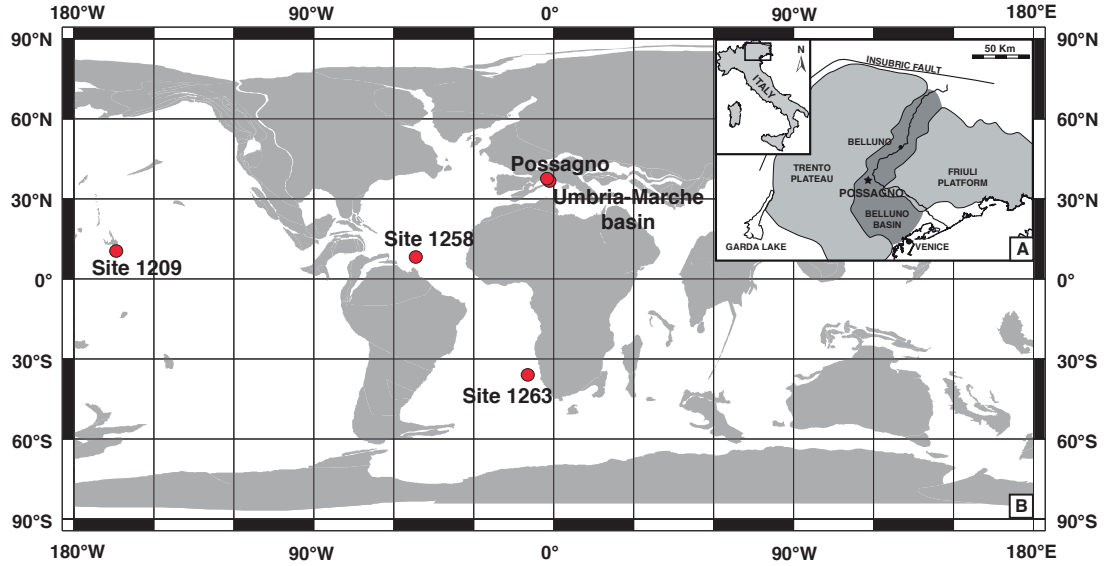

Figure 3.1*: A) The Possagno section is located in the eastern Southern Alps. The section crops out in the Carcoselle quarry, 1.5 km west of the town of Possagno (45°50'2"N, 11°31'1"E). B) Paleogeographic reconstruction for the early Eocene (~54Ma) showing the position of the Possagno section, Umbria-Marche basin, ODP Sites 1263, 1258 and 1209 (map generated at http://www.odsn.de/odsn/services/paleomap/paleomap.html, modified).*

Moreover, a different outcrop located ~200 m away from the original section sampled by Agnini et al. (2006) has been sampled every 5 cm, in order to provide a stable carbon isotope record and wt.% $CaCO_3$ at a higher resolution (Fig. 3.3). The presence of several well-recognizable markers together with a biostratigraphic analyses for selected intervals allows a confident correlation with the original sampling of Agnini et al. (2006). The zero level of this newly sampled outcrop coincides with the top of a characteristic decimetric light green massive limestone bed - informally defined “Aquamarina Bed” (Fig. 3.3) – whose base at Carcoselle marks the transition from Scaglia Rossa to Scaglia Variegata Fms. Such distinctive marker bed was useful for correlating this new profile with the profile originally studied by Agnini et al. (2006).

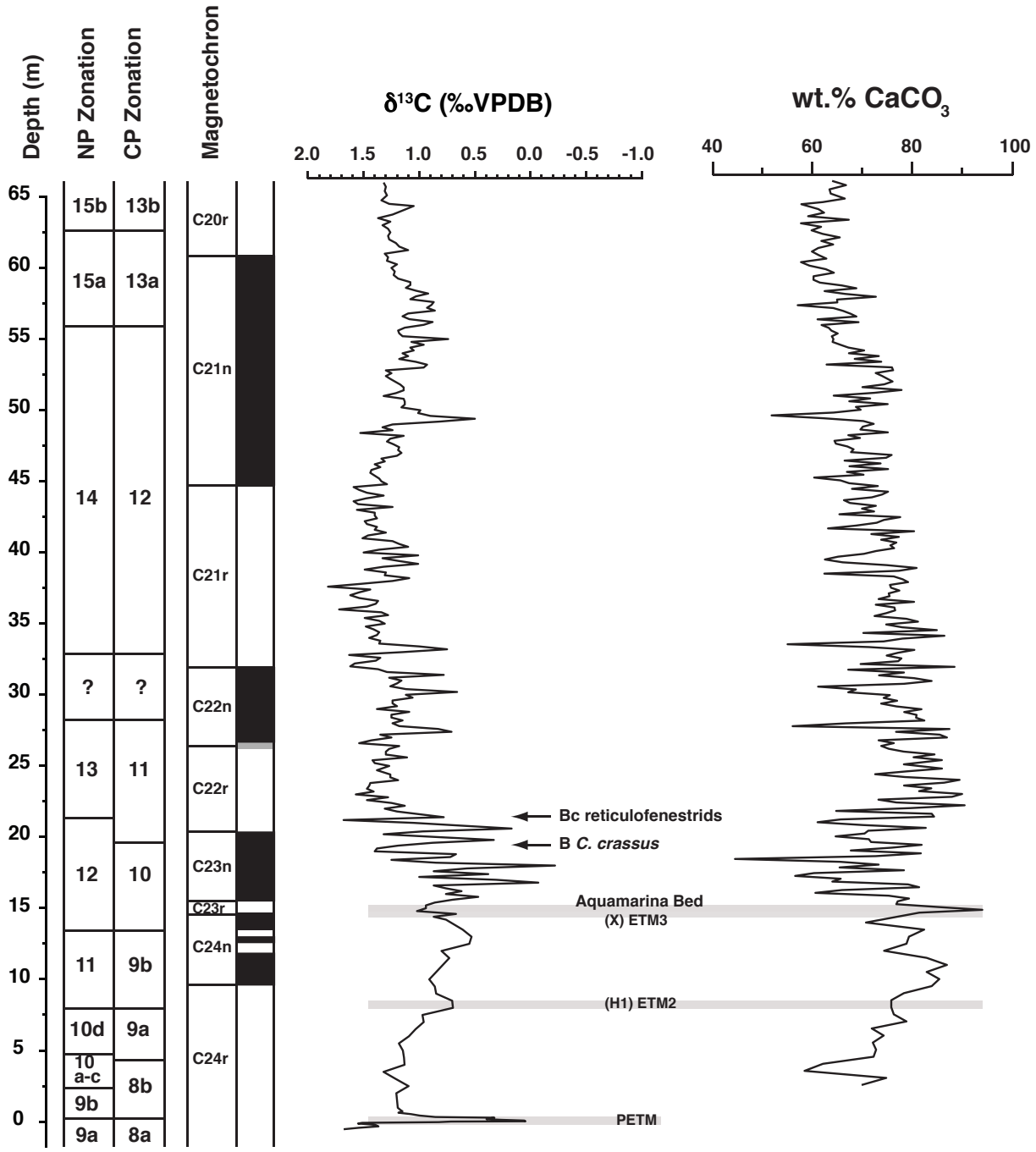

Figure 3.2*: Stable carbon isotope and wt.% $CaCO_3$ records against the lithostratigraphy and bio-magnestratigraphy of the lower-middle Eocene at Possagno derived from the original sampling of Agnini et al. (2006). Depth is in meters from the P/E boundary defined by a ~2‰ negative excursion in the carbon isotope values at the NP9a/NP9B and CP8a/CPb calcareous nannofossil zonal boundary. B C. crassus – Base Coccolithus crassus. Bc Reticulofenestrids – Base common Reticulofenestrids.*

Furthermore, a stratigraphic interval presumably spanning magnetochrons C22r to C18r has been recently cored in the Carcoselle quarry to obtain a high-resolution record spanning the Early Eocene Climatic

Optimum (EECO) to the Middle Eocene Climatic Optimum (MECO). The entire succession has been recovered by drilling 3 holes (Possagno Cores A, B and C) at different topographic heights in October 2014 (Fig. 3.1). Here we present data from the Possagno Core B (Fig. 3.4), which, based on stratimetric assessment in the field and lithostratigraphy, is expected to cover the lowermost portion of the Scaglia Variegata Fm. corresponding to magnetochrons C22r-C22n (Agnini et al. 2006). The bedding, measured in outcropping beds at the top of the drillhole, has a strike of N175°W and an average dip of ~23°ESE.

The record recovered with the Possagno Core B provides a remarkably well preserved, mostly undisturbed, succession, which has been sampled at 5 cm space resolution for geochemical analysis.

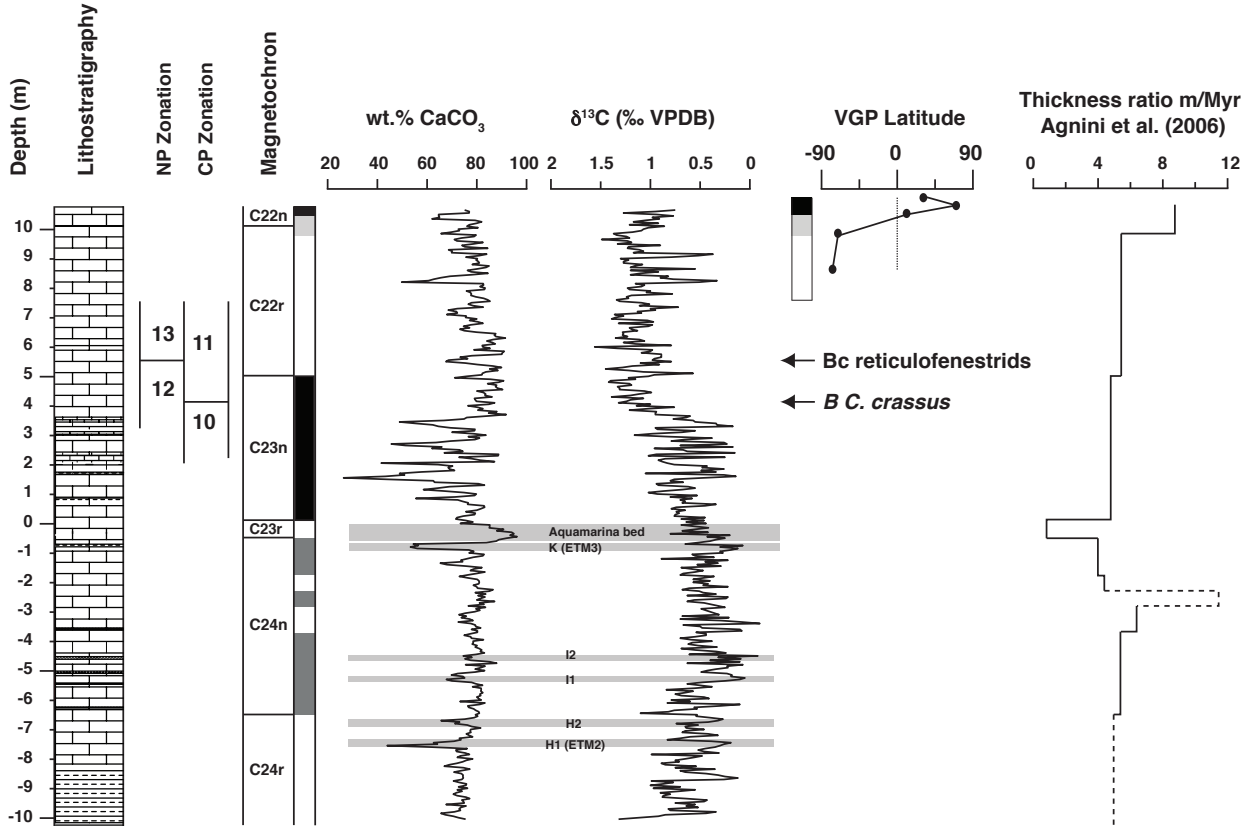

Figure 3.3: *Carbon isotope and wt.% $CaCO_3$ record from the newly sampled outcrop. The position of the C22r/C22n magnetochron has been obtained directly on the new outcrop based on VGP Latitude values from five samples. The position of the C24n (in grey) is only tentatively projected relative to the new sample set. The sedimentation rate within each magnetochron (from Agnini et al., 2006, based on the Global Polarity Time Scale of Cande and Kent, 1995) is also reported.*

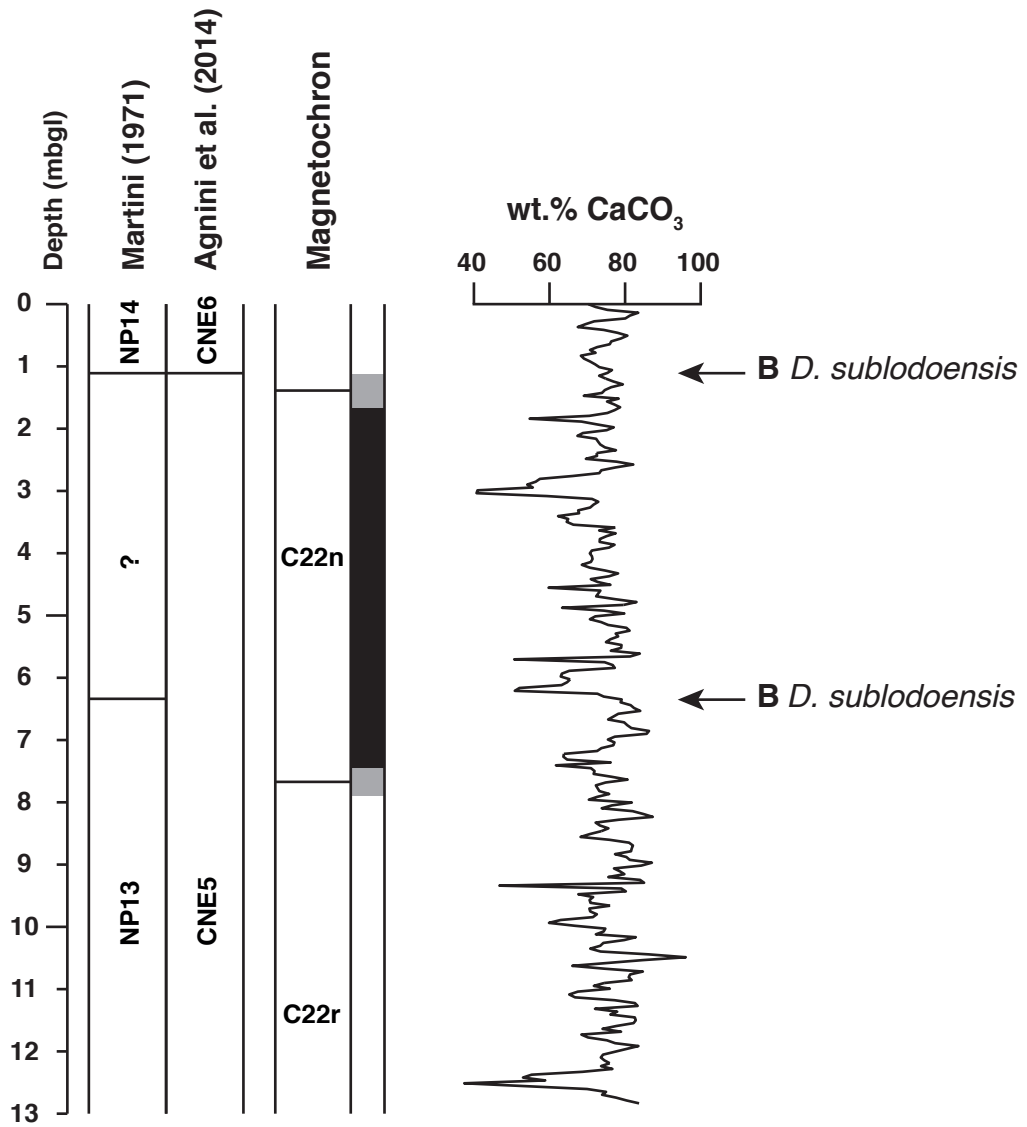

Figure 3.4: *Wt.% $CaCO_3$ record from the Possagno Core B, plotted against magnetostratigraphy and biostratigraphy. Depth is reported in meters below ground level (mbgl) to bottom core.*

3.2.2 Geochemical Record

For the original sampling of Agnini et al (2006), geochemical analyses are based on a lower resolution sample set (50 cm) from the top of the PETM to magnetochron C23r, with the exception of the PETM interval, which has been sampled at 5 cm spacing. From C23n to the top of the section (C20r) sample resolution is 20 cm which corresponds to about 20 kyr based on an average sedimentation rate of ~1 cm/kyr (Agnini et al., 2006).

From the new outcrop, stable isotope analyses were carried out on the 5 cm-spaced sample set spanning the middle part of Chron C24r to the middle part of Chron C22n, for a total of 409 samples. Carbon isotope analyses were performed at the IAMC-CNR laboratory (Capo Granitola, Italy) using an automated

continuous flow carbonate preparation GasBenchII device and a ThermoElectron Delta Plus XP mass spectrometer on powdered bulk rock samples after heating them at 400°C to remove organic components. Carbon isotope ratios of both records are calibrated to the Vienna Pee Dee Belemnite standard (VPDB) and converted to conventional delta notation ($\delta^{13}C$); precision is within ±0.06‰.

Wt.% $CaCO_3$ values have been measured on a total of 274 samples from the Possagno Core B. Sampling resolution was 5 cm with a few exceptions across slightly disturbed intervals where sampling resolution was 10 cm. Wt.% $CaCO_3$ content measurement was performed using a "Dietrich-Fruhling" calcimeter at the University of Urbino. Based on replicate analyses, precision is within 1.5%.

3.2.3 Spectral Analysis

Cyclostratigraphic analysis was performed in the depth domain using the wt.% $CaCO_3$ record obtained from 20 cm-spaced samples collected from the upper part of Chron C22r to the lower part of Chron C20r and on the 5 cm-spaced sample set over the C23n to the lower part of Chron C21r interval. A power spectrum analysis of the wt.% $CaCO_3$ has been conducted using a 2π- Multi Taper Method (MTM) with three tapers spectral analysis using the Astrochron Package (Meyers, 2014). This approach allows us for the identification of periodic components exceeding the 95% confidence level.

In order to assess the relationship between $\delta^{13}C$ and $CaCO_3$ records, a cross correlation of the $\delta^{13}C$ and wt.% $CaCO_3$ and a coherency analysis of the two signals have been performed using AnalySeries software (Paillard et al., 1996).

3.2.4 Paleomagnetic analysis

In order to detect the stratigraphic position of the C22r/C22n magnetochron boundary in the new high-resolution record, a new magnetic stratigraphic analysis was performed. A total of five equally spaced (50 cm), oriented samples have been collected in a restricted interval where the C22r/C22n boundary was expected to occur based on comparison with the litho–, bio– and magnetostratigraphy of Agnini et al. (2006).

From the Possagno Core B, a number of 36 paleomagnetic samples were collected at 50-cm average resolution. Samples were drilled perpendicularly to the vertical core axis.

Paleomagnetic samples were stepwise thermally demagnetized up to a maximum temperature of 575°C and measured with a 2G cryogenic magnetometer at the Alpine Laboratory of Paleomagnetism (ALP, Peveragno), following standard paleomagnetic procedures (Kirschvink, 1980). The primary magnetization was isolated using principal component analysis at temperatures between 350°C and 575°C, and magnetic polarity was interpreted after calculation of the virtual geomagnetic polarity latitude.

3.3 RESULTS

3.3.1 Geochemical records

For the original sampling of Agnini et al. (2006), average wt.% $CaCO_3$ values are ~70% up to 35 m above the PETM (Fig. 3.2). From this point upward a gradual decline is observed, which tracks the transition from the Scaglia Rossa Fm. to the more clayey Scaglia Cinerea Fm. as defined by Agnini et al. (2006). Calcium carbonate values from the newly available outcrop range from ~26% to ~97% with an average value of ~75% (Fig. 3.3). Most of the variability is observed across magnetochron C23n (Fig. 3.3), similar to what observed in other deep-water settings (Galeotti et al., 2017). The wt.% $CaCO_3$ record from the Possagno Core B ranges from ~37 to ~96%, with an average value of ~74% (Fig. 3.4).

The carbon isotope record from the low-resolution sample set (Agnini et al., 2006) shows large excursions, with higher frequency fluctuations observed across magnetochron C23n. A well-defined CIE of ~2‰ is recorded across the 40 cm-thick PETM interval (Fig. 3.2). From the PETM to the upper part of C24n the well-known gradual decline of carbon isotope average values (Zachos et al., 2008) is observed (see also Luciani et al., 2016). The low-resolution data from the original sampling of Agnini et al. (2006) does not allow identifying hyperthermal events (i.e. H1, H2, I1, I2 and K of Cramer et al., 2003) that are known to occur within the C24r-C24n interval.

The new carbon isotope record based on the higher resolution sample set, however, allows capturing all the major early Eocene CIEs (Fig. 3.3). The onset of ETM2 is observed at -7.20 m and the onset of ETM3 at -0.40 m below the base of the Aquamarina Bed, which falls in the middle part of the condensed Chron C23r based on the litho- and magnetostratigraphy of Agnini et al. (2006). Both sample sets show a very large variability across C23n, associated to the climax interval of the EECO (Figs. 3.2, 3.3). Following this interval of larger variability in both $CaCO_3$ and $\delta^{13}C$ records, a shift towards heavier average $\delta^{13}C$ values is observed in the upper half of Chron C23n. From here to the top of the section, the $\delta^{13}C$ record shows diminished variance around an average value of ~1‰. Yet, prominent CIEs, of up to 1‰, are recorded in C22r to lowermost C21r and in the lower third of C21n (Figs. 3.2, 3.3).

3.3.2 The Possagno composite stratigraphic record

The new outcrop sampled at high resolution across C24r-C22n is located ~200 m away from the original section sampled by Agnini et al. (2006), within the same quarry area. Considering the pelagic nature of the Scaglia Rossa limestones and its bathyal depositional setting, no lithostratigraphic changes are to be expected between the two successions. Indeed, the occurrence of lithological marker beds allowed us a first order correlation in the field. In particular, a straightforward lithostratigraphic correlation is permitted by the occurrence of Aquamarina marker bed, which occurs at the C24n/C23r magnetochron boundary. A

further mean of lithostratigraphic correlation is provided by the succession of prominent marly beds at specific depths relative to the Aquamarina Bed in both outcrops. The condensed Aquamarina Bed lies only 20 cm above the top of the prominent marly layer corresponding to ETM3. However, the latter occurs ~350 kyr prior to the top of C24n.1n in other successions (Francescone et al., 2018; Lauretano et al., 2016). Hence, the occurrence of the Aquamarina Bed at the boundary between C23r/C24n not only implies a stratigraphic gap within magnetochron C23r, as suggested by Agnini et al. (2006), but also decapitates the topmost ~200kyr of magnetochron C24n. For this reason, our cyclochronological analysis of the interval below the Aquamarina Bed, is limited to cycle counting between ETM2 and ETM3.

Similarly, the C23n/C22r magnetochron boundary is recognizable by mean of robust biostratigraphic datums being sandwiched by the base of *Coccolithus crassus* and the first common occurrence of reticulofenestrids (*Dictyococcites* and *Reticulofenestra*) (see Fig. 3.3). The latter event occurs ~45 cm above the C23n/C22r boundary according to Agnini et al. (2006). The top of C22r magnetochron has been identified directly by collecting new samples for paleomagnetic analysis in the newly sampled outcrop. All together these constraints allow a robust projection of the magnetostratigraphy of Agnini et al. (2006) to the new samples with a cm-scale error.

Paleomagnetic analysis of the new Possagno section, indicates a reversal between 9.80 m and 10.50 m (Fig. 3.3). In agreement with the original data set of Agnini et al. (2006), this magnetozone is interpreted as the C22r/C22n magnetochron boundary. This provides a direct comparison between the high-resolution sample set and the data originally sampled by Agnini et al (2006). In the Possagno Core B, preliminary biostratigraphic analysis allows excluding the presence of *Tribrachiatus orthostylus* and identifying the lowest and probably the lowest common occurrence of *Discoaster sublodoensis* at 6.30 and 1.10 meters below ground level (m) to bottom core, respectively (Fig. 3.4). On this basis, the two reversals identified between 1.07-1.63 mbgl and 7.43-7.87 mbgl are interpreted as the top and bottom of C22n, respectively (Fig. 3.4). Consequently, C22n has a thickness of ~6.2 ± 0.5 m, in line with the observation made on the outcrop by Agnini et al. (2006). In summary, therefore, the newly available high-resolution record, including the new outcrop and the Possagno Core B, spans mid C24r to lower C21r magnetochrons. From C21r to lower C20r only a low-resolution (20 cm) record is available.

3.4 CHEMOSTRATIGRAPHIC CORRELATION WITH ODP SITES 1258, 1263 AND THE UMBRIA-MARCHE BASIN

Carbon isotope records provide a robust tool for inter-site geochemical correlation, as CIEs and dynamics regulating changes in seawater $\delta^{13}C$ have a global extent (Francescone et al., 2018; Westerhold et al., 2018).

In order to compare the local carbon isotope record from Possagno with similar records from other sites, prominent CIEs are labeled following Cramer et al. (2003) up to the lowermost magnetochron C23r,

including H1 to L CIEs, and Lauretano et al. (2016) between the middle C23r and the lower C22n Chron, including M to W CIEs. For the rest of the studied interval (middle C22n to upper C21r), we followed the labeling of Sexton et al. (2011), revised by Westerhold et al. (2017). Comparison between the original data (Luciani et al., 2016) and the higher resolution record from the new sampling is very satisfactory in terms of long-term trends. However, the amplitude of some CIEs recorded in the low-resolution record of Luciani et al. (2016) is not reproduced in the new carbon isotope profile (Fig. 3.5). Particularly problematic is the interval encompassing magnetochron C23n. In fact, the $\delta^{13}C$ low-resolution profile shows a series of CIEs that have no counterparts in terms of amplitude in the high-resolution record at Possagno and other records worldwide (Galeotti et al., 2017; Kirtland Turner et al., 2014; Lauretano et al., 2016; Sexton et al., 2011; Westerhold et al., 2018). Hence, while the record obtained from the Agnini et al.'s sampling set (Luciani et al., 2016) reflects global long-term trends, some problem, possibly related to local diagenetic overprint, causing the amplitude of individual CIE events to differ from other records is evident. Moreover, T and U events (Lauretano et al., 2016) characterized by two prominent CIEs in the middle and in the upper part of Chron C22r, are weakly expressed when compared with the high resolution record. In this case, however, the low magnitude could be related to samples spacing, probably too low to correctly capture the associated $\delta^{13}C$ excursion. Importantly, from C22n upwards, the lower resolution Possagno $\delta^{13}C$ record is well comparable to other records worldwide. Accordingly, the two very distinctive triplets of CIEs, labeled C22nH3/H4/H5 and C21rH3/H4/H5, can be confidently correlated to other sites, in spite of the low resolution of the Possagno record.

The newly obtained 5 cm-spaced $\delta^{13}C$ record shows a very good match with ODP Site 1258 at Demerara Rise (Kirtland Turner et al., 2014; Sexton et al., 2011), ODP Site 1263 at Walvis Ridge (Lauretano et al., 2016), ODP Site 1209 at Shatsky Rise (Westerhold et al., 2018) and the U-M basin (Francescone et al., 2018). Evidently, the good alignment of all these records, including benthic foraminifers and bulk samples at different locations/oceans, results from factors controlling the global carbon cycle, which are reflected in all marine records.

Besides individual CIEs, the alignment of different records allows to evidence several features which characterize the long-term trend of the carbon isotope record worldwide. Notably, all carbon isotope profiles show that the interval encompassing the upper part of magnetochron C24r to the upper part of Chron C23n is characterized by the lowest carbon isotope values (Fig. 3.5). Within this ~2.8 Myr-long interval, a sequence of nine events, included between H1/ETM2 to N, occur. Another prominent feature of all record is the very large variance that characterizes the interval corresponding to magnetochron C23n.

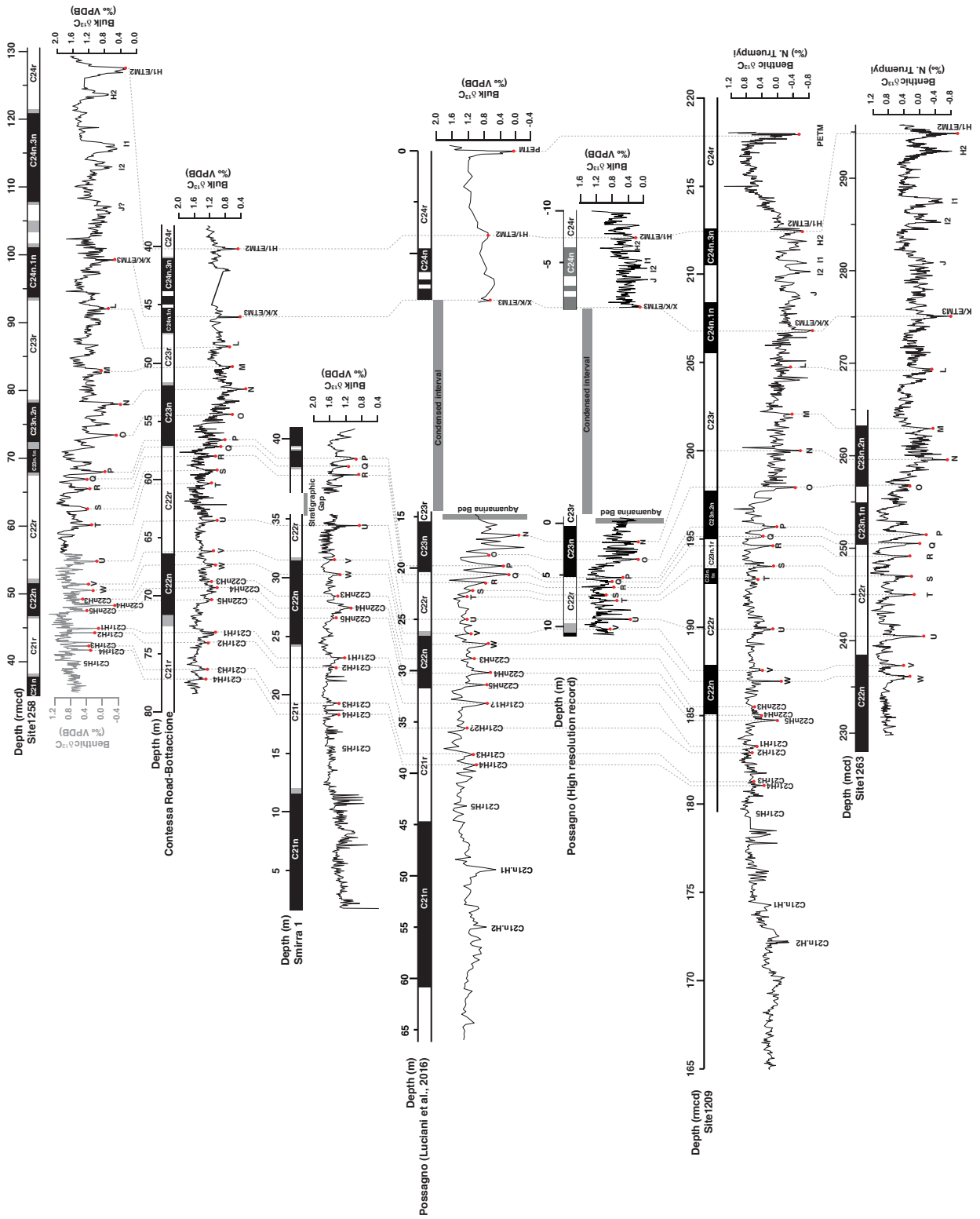

Figure 3.5: *Chemostratigraphic ($\delta^{13}C$) and magnetostratigraphic correlations among ODP Site 1258 (Kirtland Turner et al., 2014 [black line] and Sexton et al., 2011 [gray line]), Contessa Road–Bottaccione composite section and Smirra 1 core (Francescone et al., 2018; Galeotti et al., 2010, 2017), Possagno*

record derived from Agnini et al.'s sampling (Luciani et al., 2016) and Possagno high resolution record, ODP Site 1209 (Westerhold et al., 2018) and ODP Site 1263 (Lauretano et al., 2016).

Importantly, this might provide an observational basis to validate theoretical models predicting a threshold effect resulting from orbital forcing superimposed on gradually changing mean global boundary conditions for early Eocene hyperthermals, as proposed by Lunt et al. (2011) and DeConto et al. (2012). Galeotti et al. (2017) tentatively defined this 1 Myr-long interval as corresponding to the EECO. A major positive ~0.7‰ carbon isotope shift occurs globally in the upper half of Chron C23n, hence at the height of peak temperatures across the EECO. In correspondence of this carbon shift, marine $\delta^{18}O$ values do not display large or permanent variations (Zachos et al., 2008; Lauretano et al., 2018; Westerhold et al., 2018,), implying a minimal impact on CO_2 concentrations. From here upwards, all the $\delta^{13}C$ records show diminished variance. This shift occurs just before the O event in all records. With respect to this observation, ODP Site 1209 is an obvious exception because the shift occurs, in the tentative magnetostratigraphic interpretation of this site (Westerhold et al., 2018), at the topmost part of magnetochron C23r. This likely erroneous interpretation propagates over younger intervals. Indeed, R and S events fall in subchron C23n.1r and T event at the topmost part of C23n.1n, while in all other $\delta^{13}C$ records these events occur in the lower half of magnetochron C22r.

After the shift recorded in the upper part of C23n, average $\delta^{13}C$ values show a long interval of relative stability – between P and C22nH5 CIEs. Within this interval, a total of 11 CIEs occur. Possibly, a second short-lived (~50 kyr) positive shift (~0.15%) occurs at the end of magnetochron C22n, just after the C22nH5 event. This shift takes place in coincidence with the onset of the post-EECO long-term cooling trend at ~49.1 Ma. In spite of its low magnitude, therefore, it possibly represents an important event in the global carbon cycle, which is reflected in global marine temperature.

Carbon isotope mean values remain stable up to the lower part of magnetochron C21n where a shift towards lighter values occurs, in coincidence with the C21n.H1 event. This ~0.4 shift is recorded at both Pacific Site ODP Site 1209 and Possagno, likely capturing a global trend. After it, mean values remain lower for about 1 Myr coinciding with an extended warming reversal at ~47 Ma within the Eocene long-term cooling (Westerhold et al., 2018).

3.5 CYCLOCHRONOLOGY

Because of the large increase in sedimentation rate recorded between C22r and C22n magnetochrons (Agnini et al., 2006 - Fig. 3.3), the occurrence of a stratigraphic gap (or condensation) across the Aquamarina Bed, and because samples have been collected at different locations within the Carcoselle quarry, spectral analysis has been conducted separately on four discrete stratigraphic segments. The first two segments, corresponding to the upper C24r to the upper C24n magnetochrons and from Chron C23n to

magnetochron C22r, respectively, for which a high resolution (5 cm) sample set is available, have been analyzed from the newly sampled outcrop. The third segment spanning magnetochron C22n to the upper part of Chron C21n has been analyzed from the older (lower-resolution) sampling of Agnini et al. (2006). Spectral analysis conducted on the wt.% $CaCO_3$ record from the Possagno Core B complements the analysis of the third segment across C22n. Based on sedimentation rate values reported by Agnini et al. (2006), the available sampling resolution in the time domain is ~10kyr for the first two segments and the Possagno Core B. The 20cm-spaced samples from the fourth interval represents 20 kyr intervals.

Results of the MTM spectral analysis are presented separately for the different intervals in figure 3.6.

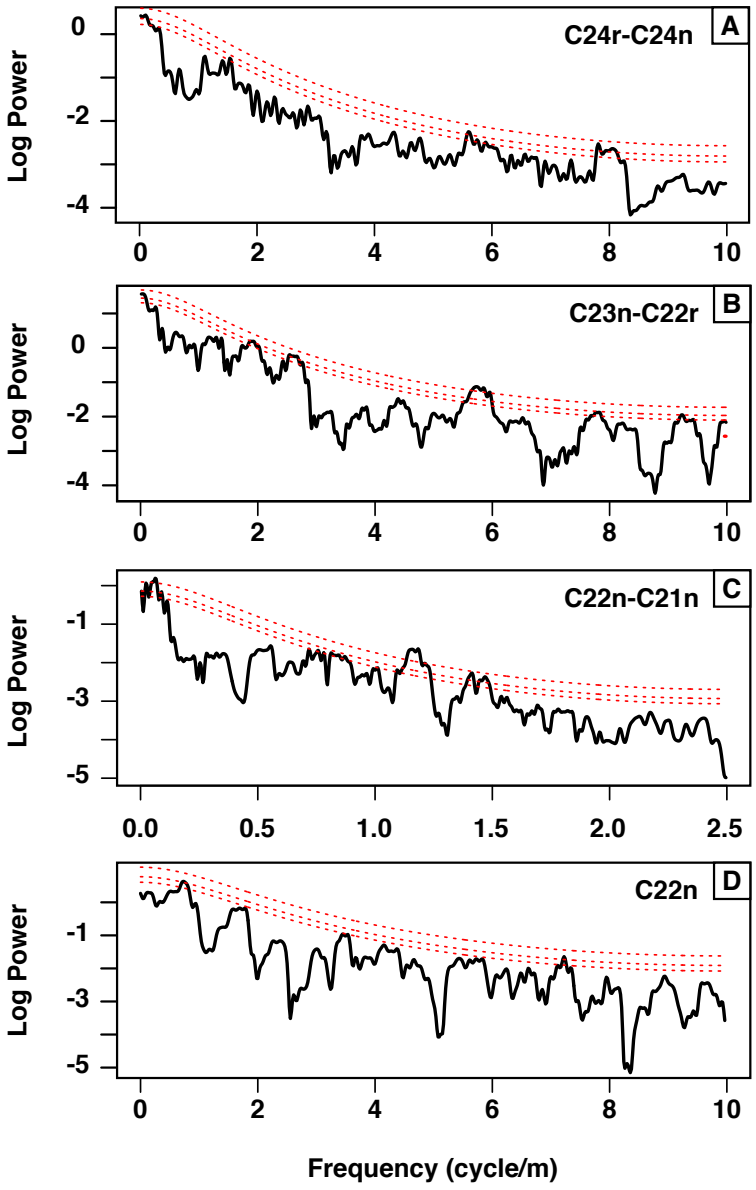

Figure 3.6: *Results of the MTM spectral analysis carried out on the wt.% $CaCO_3$ record from A) the C24r-C24n interval and B) C23n-C22r intervals from which a higher resolution sample set is available; C) C22n-*

C21n interval performed on the low resolution sample set of Agnini et al. (2006) and D) C22n from the Possagno Core B. The 90%, 95% and 99% confidence limits are reported as dashed lines.

3.5.1 C24r-C24n stratigraphic interval

The MTM analysis on the new high resolution sample set below Aquamarina Bed, allows identifying periodic components (> 95% confidence limit) centered at frequencies of ~1.6 cycle/m, ~5.7 cycle/m and ~8 cycle/m corresponding to wavelengths of ~60 cm, ~17.5 and ~12.5 cm, respectively (Fig. 3.6A). Based on the average sedimentation rate proposed by Agnini et al. (2006), these frequencies correspond to ~120 kyr, ~34 kyr and ~20 kyr. Assuming that the ~60 cm component represents the short eccentricity, we filtered it to establish a basic cyclochronology for the C24r-C24n interval (Fig. 3.7A). After Gaussian filtering of the wt.% $CaCO_3$ record centered at ~1.65 cycles/m with a bandwidth of ±15%, we count 12 short eccentricity cycles between ETM2 and ETM3 (Fig. 3.7A), similar to previous cyclochronological analyses for the same interval (Galeotti et al., 2010; 2017; Lauretano et al., 2016).

3.5.2 C23n-C22r stratigraphic interval

Spectral analysis allows identifying periodic components above the 95% confidence limit in the wt.% $CaCO_3$. These components are centered at frequencies of ~2 cycle/m ~2.5 cycle/m and ~5.8 cycle/m, corresponding to wavelengths of 50 cm, 40 cm and ~17 cm, respectively (Fig. 3.6B). Based on the average sedimentation rate proposed by Agnini et al. (2006), this implies periods of ~100 kyr, 80 kyr and ~34 kyr, respectively. Bandpass frequency filtering of the 40 cm and 50 cm periodic component related to short eccentricity allows establishing a basic cyclochronological framework for the C23n-C22r interval (Fig. 3.7B). After Gaussian filtering of the wt.% $CaCO_3$ record centered at 2.25 cycles/m with a bandwidth of ±15%, we count 10 short eccentricity cycles across C23n, which suggests a total duration of ~1000 kyr for this magnetochron. Cycle counting provides evidence for the occurrence of 10 short eccentricity cycles within C22r, for a total duration of ~1000 kyr. Unfortunately, a rather loose definition of the top of C22r does not allow a precise assessment of the cyclochronological duration of this magnetochron. However, we stress that using median point within the stratigraphic uncertainty of C23n base and C22r top, the two magnetochrons together contains 20 short eccentricity cycles, very similar to what observed at ODP Site 1258 (Westrehold et al., 2017) and at the Bottaccione section of Umbria-Marche basin (Galeotti et al., 2017).

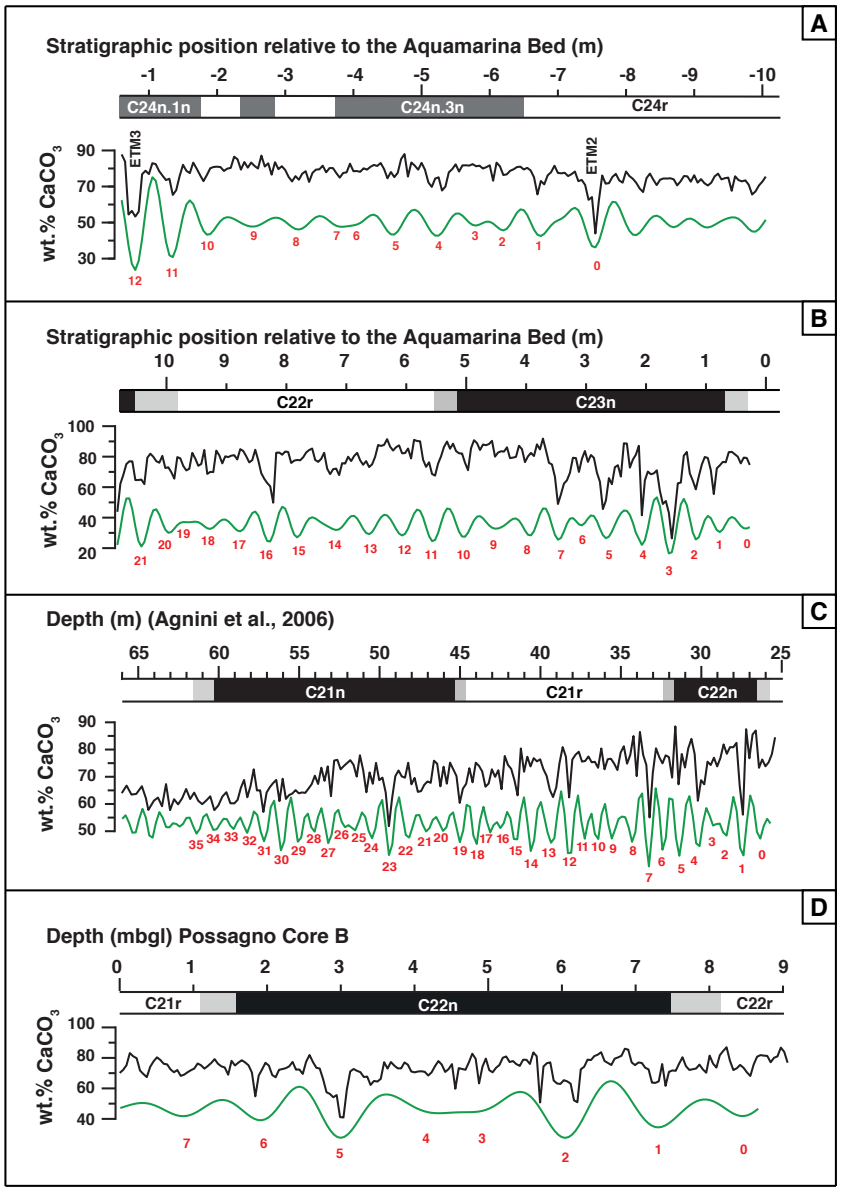

Figure 3.7: *Short eccentricity (green line) filters in the A) C24r-C24n and B) C23n-C22r stratigraphic intervals from which a higher resolution sample set is available; C) C22n-C21n stratigraphic interval from the low resolution sample set of Agnini et al. (2006) and D) C22n from the Possagno Core B.*

3.5.3 C22n-C21n stratigraphic interval

Based on an average sedimentation rate of ~1 cm/kyr, the sampling resolution of 20 cm of the sample set collected by Agnini et al. (2006) is too low to identify higher frequency orbital components, including obliquity. Yet, the MTM spectral analysis of the wt.% $CaCO_3$ record allows identifying a broad band of periodic components exceeding the 95% confidence limit centered at a frequency of 1 cycle/m (Fig. 3.6C), or a period wavelength of ~1 m corresponding to a period of ~100 kyr. Bandpass frequency filtering of the

1 m-period component allows establishing a basic cyclochronological framework for the surveyed interval (Fig. 3.7C). With the necessary caution imposed by the low sampling resolution, we obtain a number of cycles across C22n and C21r that closely matches the cyclostratigraphy of the same interval at ODP Site 1258, and the U-M basin (Francescone et al., 2018; Galeotti et al., 2017; Westerhold et al., 2017). In particular, we count 6 short eccentricity cycles in Chron C22n and 13 cycles in Chron C21r, for a total duration of 600 and 1300 kyr, respectively. We further extend our cyclochronology to magnetochron C21n, estimating 16 short eccentricity cycles. Also considering the uncertainties in the position of magnetochron boundaries, particularly large at the top of C21n, the latter has a cyclochronological duration of ~1.6 Myr.

3.5.4. C22n stratigraphic interval in the Possagno Core B

In line with the estimated duration of Chron C22n from the record of the sample set collected by Agnini et al. (2006 – Fig. 3.7C), the higher resolution $CaCO_3$ record from the Possagno Core B provides evidence for the occurrence of 6-6.5 short eccentricity cycles for the magnetochron C22n (Fig. 3.7D). Thus implies a cyclochronological duration of 600-650 kyr. However, our paleomagnetic analysis does not allow us to define C22r/C22n and C22n/C21r magnetochron boundaries with a precision better than ~50 cm.

3.6 DISCUSSION

Lithological cycles across hyperthermal events in Paleocene-Eocene bathyal records are controlled by carbonate dissolution (Lourens et al. 2005; Westerhold et al., 2007). Bathyal depositional settings sufficiently close to ancient continental margins, record both dissolution related to shoaling of the CCD and lysocline and/or carbonate dilution related to increased siliciclastic fluxes, which are concomitant phenomena across hyperthermal events. Carbonate dilution by enhanced runoff across hyperthermals is a feature of marginal depositional settings (Nicolo et al., 2007) typical of the shallower-water eastern Veneto depositional settings (e.g. Giusberti et al. 2007, 2016). Cross-correlation analysis of the $CaCO_3$ and $\delta^{13}C$ time series in the time domain within the C22n-C21n interval shows > 99% coherency of the two records for frequencies in the range of the short eccentricity component (Fig. 3.8). No relevant phase lag between the two records is observed, suggesting a common causal mechanism for negative carbon isotope excursions (CIEs) and $CaCO_3$ depletion, which likely results from the interplay of dissolution and dilution as expected in the depositional setting under investigation. Changes in sedimentation rate do not provide univocal evidence for dissolution or dilution cycles in the $CaCO_3$ record of Possagno, although dilution has been reported to be the prevalent mechanism for low wt.% $CaCO_3$ values across hyperthermals in eastern Veneto successions (Giusberti et al., 2007).

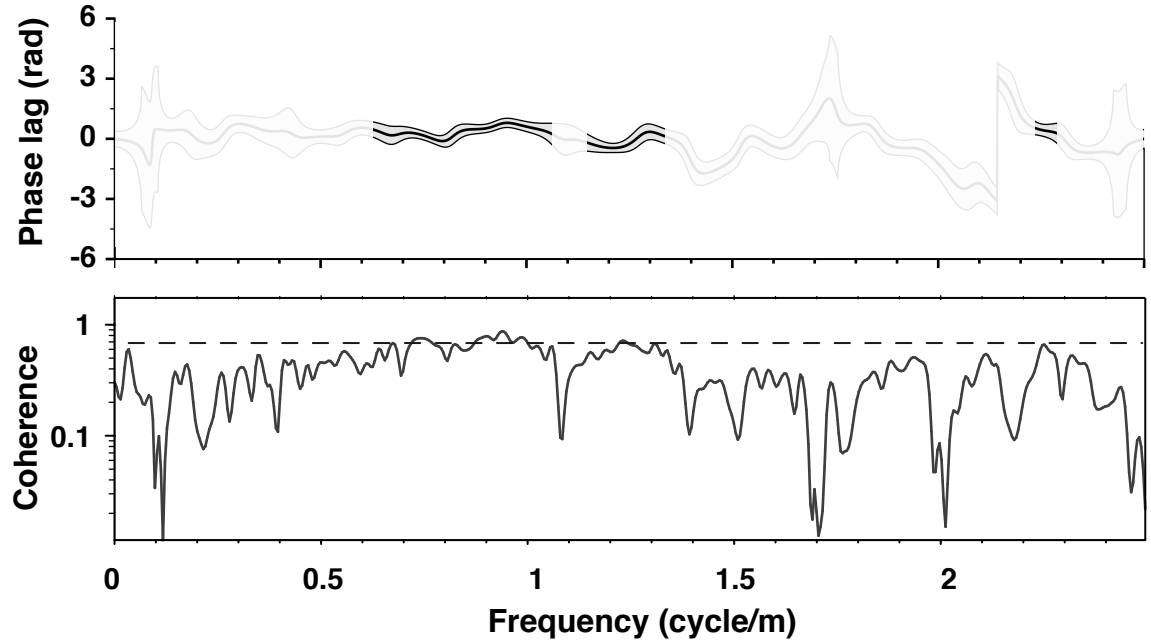

Figure 3.8: *Phase lag (upper panel) and coherency (lower panel) of the $\delta^{13}C$ and $CaCO_3$ record from the post-EECO interval at Possagno. Note how the two records show no lag for most of the frequency spectrum and high (>99% confidence limit) coherency across orbital frequencies corresponding to the short eccentricity, i.e. 1 cycle/m.*

3.6.1 Astrochronology

Orbital components derived from the wt.% $CaCO_3$ record have been used to tune the Possagno record to La2010b astronomical solution of Laskar et al. (2010), similar to Westerhold et al. (2017) and Francescone et al (2018). For this exercise we focus on the C23n-C22r and C22n-C21n intervals, as we have no direct magnetostratigraphic constraint for the C24n in the lowermost of the three segments analyzed and because C24n is clearly truncated at its top by the Aquamarina Bed. As a tie point for the tuning we use an absolute age estimate of 54.09 Ma for ETM2 (Westerhold et al. 2007, option 2). Based on the cyclochronological record of the Contessa Road-Bottaccione composite section (Galeotti et al. 2010, 2017), this age propagates to an absolute age of 51.84 Ma for the lower boundary of Chron C23n, in line with the Geological Time Scale (GTS) 2004 (Ogg and Smith, 2004) and GTS2012 (Ogg, 2012; Vandenberghe et al., 2012). The occurrence of a clear modulation in the short eccentricity filter across the C23n-C22r interval, however, indicates that the lower boundary of C23n seats on a 405 kyr minimum, as already observed in other deep-sea settings (Lauretano et al., 2016; Westerhold et al., 2017) and that a maximum of long eccentricity occurs at 1.8 m above the Aquamarina bed (Fig. 3.7). The duration of individual magnetochrons after tuning is reported in Table 3.1, together with previous estimates provided by different authors. The duration obtained from the cyclochronological analysis of the Possagno section closely matches the GPTS of Cande and Kent

(1995), and the most recent astrochronological estimates of Westerhold et al. (2017) and Francescone et al. (2018) (Tables 3.1, 3.2, Fig. 3.9). We conclude that the Possagno record provides a valuable cyclochronological and astrochronological estimate of the duration of the interval spanning C23n–C22r. However, some differences exist between the cyclochronology of magnetochrons C22n and C21r from Possagno and other age models, being ~100 kyr shorter and 100 kyr longer, respectively, than reported by Westerhold et al. (2017) and Francescone et al. (2018). The low-resolution of samples across C22n-C21r might explain this discrepancy.

		Standard GTS		Astronomically calibrated			Cycle Counting	Tuned
Chron	**CK95**	**GTS 2004**	**GTS 2012**	**Wetal17**	**CR-BTT**	**S1**	**Possagno**	
C21n	1642	1889	1625	1599			1600	1660
C21r	1131	1364	1217	1161		1110	1300	1230
C22n	677	828	778	700	770	800	600-650	670
C22r	1064	1303	1284	1082	1100		1000	1140
C23n	965	1171	1205	961	950		1000	1040

Table 3.1: *Estimated duration (kyr) of individual magnetochrons for the surveyed interval according to different authors: CK95 = Cande and Kent (1995); GTS2004 = Geological Time Scale 2004 (Ogg and Smith, 2004); GTS2012 = Geological Time Scale 2012 (Ogg, 2012; Vandenberghe et al., 2012); Wetal17 = Westerhold et al. (2017); CR-BTT = Contessa Road-Bottaccione composite section and S1 = Smirra 1 core (Francescone et al., 2018; Galeotti et al., 2017) and this work (Possagno).*

The cyclochronological duration and the inferred astrochronological ages of magnetochron boundaries and individual CIE events are reported in Tables 3.2 and 3.3, along with previous estimates by other authors. The largest differences with the most recent astrochronological estimates of Westerhold et al. (2017), Lauretano et al. (2016) and Francescone et al. (2018), are limited to one short eccentricity cycle across the C22nH1, or V, C21rH5 and C21n.H1 events.

All in all, the Possagno outcrops provide a good quality record of early-middle Eocene hyperthermal events and their cyclochronology. This will need to be refined by analyzing the available drillholes at a resolution sufficient to better solve cyclocstratigraphy at the short eccentricity level and beyond.

Event	Possagno	CR-BTT	S1	Lau3c	Wetal17	Wetal18
PETM		56.10			55.93	
ETM2		54.09		54.14	54.05	
ETM3		52.80		52.83	52.84	
L, C23rH1		52.44		52.41	52.46	
M, C23rH2		52.00		51.88	51.97	
N, C23n.2nH1	51.62	51.63		51.55	51.55	
O, C23n.2nH2	51.24	51.21		51.28	51.23	
P, C23n.1nH1	50.85	50.85		50.80	50.86	
Q, C22rH1	50.76	50.76		50.73	50.76	
R, C22rH2	50.61	50.62		50.63	50.67	
S, C22rH3	50.47	50.40		50.47	50.48	
T, C22rH4	50.36	50.29		50.32	50.37	
U, C22rH5	49.97	49.96	49.96	49.96	49.95	
V, C22nH1	49.78	49.67	49.67	49.70	49.68	
W, C22nH2	49.58	49.53	49.52	49.6	49.58	
C22nH3	49.29	49.29	49.29		49.38	
C22nH4	49.13	49.19	49.19		49.25	
C22nH5	49.01	49.08	49.07		49.14	
C21rH1	48.84	48.76	48.77		48.85	
C21rH2	48.63	48.66	48.69		48.76	
C21rH3	48.37	48.41	48.40		48.45	
C21rH4	48.29	48.32	48.31		48.36	
C21rH5	47.95		48.08		48.07	
C21n.H1	47.36					47.17
C21n.H2	46.74					46.74

Table 3.2: *Astrochronological age of hyperthermal events according to this study (Possagno), the Contessa Road-Bottaccione composite section (CR-BTT) and the Smirra 1 core (S1 – Francescone et al., 2018; Galeotti et al., 2010, 2017), the three-cycle option taken from Lauretano et al. (2016 - Lau3c), Westerhold et al. (2017 – Wetal17) and Westerhold et al. (2018 – Wetal18).*

Chron	CK95	GPTS2004	GPTS2012	Wetal17	CR-BTT	S1	Possagno
C20r $_{(base)}$	46.264	45.346	45.724	46.235			46.1±50
C21n $_{(base)}$	47.906	47.235	47.349	47.834		47.76	47.75±50
C21r $_{(base)}$	49.037	48.599	48.566	48.994	48.89	48.87	49.0±50
C22n $_{(base)}$	49.714	49.427	49.344	49.695	49.66	49.67	49.65±50
C22r $_{(base)}$	50.788	50.73	50.628	50.777	50.77		50.80±50
C23n $_{(base)}$	51.743	51.901	51.833	51.737	51.72		51.84±50

Table 3.3: *Magnetochron boundary ages according to CK95 = Cande and Kent (1995); GTS2004 = Geological Time Scale 2004 (Ogg and Smith, 2004); GTS2012 = Geological Time Scale 2012 (Ogg, 2012; Vandenberghe et al., 2012); Wetal17 = Westerhold et al. (2017); Contessa Road-Bottaccione (CR-BTT)*

composite section and the Smirra 1 core (S1 - Francescone et al., 2018; Galeotti et al., 2017) and this work (Possagno).

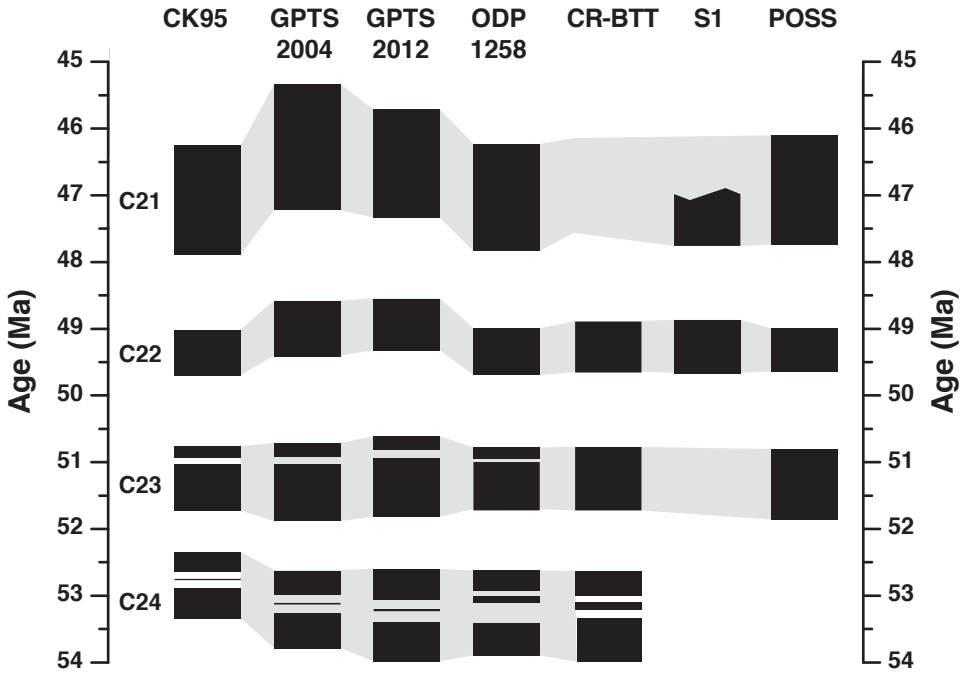

Figure 3.9: *Comparison of magnetochron boundary ages and durations for Chrons C24n to C21n based on estimates from Cande and Kent (1995; CK95), Geological Time Scale (GTS) 2004 (Ogg and Smith, 2004) and GTS2012 (Ogg, 2012; Vandenberghe et al., 2012), ODP Site 1258 (Westerhold et al., 2017), Contessa Road-Bottaccione composite section (CR-BTT) and the Smirra 1 core (S1 – Francescone et al., 2018; Galeotti et al., 2010, 2017) and this paper (POSS).*

3.7 CONCLUSIONS

The analysis of the carbon isotope record of the Possagno section reveals a succession of CIEs, which confirms previous observation of astronomically-controlled aberrations of the carbon cycle. Similar to what observed elsewhere, CIEs are associated with $CaCO_3$ depleted intervals. Possibly, $CaCO_3$ decreases at Possagno results from concomitant dissolution to enhanced clay fluxes confirming that dilution plays a role in determining lithological cycles across hyperthermals in the relatively marginal depositional setting of the eastern Veneto area. The detection of astronomical forcing on wt.% $CaCO_3$ allows to develop a floating cyclochronology for the stratigraphic interval spanning magnetochron C23n-C21n, confirm previous cyclochronological estimates across it and provide a floating cyclochronology for C21n. The alignment of stable carbon isotope records available from different basins and oceans allows identifying global features in terms of global occurrence of individual CIEs and longer-term trends.

Chapter IV

DOES THE COMPARISON OF CARBON RELEASE AND INCREASE IN BOTTOM WATER TEMPERATURE ACROSS EARLY EOCENE HYPERTHERMALS PROVIDE A CASE FOR GREENHOUSE STATE CLIMATE SENSITIVITY?

Simone Galeotti, Federica Francescone, Luca Lanci

To be submitted to Geology

ABSTRACT: Hyperthermals are a series of episodes of global warming caused by the rapid (10^{3-4} yr) injection of massive amounts of isotopically light carbon into the exogenic pool that occurred during the late Paleocene-early Eocene. These carbon cycle alterations are reflected in negative shifts of global $\delta^{13}C$ values, whose magnitude can be used to constrain the amount of carbon released provided that isotopic composition of the carbon source(s) is known and a high resolution age model is available. The associated negative shift in oxygen isotope values can be taken to provide – in the absence of ice – a confident measure of the consequent increase in temperature. Linear regression of stable carbon and oxygen isotope shifts, therefore, can be used to measure the global warming against the total amount of carbon release, which, in turn, should provide insights on the Climate Sensitivity during the Eocene. Changing background conditions for individual episodes (i.e. through time) needs, however, to be considered. Here we review the observed relationships between carbon and oxygen isotope values across early Eocene hyperthermals and discuss the practicability of this approach in determining the nature of the carbon source.

4.1 INTRODUCTION

The late Paleocene-early Eocene is punctuated by a series of episodes of sudden and extreme warming, known as hyperthermals. The first and most prominent of these events, the Paleocene Eocene Thermal Maximum (PETM) or Eocene Thermal Maximum 1 (ETM1), is characterized by negative global shifts in $\delta^{13}C$ and $\delta^{18}O$, and dissolution of carbonates in the deep ocean occurring ~56 million years ago (Ma). Together with independent temperature proxies (e.g. Sluijs et al., 2006), isotopic and sedimentary records provide evidence for a massive input of carbon into the coupled ocean-atmosphere system, ocean acidification (Zachos et al., 2005) and an increase in global temperature of about 5-6°C within a few thousand years (Kennett and Stott, 1991; Zachos et al., 2001). The acquisition of high-resolution stable isotope records from various oceanic sites and land-based sections have provided compelling evidence for the existence of other hyperthermal events of smaller magnitude compared to ETM1, including ETM2 (~54

Ma) and ETM3 (~52.8 Ma) and other minor events spread over the time interval between ~56 and ~47 Ma. Evidence suggests that these transient events were driven by the input of vast amounts of ^{13}C-depleted carbon into the coupled ocean-atmosphere system. Carbon release likely resulted from the destabilization of light-carbon reservoirs by crossing a thermodynamic threshold (Lunt et al., 2011) due to the interplay of the long-term warming and orbital forcing (DeConto et al., 2012; Dickens et al., 1997; Frieling et al., 2016; Kennett and Stott, 1991; Littler et al., 2014; Nicolo et al., 2007; Sluijs et al., 2007; Zachos et al., 2008). Provided that the amount of carbon released and consequent global temperature increases can be derived from geological archives, hyperthermal events provide a case to test Climate Sensitivity (CS) in the past. In particular, because future global warming from anthropogenic greenhouse gas emissions will depend on climate feedbacks, which are part of a complex response by the climate system, hyperthermals could provide insights on the climate system response to greenhouse gas forcing under warmer - than present day - conditions. Paired oxygen and carbon isotope shifts offer a mean to test the temperature response against the estimated amount of carbon release across individual hyperthermal events. Being representative of bottom-water temperatures, stable isotope records derived from benthic foraminifera are fundamental to assess the degree of warming and carbon dynamics (Lauretano et al., 2015; Westerhold et al., 2018; Lauretano et al., 2018). In particular, the slope of the regression lines of paired $\delta^{13}C/\delta^{18}O$ shifts during each event is an expression of the relationship between changes in the carbon cycle and consequent deep-sea warming. On the other hand, background conditions for each hyperthermal needs to be carefully evaluated when comparing the response across different events. Here we present the results of such a comparison based on available data from oceanic successions and discuss them in the light of evolving background conditions through the Eocene.

4.2 COVARIANCE OF $\delta^{13}C$ AND $\delta^{18}O$ ACROSS ETMs

Analysis of the covariance between benthic Carbon and Oxygen isotope values at the onset of ETMs have been presented by several authors from different oceanic sites including ETM1 and ETM2 at ODP Site 1263 (Stap et al., 2010), ETM2 and ETM3 at ODP Site 1262, Site 1263 and Site 1265 (Lauretano et al., 2015) and ETM1, ETM2 and ETM3 at ODP Site 1209 (Westerhold et al., 2018). The paleogeographic location of these oceanic Sites at the Paleocene/Eocene boundary time is reported in Fig. 4.1. Covariance across ETM1 at ODP Site 690 has been determined by Stap et al. (2010). Regression slopes have also been determined for other hyperthermals, i.e. events of negative $\delta^{13}C$ shift and statistically significant concomitant temperature increase by the same authors (Lauretano et al., 2015; Westerhold et al., 2018). No comparison of global covariance between $\delta^{13}C$ and $\delta^{18}O$ has been so far attempted for different hyperthermals, which does not ensure that the regression slope results from local environmental conditions, e.g. bottom water masses. Importantly, the acquisition of high resolution records from different oceanic

sites and land-based successions and of a robust cyclochronology of the late Paleocene-middle Eocene hyperthermal events (Westerhold et al., 2017, 2018; Galeotti et al., 2010, 2017; Francescone et al., 2018) allows to virtually correlate individual episodes on a global scale provided that a sound bio-magnetostratigraphy is available. Most high-resolution stable isotope records have been obtained from Atlantic Ocean sites, which would not allow inter-ocean comparison. However, the recent acquisition of a high-resolution record from the early Eocene of ODP Site 1209 allows to assess the temperature response – tracked by benthic foraminiferal $\delta^{18}O$ values – to carbon input of different magnitude – tracked by $\delta^{13}C$ – also for the Pacific Ocean. The consistent covariance between carbon and oxygen during ETM1, ETM2, and ETM3 has been taken to provide evidence that all these major hyperthermal events share similar characteristics (Stap et al., 2010; Lauretano et al., 2015, 2018; Westerhold et al., 2018). Comparable slopes of the $\delta^{13}C$ vs. $\delta^{18}O$ regression lines, in fact, are suggestive of similar mechanisms considering that the degree of change in the exogenic carbon pool and concurrent warming during all the events show similar ratios.

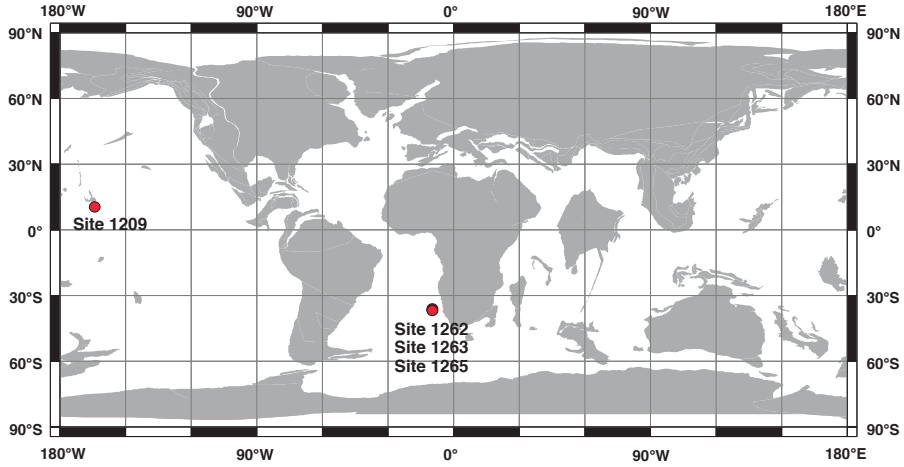

Figure 4.1: *Paleoceanographic reconstruction for the early Eocene (56 Ma) showing the position of ODP Sites 1262, 1263, 1265 and ODP Site 1209. Paleogeographic map is from the Ocean Drilling Stratigraphic Network Plate Tectonic Reconstruction Service: (http://www.odsn.de/odsn/services/paleomap/paleomap.html).*

4.3 THE PACIFIC AND ATLANTIC RECORDS

Detailed high-resolution investigations on South Atlantic (Leg 208) and Pacific (ODP Site 1209) benthic foraminiferal stable isotope data suggest that a coherent relation between $\delta^{13}C$ and $\delta^{18}O$ exists for ETM1, ETM2 and ETM3 (Stap et al., 2010; Lauretano et al., 2015; Westerhold et al., 2018). Although with different magnitude, decreases in $\delta^{13}C$ are associated to consistent decreases in $\delta^{18}O$ during these events and with similar slope. According to the above mentioned authors, a similar result points to a consistent global picture whereby the carbon input to the exogenic carbon pool caused proportional warming (Pagani

et al., 2006). Table 4.1 summarizes the different slopes observed for ETM1, ETM2 and ETM3 (Figs. 4.2, 4.3 and 4.4) at the Pacific Ocean ODP Site 1209 and South Atlantic Site 1263 and the amount of temperature increase in °C corresponding to each 1‰ variation in $\delta^{13}C$ values.

	ODP Site 1209		ODP Site 1263	
	$\Delta\delta^{18}O/\Delta\delta^{13}C$	T increase per 1‰ $\Delta\delta^{13}C$ (°C)	$\Delta\delta^{18}O/\Delta\delta^{13}C$	T increase per 1‰ $\Delta\delta^{13}C$ (°C)
ETM1	0.65	2.6	0.57	2.28
ETM2	0.7	2.8	0.55*	2.2
ETM3	0.48	1.92	0.55	2.2

Table 4.1: *$\Delta\delta^{18}O/\Delta\delta^{13}C$ ratio across ETMs at ODP Sites 1209 and 1263. Data are from Stap et al. (2010), Lauretano et al. (2015) and Westerhold et al. (2018). See also text. *ETM2 value is from Sites 1262 and Site 1265 where it shows the same slope of 0.55.*

All results are comprised between ~0.5 and 0.7. Resulting bottom-water temperature increase is in the range of 2–2.8°C per each permil variation of $\delta^{13}C$. The South Atlantic Leg 208 sites, in particular, show remarkable coherent slopes for the three major hyperthermal events. While this finding has been appreciated as an evidence for a common origin of the carbon source triggering the warming events (Stap et al., 2010; Lauretano et al., 2018; Westerhold et al., 2018), we emphasise that several factors introduce a non-linearity in the expected temperature response to carbon input across them, some of which suggesting that $\delta^{13}C/\delta^{18}O$ slopes should rather be different for different events instead of the same: i. the radiative forcing per doubling of CO_2 is a function of background conditions; ii. solubility of CO_2 in the ocean is a function of sea surface temperature; iii. climate sensitivity may be a function of mean global annual temperature (e.g. Shaffer et al., 2016). Because of the well-known gradual warming during the early Eocene, background conditions at the onset of each of the ETMs were different. Benthic stable isotope records provide evidence that bottom water temperature was ~3°C higher at the onset of ETM3 compared to ETM1. This aspect imposes caution in evaluating the coherency in the $\delta^{13}C/\delta^{18}O$ slopes as an indication that the carbon source was similar for all ETMs. A further complication could be the rate of emission, which seems to have been largely different for different ETMs (Stap et al., 2010). Taking into account all these aspects requires a modelling effort that is beyond the goal of this paper. Here we take a very approach by considering that the whole carbon input for individual episodes translates to a peak of CO_2. Ultimately this approach does not consider changing boundary conditions (i.e. ocean temperature, thus CO_2 solubility) and, possibly more important the rate of emission (i.e. total carbon emission/time). However, this approach is the same to that taken by calculating the slopes of linear regression between $\Delta\delta^{13}C$ and $\Delta\delta^{18}O$ and, therefore, provide a means to test previous findings.

Two cases, i.e. carbon input with -60‰ $\delta^{13}C$ values assuming that CO_2 derives entirely from the destabilization of gas hydrates (e.g. Dickens et al., 1995) and carbon input with -26.6‰ $\delta^{13}C$ assuming that CO_2 derives entirely from soils or peat (e.g. DeConto et al., 2012), have been considered (see Table 4.2).

	Gt of carbon release			CO_2 equivalent (ppm)			CO_2 doubling		
$\delta^{13}C$	ETM1	ETM2	ETM3	ETM1	ETM2	ETM3	ETM1	ETM2	ETM3
-60‰	1800	1600	520	720	640	208	1.9	1.5	1.2
-26.6‰	6500	3200	1250	2600	1280	500	4.25	2.1	1.4

Table 4.2: *Summary of total carbon releases for ETM1, ETM2 and ETM3 based on different isotopic composition of the reservoirs, the equivalent peak of CO_2 (ppm) considering that all the carbon contributes to the peak in a non-dynamic system and contributes of these amount measured as CO_2 doubling based on pre-events CO_2 levels of ~800ppm for ETM1 and ~1200 ppm for ETM2 and ETM3.*

We then plot the expected change in terms of mean global temperature using a CS of 5K per doubling of CO_2 following Shaffer et al.(2016). Because we use the same CS to compare ETM2 and ETM3 (similar to the Early Eocene Climatic Optimum) against ETM1, the ΔT between these two intervals provides the necessary information to calculate ΔpCO_2 between them, independently of absolute values of the latter. Considering a pCO_2 of ~800 ppm for the onset of the PETM and a ΔT of ~3°C between the latest Paleocene and the Early Eocene Climatic Optimum, which is similar to background conditions for ETM2 and ETM3, pCO_2 values at the onset of the two latter hyperthermals can be estimate to be ~1200.

Because of gradually changing background condition at the onset of ETMs through the Eocene (i.e. warming) and the decrease in time of the carbon input, resulting slopes are largely different, which should be captured by $\Delta\delta^{18}O/\Delta\delta^{13}C$ regression lines. As it can be seen in Figure 4.5, similar slope can be maintained through time and for different background conditions/ETMs only by changing the isotopic composition of the carbon input. In particular, a heavier carbon source is needed to justify the slopes observed for ETM2 and ETM3 which should be steeper than that of ETM1, being the temperature effect of a specific amount of carbon larger for the latter.

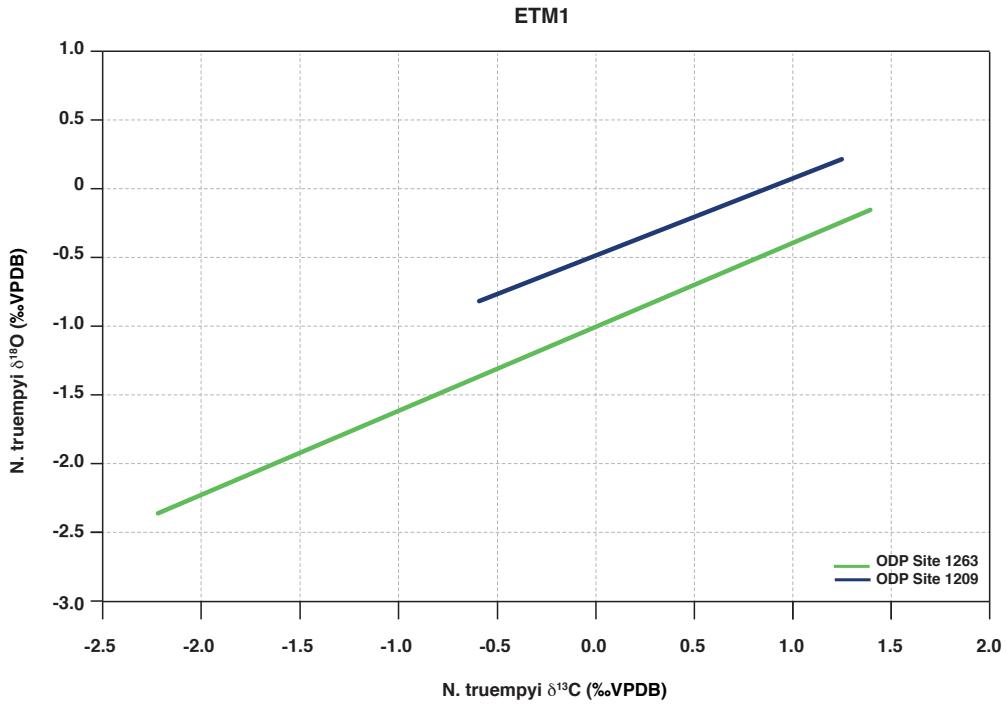

Figure 4.2: *Regression line between $\delta^{13}C$ and $\delta^{18}O$ during the onset of ETM1 (or PETM) at ODP Site 1263 and ODP Site 1209.*

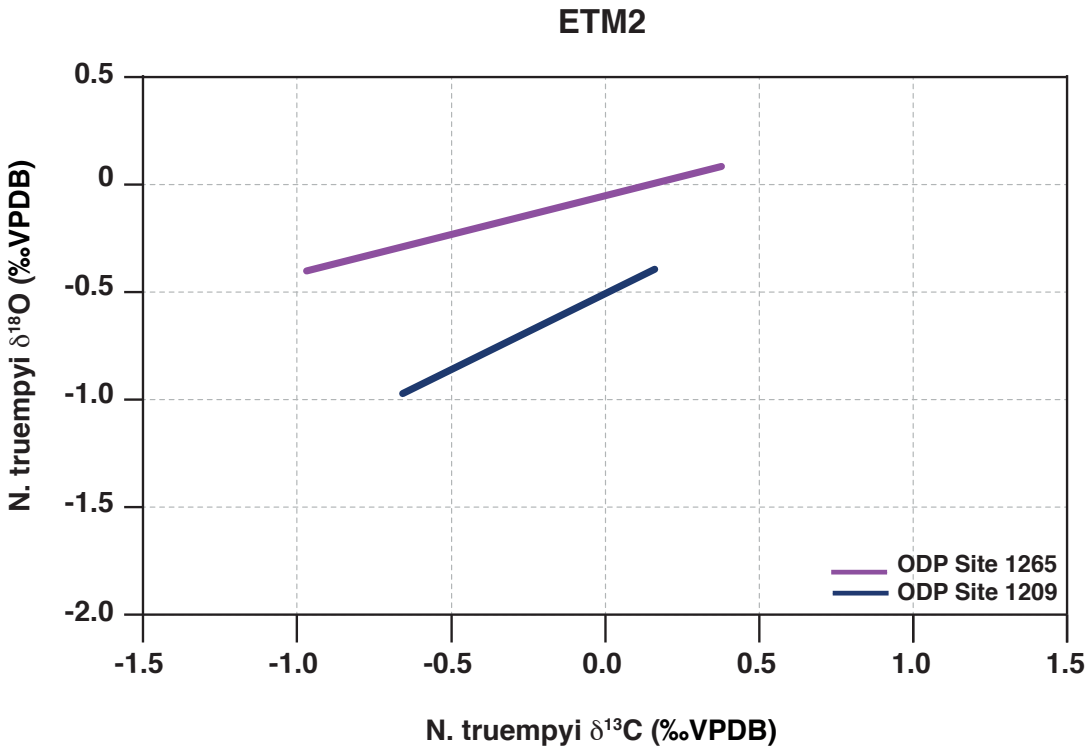

Figure 4.3: *Regression line between $\delta^{13}C$ and $\delta^{18}O$ during the onset of ETM2 at ODP Site 1265 and ODP Site 1209.*

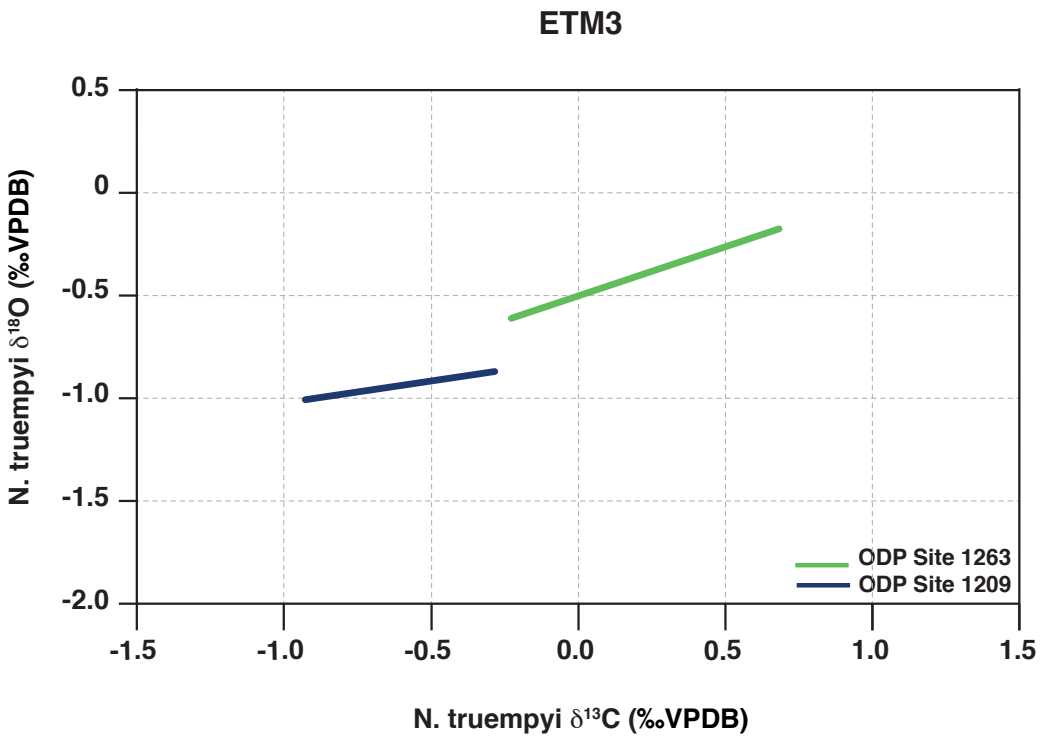

Figure 4.4: *Regression line between $\delta^{13}C$ and $\delta^{18}O$ during the onset of ETM3 at ODP Site 1263 and ODP Site 1209.*

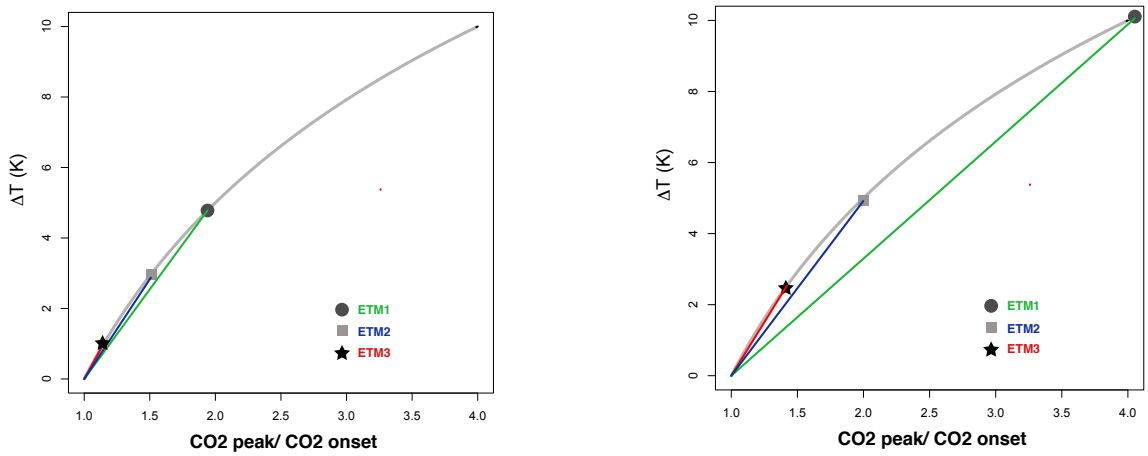

Figure 4.5: *Expected regression of CO_2 excess (in doubling of pre-ETM CO_2 atmospheric concentrations) vs ΔT (K) for ETM1, ETM2 and ETM3 based on the hypothesis that the total carbon released derives from a source with $\delta^{13}C$=-60‰ (right panel) or a source with $\delta^{13}C$ =-26.6‰ (left panel).*

4.4 CONCLUSIONS

Comparison of $\Delta\delta^{18}O$ and $\Delta\delta^{13}C$ across early Eocene hyperthermals show similar regression slopes in benthic foraminiferal records from both the Atlantic and Pacific Oceans. This result has been taken to indicate that all major ETMs (ETM1, ETM2 and ETM3) were caused by carbon release from the same source. However, when considered in the light of evolving mean background conditions though the early Eocene – as suggested by geochemical proxies – this result should rather point to a different isotopic composition of carbon for the considered events. This implies the existence of more than one reservoir. We suggest that gradual depletion in the mass of the isotopically lighter reservoir explain the coherence of regression slopes observed across all ETMs. This hypothesis would also account for the decreasing amplitude of the carbon shift associated with individual hyperthermals through time.

REFERENCES

Agnini, C., Fornaciari, E., Raffi, I., Catanzariti, R., Pälike, H., Backman, J., Rio, D., 2014, Biozonation and biochronology of Paleogene calcareous nannofossils from low and middle latitudes: Newsletters on Stratigraphy 47, 131-181. http://dx.doi.org/10.1127/0078-0421/2014/0042.

Agnini, C., Macrì, P., Backman, J., Brinkhuis, H., Fornaciari, E., Giusberti, L., Luciani, V., Rio, D., Sluijs, A., Speranza, F., 2009. An early Eocene carbon cycle perturbation at ~52.5 Ma in the Southern Alps: chronology and biotic response. Paleoceanography 24, 2209. https://doi.org/10.1029/2008PA001649.

Agnini, C., Muttoni, G., Kent, D.V., Rio, D., 2006. Eocene biostratigraphy and magnetic stratigraphy from Possagno, Italy: The calcareous nannofossil response to climate variability. Earth and Planetary Science Letters 241, 815–830. https://doi.org/10.1016/j.epsl.2005.11.005.

Arculus, R.J., Ishizuka, O., Bogus, K.A., Gurnis, M., Hickey-Vargas, R., Aljahdali, M.H., Bandini-Maeder, A.N., Barth, A.P., Brandl, P.A., Drab, L., et al., 2015, A record of spontaneous subduction initiation in the Izu-Bonin-Mariana arc: Nature Geoscience, v. 8, p. 728–733, doi: 10.1038/ngeo2515.

Arthur, M.A., and Fischer, A.G., 1977, Upper Cretaceous-Paleocene magnetic stratigraphy at Gubbio, Italy I. Lithostratigraphy and sedimentology: Geological Society of America Bulletin, v. 88, p. 367–371, doi: 10.1130/0016-7606(1977)88<367:UCMSAG>2.0.CO;2.

Billups, K., H. Pälike, J. E. T. Channell, J. Zachos, and N. J. Shackleton (2004), Astronomic calibration of the late Oligocene through early Miocene geomagnetic polarity time scale, Earth and Planetary Science Letters, 224, 33-44.

Bouligand, C., Dyment, J., Gallet, Y., and Hulot, G., 2006, Geomagnetic field variations between Chrons 33r and 19r (83–41 Ma) from sea-surface magnetic anomaly profiles: Earth and Planetary Science Letters, v. 250, p. 541–560, doi: 10.1016/j.epsl.2006.06.051.

Bowles, J., Tauxe, L., Gee, J., McMillan, D., and Cande, S., 2003, Source of tiny wiggles in Chron C5: A comparison of sedimentary relative intensity and marine magnetic anomalies: Geochemistry, Geophysics, Geosystems, v. 4, p. 1049, doi:10.1029/2002GC000489.

Cande, S. C., and Kent, D. V., 1992, A new geomagnetic polarity time scale for the Late Cretaceous and Cenozoic: Journal of Geophysical Research: Solid Earth, v. 97(B10), p. 13917-13951, doi: 10.1029/92JB01202.

Cande, S.C., and Kent, D.V., 1995, Revised calibration of the geomagnetic polarity timescale for the Late Cretaceous and Cenozoic: Journal of Geophysical Research: Solid Earth, v. 100, p. 6093–6095, doi: 10.1029/94JB03098.

Cande, S.C., and Patriat, P., 2015, The anticorrelated velocities of Africa and India in the Late Cretaceous and early Cenozoic: Geophysical Journal International, v. 200, p. 227–243, doi: 10.1093/gji/ggu392.

Charles, A. J., Condon, D. J., Harding, I. C., Pälike, H., Mar- shall, J. E., Cui, Y. et al. 2011. Constraints on the numerical age of the Paleocene–Eocene boundary. Geochemistry, Geophysics, Geosystems 12 (6), Q0AA17, doi: 10.1029/2010GC003426.

Coccioni, R., Bancalà, G., Catanzariti, R., Fornaciari, E., Frontalini, F., Giusberti, L., Sprovieri, M., 2012. An integrated stratigraphic record of the Palaeocene–lower Eocene at Gubbio (Italy): new insights into the early Palaeogene hyperthermals and carbon isotope excursions. Terra Nova 24, 380–386.

Cramer, B.S., Wright, J.D., Kent, D.V., and Aubry, M.P., 2003, Orbital climate forcing of $\delta^{13}C$ excursions in the late Paleocene–early Eocene (chrons C24n– C25n): Paleoceanography, v. 18, 1097, https://doi.org/10.1029/2003PA000909.

DeConto, R.M., Galeotti, S., Pagani, M., Tracy, D., Schaefer, K., Zhang, T., and Beerling, D.J., 2012. Past extreme warming events linked to massive carbon release from thawing permafrost: Nature, v. 484, p. 87–91, https://doi.org/10.1038/nature10929.

Dickens, G. R., Castillo, M.M., Walker, J.C., 1997. A blast of gas in the latest Paleocene: Simulating first-order effects of massive dissociation of oceanic methane hydrate. Geology, v. 25, p. 259-262, doi: 10.1130/0091-7613(1997)025<0259:ABOGIT>2.3.CO;2.

Dickens, G.R., O'Neil, J.R., Rea, D.K., Owen, R.M., 1995. Dissociation of oceanic methane hydrate as a cause of the carbon isotope excursion at the end of the Paleocene. Paleoceanography and Paleoclimatology, v. 10, p. 965-971, https://doi.org/10.1029/95PA02087.

Dinarès-Turell, J., Westerhold, T., Pujalte, V., Röhl, U., Kroon, D., 2014. Astronomical calibration of the Danian stage (Early Paleocene) revisited: Settling chronologies of sedimentary records across the Atlantic and Pacific Oceans. Earth and Planetary Science Letters 405, 119– 131.

Dunkley-Jones, T., Lunt, D.J., Schmidt, D.N., Ridgwell, A., Sluijs, A., Valdes, P.J., and Maslin, M., 2013, Climate model and proxy data constraints on ocean warming across the Paleocene-Eocene Thermal Maximum: Earth-Science Reviews, v. 125, p. 123–145, doi: 10.1016/j.earscirev.2013.07.004.

Francescone, F., Lauretano, V., Bouligand, C., Moretti, M., Sabatino, N., Schrader, C., Catanzariti, R., Hilgen, F., Lanci, L., Turtù, A., Sprovieri, M., Lourens, L., Galeotti, S., 2018. A 9 million-year-long astrochronological record of the early–middle Eocene corroborated by seafloor spreading rates. GSA Bulletin. https://doi.org/10.1130/B32050.1.

Frieling, J., Svensen, H.H., Planke, S., Cramwinckel, M.J., Selnes, H., Sluijs, A., 2016. Thermogenic methane release as a cause for the long duration of the PETM. Proceedings of the National Academy of Sciences, v. 113, p. 12059-12064, https://doi.org/10.1073/pnas.1603348113.

from sea-floor spreading rates: Nature, v. 364, p. 788–790, doi: 10.1038/364788a0.

Galeotti, S., Angori, E., Coccioni, R., Ferrari, G., Galbrun, B., Monechi, S., Premoli Silva, I., Speijer, R., and Turi, B., 2000, Integrated stratigraphy across the Paleocene/Eocene boundary in the Contessa

Road section, Gubbio (central Italy): Bulletin de la Societe Geologique de France, v. 171, p. 355–365, doi: 10.2113/171.3.355.

Galeotti, S., Kaminski, M.A., Speijer, R., Coccioni, R., 2005. High resolution Deep Water Agglutinated Foraminiferal record across the Paleocene/Eocene transition in the Contessa Road Section (central Italy). In: Bubik, M., Kaminski, M. A. (Eds.), Proceedings of the 6th Inter- national Workshop on Agglutinated Foraminifera: Grzybowski Foundation Special Publication 8, 83–103.

Galeotti, S., Krishnan, S., Pagani, M., Lanci, L., Gaudio, A., Zachos, J.C., Monechi, S., Morelli, G., and Lourens, L., 2010, Orbital chronology of early Eocene hyper- thermals from the Contessa Road section, central Italy: Earth and Planetary Science Letters, v. 290, p. 192– 200, https://doi.org/10.1016/j.epsl.2009.12.021.

Galeotti, S., Moretti, M., Cappelli, C., Phillips, J., Lanci, L., Littler, K., Monechi, S., Petrizzo, M.R., Silva, I.P., Zachos, J.C., 2015. The Bottaccione section at Gubbio, central Italy: a classical Paleocene Tethyan setting revisited. Newsletters on Stratigraphy 48, 325–339. https://doi.org/10.1127/nos/2015/0067.

Galeotti, S., Moretti, M., Sabatino, N., Sprovieri, M., Ceccatelli, M., Francescone, F., Lanci, L., Lauretano, V., and Monechi, S., 2017, Cyclochronology of the Early Eocene carbon isotope record from a composite Contessa Road-Bottaccione section (Gubbio, central Italy): Newsletters on Stratigraphy, v. 50, p. 231–244, doi: 10.1127/nos/2017/0347.

Ghil, M., Allen, M.R., Dettinger, M.D., Ide, K., Kondrashov, D., Mann, M. E., Yiou, P., 2002. Advanced spectral methods for climatic time series. Reviews of geophysics 40, 1003.

Giusberti, L., Boscolo Galazzo, F., Thomas, E., 2016. Variability in climate and productivity during the Paleocene–Eocene Thermal Maximum in the western Tethys (Forada section). Climate of the Past 12, 213-240. doi: 10.5194/cp-12-213-2016.

Giusberti, L., Rio, D., Agnini, C., Backman, J., Fornaciari, E., Tateo, F., Oddone, M., 2007. Mode and tempo of the Paleocene-Eocene thermal maximum in an expanded section from the Venetian pre-Alps. Geological Society of America Bulletin 119, 391–412. https://doi.org/10.1130/B25994.1.

Hansen, J., Sato, M., Kharecha, P., Beerling, D., Berner, R., Masson-Delmotte, V., ... & Zachos, J. C. (2008). Target atmospheric CO2: Where should humanity aim?. arXiv preprint arXiv:0804.1126, doi: 10.2174/1874282300802010217

Hellinger, S.J., 1981, The uncertainties of finite rotations in plate tectonics: Journal of Geophysical Research: Solid Earth, v. 86, p. 9312–9318, doi: 10.1029/JB086iB10p09312.

Hilgen, F. J., Kuiper, K. F., Lourens, L. J., 2010. Evaluation of the astronomical time scale for the Paleocene and earliest Eocene. Earth and Planetary Science Letters 300(1), 139–151.

Hilting, A. K., Kump, L. R., Bralower, T. J., 2008. Variations in the oceanic vertical carbon isotope gradient and their implications for the Paleocene–Eocene biological pump. Paleoceanography 23, PA3222.

Hinnov, L. A., and Hilgen, F. J. (2012). Cyclostratigraphy and astrochronology. In The geologic time scale (pp. 63-83).

Holbourn, A.E., Kuhnt, W., Schulz, M., and Erlenkeuser, H., 2005, Impacts of orbital forcing and atmospheric CO_2 on Miocene ice-sheet expansion: Nature, v. 438, p. 483–487, doi:10.1038/nature04123.

Huber, M., Caballero, R., 2011. The early Eocene equable climate problem revisited. Climate of the Past 7(2), 603–633. Huber, M., Thomas, E., 2008. Paleoceanography: green- house climates. Encyclopedia of Ocean Sciences. 2nd edition, Elsevier, New York, 4229–4239.

Huber, M., Thomas, E., 2008. Paleoceanography: green- house climates. Encyclopedia of Ocean Sciences. 2nd edition, Elsevier, New York, 4229–4239.

Huestis, S.P., and Acton, G.D., 1997, On the construction of geomagnetic timescales from non-prejudicial treatment of magnetic anomaly data from multiple ridges: Geophysical Journal International, v. 129, p. 176–182, doi: 10.1111/j.1365-246X.1997.tb00947.x.

Kasting, J.F., and Richardson, S.M., 1985, Seafloor hydrothermal activity and spreading rates: the eocene carbon dioxide greenhouse revisited: Geochimica et Cosmochimica Acta, v. 49, p. 2541–2544, doi: 10.1016/0016-7037(85)90122-X.

Kennett, J.P., Stott, L.D., 1991. Abrupt deep-sea warming, palaeoceanographic changes and benthic extinctions at the end of the Palaeocene. Nature, v. 353, p. 225–229. https://doi.org/10.1038/353225a0.

Kirschvink, J.L., 1980, The least-squares line and plane and the analysis of palaeomagnetic data: Geophysical Journal International, v. 62(3), p. 699-718, doi.org/10.1111/j.1365-246X.1980.tb02601.x.

Kirtland Turner, S., Sexton, P.F., Charles, C.D., Norris, R.D., 2014. Persistence of carbon release events through the peak of early Eocene global warmth. Nature Geoscience 7, 748–751. https://doi.org/10.1038/ngeo2240.

Koch, P.L., Zachos, J.C., Gingerich, P.D., 1992. Correlation between isotope records in marine and continental carbon reservoirs near the Paleocene Eocene boundary. Nature 358, 319–322.

Krijgsman, W., Hilgen, F.J., Raffi, I., Sierro, F.J., and Wilson, D.S., 1999, Chronology, causes and progression of the Messinian salinity crisis: Nature, v. 400, p. 652–655, doi: 10.1038/23231.

Kurtz, A.C., Kump, L.R., Arthur, M.A., Zachos, J.C., and Paytan, A., 2003, Early Cenozoic decoupling of the global carbon and sulfur cycles: Paleoceanography, v. 18, no. 4. doi: 10.1029/2003P A000908.

Laskar, J., Fienga, A., Gastineau, M., Manche, H., 2011a.La2010: a new orbital solution for the long-term motion of the Earth. Astronomy & Astrophysics 532, A89.

Laskar, J., Gastineau, M., Delisle, J.B., Farrés, A., and Fienga, A., 2011b, Strong chaos induced by close encounters with Ceres and Vesta: Astronomy & Astrophysics, v. 532, L4, https://doi.org/10.1051/0004- 6361/201117504.

Laskar, J., Robutel, P., Joutel, F., Gastineau, M., Correia, A.C.M. and Levrard, B., 2004, A long-term numerical solution for the insolation quantities of the Earth: Astronomy & Astrophysics, v. 428, p. 261–285, doi: 10.1051/0004-6361:20041335.

Lauretano, V., Hilgen, F.J., Zachos, J.C., and Lourens, L.J., 2016, Astronomically tuned age model for the early Eocene carbon isotope events: A new high-resolution $\delta^{13}C$ benthic record of ODP Site 1263 between ~49 and ~54 Ma: Newsletters on Stratigraphy, v. 49, p. 383–400, doi: 10.1127/nos/2016/0077.

Lauretano, V., Littler, K., Polling, M., Zachos, J.C., and Lourens, L.J., 2015, Frequency, magnitude and character of hyperthermal events at the onset of the Early Eocene Climatic Optimum: Climate of the Past, v. 11, p. 1313–1324, doi: 10.5194/cp-11-1313-2015.

Lauretano, V., Zachos, J.C., Lourens, L.J., 2018. Orbitally Paced Carbon and Deep-Sea Temperature Changes at the Peak of the Early Eocene Climatic Optimum. Paleoceanography and Paleoclimatology, https://doi.org/10.1029/2018PA003422.

Laurin, J., Meyers, S. R., Galeotti, S., Lanci, L., 2016. Frequency modulation reveals the phasing of orbital eccentricity during Cretaceous Oceanic Anoxic Event II and the Eocene hyperthermals. Earth and Planetary Science Letters 442, 143–156.

Littler, K., Röhl, U., Westerhold, T., Zachos, J.C., 2014. A high-resolution benthic stable-isotope record for the South Atlantic: Implications for orbital-scale changes in Late Paleocene–Early Eocene climate and carbon cycling. Earth and Planetary Science Letters, v. 401, p. 18-30, https://doi.org/10.1016/j.epsl.2014.05.054.

Lourens, L. J., Hilgen, F. J., Laskar, J., Shackleton, N. J., and Wilson, D.: The Neogene Period, in: A Geological Timescale 2004, edited by: Gradstein, F., Ogg, J., and Smith, A., Cambridge University Press, UK, 409–440, 2004.

Lourens, L.J., Sluijs, A., Kroon, D., Zachos, J.C., Thomas, E., Röhl, U., Bowles, J., and Raffi, I., 2005, Astronomical pacing of late Palaeocene to early Eocene global warming events: Nature, v. 435, p. 1083–1087, https:// doi.org/10.1038/nature03814.

Lowrie, W., Alvarez, W., Napoleone, G., Perch-Nielsen, K., Premoli Silva, I., and Toumarkine, M., 1982, Paleogene magnetic stratigraphy in Umbrian pelagic carbonate rocks: The Contessa sections, Gubbio: Geological Society of America Bulletin, v. 93, p. 414–432, doi: 10.1130/0016-7606(1982)93<414:PMSIUP>2.0.CO;2.

Luciani, V., Dickens, G.R., Backman, J., Fornaciari, E., Giusberti, L., Agnini, C., D'Onofrio, R., 2016. Major perturbations in the global carbon cycle and photosymbiont-bearing planktic foraminifera during the early Eocene. Climate of the Past 12, 981–1007. https://doi.org/10.5194/cp-12-981-2016.

Lunt, D.J., Ridgwell, A., Sluijs, A., Zachos, J., Hunter, S., Haywood, A., 2011. A model for orbital pacing of methane hydrate destabilization during the Palaeogene. Nature Geoscience , v. 4, p. 775–778, https://doi.org/10.1038/ngeo1266.

Lurcock, P.C., and Wilson, G.S., 2012, PuffinPlot: A versatile, user-friendly program for paleomagnetic analysis: Geochemistry, Geophysics, Geosystems, v. 13, doi: 10.1029/2012GC004098.

Malinverno, A., Hildebrandt, J., Tominaga, M., and Channell, J.E.T., 2012, M-sequence geomagnetic polarity time scale (MHTC12) that steadies global spreading rates and incorporates astrochronology constraints: Journal of Geophysical Research: Solid Earth, v. 117, doi: 10.1029/2012JB009260.

Mann, M.E., and Lees, J.M., 1996, Robust estimation of background noise and signal detection in climatic time series: Climatic Change, v. 33, p. 409–445, doi: 10.1007/BF00142586.

Martini, E., 1971, Standard Tertiary and Quaternary Calcareous Nannoplankton Zonation in Farinacci, A. ed., Proceedings of the 2nd Planktonic Conference, Rome, volume 2, Edizioni Tecnoscienza, Rome, 739 - 785.

McGowran, B., 1989, Silica burp in the Eocene ocean: Geology, v. 17, p. 857–860, https://doi. org/10.1130/0091-7613(1989)017<0857:SBITEO>2 .3.CO;2.

Meyers, S.R., 2014. Astrochron: An R package for astrochronology: Available at c ran.rproject.org/web/ packages/astrochron/index.html.

Meyers, S.R., 2015, The evaluation of eccentricity-related amplitude modulation and bundling in paleoclimate data: An inverse approach for astrochronologic testing and time scale optimization: Paleoceanography, v. 30(12), p. 1625-1640, doi.org/10.1002/2015PA002850.

Meyers, S.R., and Sageman, B.B., 2007, Quantification of Deep-Time Orbital Forcing by Average Spectral Misfit: American Journal of Science, v. 307, p. 773-792, doi: 10.2475/05.2007.01.

Meyers, S.R., Sageman, B.B. and Arthur, M.A., 2012, Obliquity forcing of organic matter accumulation during Oceanic Anoxic Event 2, Paleoceanography, v. 27(3), PA3212, doi.org/10.1029/2012PA002286.

Müller, R.D., Dutkiewicz, A., Seton, M., and Gaina, C., 2013, Seawater chemistry driven by supercontinent assembly, breakup, and dispersal: Geology, v. 41, p. 907–910, doi: 10.1130/G34405.1.

Müller, R.D., Dutkiewicz, A., Seton, M., and Gaina, C., 2014, Seawater chemistry driven by supercontinent assembly, breakup and dispersal: REPLY: Geology, v. 42, p. e335–e335, doi: 10.1130/G35636Y.1.

Müller, R.D., Sdrolias, M., Gaina, C., and Roest, W.R., 2008, Age, spreading rates, and spreading asymmetry of the world's ocean crust: Geochemistry, Geophysics, Geosystems, v. 9, doi: 10.1029/2007GC001743.

Müller, R.D., Seton, M., Zahirovic, S., Williams, S.E., Matthews, K.J., Wright, N.M., Shephard, G.E., Maloney, K.T., Barnett-Moore, N., Hosseinpour, M., et al., 2016, Ocean Basin Evolution and Global-

Scale Plate Reorganization Events Since Pangea Breakup: Annual Review of Earth and Planetary Sciences, v. 44, p. 107–138, doi: 10.1146/annurev-earth-060115-012211.

Napoleone, G., Premoli Silva, I., Heller, F., Cheli, P., Corezzi, S., and Fischer, A.G., 1983, Eocene magnetic stratigraphy at Gubbio, Italy, and its implications for Paleogene geochronology: Geological Society of America Bulletin, v. 94, p. 181–191, doi: 10.1130/0016-7606(1983)94<181:EMSAGI>2.0.CO;2.

Nicolo, M.J., Dickens, G.R., Hollis, C.J., and Zachos, J.C., 2007. Multiple early Eocene hyperthermals: Their sedimentary expression on the New Zealand continental margin and in the deep sea. Geology, v. 35, p. 699–702, https://doi.org/10.1130/G23648A.1.

Norton, I.O., and Lawver, L.A., 2014, Seawater chemistry driven by supercontinent assembly, breakup, and dispersal: COMMENT: Geology, v. 42, p. e334–e334, doi: 10.1130/G35109C.1.

Ogg, J.G., 2012, The geomagnetic polarity time scale, in Gradstein, F.M., Ogg, J.G., Schmitz, M.D., and Ogg, G.M., eds., The Geologic Time Scale 2012: Amsterdam, Netherlands, Elsevier 85–113, https://doi.org/10.1016/B978-0-444-59425-9.00005-6.

Ogg, J.G., and Smith, A.G., 2004, The geomagnetic polarity time scale, in Gradstein, F.M., Ogg, J.G., and Smith, A.G., eds., A Geological Time Scale, 2004: Cam- bridge, UK, Cambridge University Press 589, p. A89, https://doi.org/10.1051/0004-6361/201116836.

Pagani, M., Caldeira, K., Archer, D., Zachos, J.C., 2006. An ancient carbon mystery. Science, v. 314, p. 1556–1557, https://doi.org/10.1126/science.1136110.

Pagani, M., N. Pedentchouk, M. Huber, A. Sluijs, S. Schouten, H. Brinkhuis, J. S. Sinninghe Damsté, G. R. Dickens, and Expedition-Scientists, 2006, Arctic hydrology during global warming at the Palaeocene-Eocene thermal maximum, Nature, 442, 671–675.

Pagani, M., Zachos, J. C., Freeman, K. H., Tipple, B., Bohaty, S., 2005. Marked decline in atmospheric carbon dioxide concentrations during the Paleogene. Science 309, 600– 603.

Paillard, D., Labeyrie, L., and Yiou, P., 1996, Macintosh program performs time-series analysis: Eos (Transactions, American Geophysical Union), v. 77, p. 379.

Pälike, H., and Hilgen, F., 2008, Rock clock synchronization: Nature Geoscience, v. 1, p. 282, doi: 10.1038/ngeo197.

Pälike, H., Norris, R. D., Herrle, J. O., Wilson, P. A., Coxall, H. K., Lear, C. H., Shackleton, N. J., Tripati, A. K., and Wade, B. S., 2006. The Heartbeat of the Oligocene Climate System, Science, 314, 1894-1898.

Parsons, B., and Sclater, J.G., 1977, An analysis of the variation of ocean floor bathymetry and heat flow with age: J. Geophys. Res., v. 82, p. 802–827, doi: 10.1029/JB082i005p00803.

Patriat, P., and Achache, J., 1984, India-Eurasia collision chronology has implications for crustal shortening and driving mechanism of plates: Nature, v. 311, p. 615–621, doi: 10.1038/311615a0.

Patriat, P., and Segoufin, J., 1988, Reconstruction of the Central Indian Ocean: Tectonophysics, v. 155, p. 211–234, doi: 10.1016/0040-1951(88)90267-3.

Ravizza, G., Norris, R. N., Blusztajn, J., & Aubry, M. P., 2001. An osmium isotope excursion associated with the late Paleocene thermal maximum: Evidence of intensified chemical weathering. Paleoceanography and Paleoclimatology, 16(2), 155-163, doi: 10.1029/2000PA000541

Rea, D.K., Zachos, J.C., Owen, R.M., and Gingerich, P.D., 1990, Global change at the Paleocene-Eocene boundary: climatic and evolutionary consequences of tectonic events: Palaeogeography, Palaeoclimatology, Palaeoecology, v. 79, p. 117–128, doi: 10.1016/0031-0182(90)90108-J.

Renne, P. R., Deino, A. L., Hilgen, F. J., Kuiper, K. F., Mark, D. F., Mitchell, W. S., Smit, J., 2013. Time scales of critical events around the Cretaceous-Paleogene boundary. Science 339(6120), 684–687.

Röhl, U., Brinkhuis, H., Sluijs, A., and Fuller, M., 2004. On the search for the Paleocene/Eocene boundary in the Southern Ocean: Exploring ODP Leg 189 holes 1171D and 1172D, Tasman Sea, *in* Exon, N.F., Kennett, J.P., and Malone, M.J. eds., Geophysical Monograph Series, Washington, D. C., American Geophysical Union, v. 151, p. 113–125, doi: 10.1029/151GM08.

Röhl, U., Brinkhuis, H., Stickley, C.E., Fuller, M., Schellenberg, S.A., Wefer, G., Williams, G.L., 2004. Sea level and astronomically induced environmental changes in Middle and Late Eocene sediments from the East Tasman Plateau, in: Exon, N.F., Kennett, J.P., Malone, M.J. (Eds.), Geophysical Monograph Series. American Geophysical Union, Washington, D. C., pp. 127–151. https://doi.org/10.1029/151GM09.

Röhl, U., Westerhold, T., Bralower, T.J., Zachos, J.C., 2007. On the duration of the Paleocene-Eocene thermal maximum (PETM). Geochemistry, Geophysics, Geosystems 8, https://doi.org/10.1029/2007GC001784.

Röhl, U., Westerhold, T., Monechi, S., Thomas, E., Zachos, J.C., Donner, B., 2005. The Third and Final Early Eocene Thermal Maximum: Characteristics, Timing and Mechanisms of the 'X' Event, GSA Annual Meeting 37. Geological Society of America, Salt Lake City, USA. 264 pp.

Royer, J. Y., and Sandwell, D. T., 1989, Evolution of the eastern Indian Ocean since the Late Cretaceous: Constraints from Geosat altimetry: Journal of Geophysical Research: Solid Earth, v. 94, no. B10, p. 13755-13782, https://doi.org/10.1029/JB094iB10p13755.

Seton, M., Flament, N., Whittaker, J., Müller, R.D., Gurnis, M., and Bower, D.J., 2015, Ridge subduction sparked reorganization of the Pacific plate-mantle system 60-50 million years ago: Pacific plate-mantle reorganization: Geophysical Research Letters, v. 42, p. 1732–1740, doi: 10.1002/2015GL063057.

Sexton, P.F., Norris, R.D., Wilson, P.A., Pälike, H., Westerhold, T., Röhl, U., Bolton, C.T., Gibbs, S., 2011. Eocene global warming events driven by ventilation of oceanic dissolved organic carbon. Nature 471, 349–352, https://doi.org/10.1038/nature09826.

Shaffer, G., Huber, M., Rondanelli, R., Pepke Pedersen, J.O., 2016. Deep time evidence for climate sensitivity increase with warming. Geophysical Research Letters, v. 43, p. 6538-6545, https://doi.org/10.1002/2016GL069243.

Sluijs, A., Brinkhuis, H., Crouch, E.M., John, C.M., Handley, L., Munsterman, D., Bohaty, S.M., Zachos, J.C., Reichart, G.-J., Schouten, S., Pancost, R.D., et al., 2008, Eustatic variations during the Paleocene-Eocene greenhouse world: Paleoceanography, v. 23, doi: 10.1029/2008PA001615.

Sluijs, A., Brinkhuis, H., Schouten, S., Bohaty, S.M., John, C.M., Zachos, J.C., Reichart G.J., Sinninghe Damsté J.S., Crouch E.M., Dickens G.R., 2007. Environmental precursors to rapid light carbon injection at the Palaeocene/Eocene boundary. Nature, v. 450, p. 1218, DOI: 10.1038/nature06400.

Sluijs, A., Röhl, U., Schouten, S., Brumsack, H.-J., Sangiorgi, F., Sinninghe Damsté, J.S., Brinkhuis, H., 2008. Arctic late Paleocene–early Eocene paleoenvironments with special emphasis on the Paleocene-Eocene thermal maximum (Lomonosov Ridge, Integrated Ocean Drilling Program Expedition 302). Paleoceanography 23. https://doi.org/10.1029/2008PA001615.

Sluijs, A., Schouten, S., Pagani, M., Woltering, M., Brinkhuis, H., Sinninghe Damsté, J.S., Dickens, G.R., Huber, M., Reichart G.J., Stein, R., Matthiessen, J., Lourens, L.J., Pedentchouk, N., Backman, J., Moran, K., Expedition 302 Scientists, 2006. Subtropical Arctic Ocean temperatures during the Palaeocene/Eocene thermal maximum. Nature, v. 441, p. 610, https://doi.org/10.1038/nature04668.

Smith, W.H.F., and Sandwell, D.T., 1997, Global Sea Floor Topography from Satellite Altimetry and Ship Depth Soundings: Science, v. 277, p. 1956–1962, doi: 10.1126/science.277.5334.1956.

Stap, L., Lourens, L. J., Thomas, E., Sluijs, A., Bohaty, S., & Zachos, J. C., 2010. High-resolution deep-sea carbon and oxygen isotope records of Eocene Thermal Maximum 2 and H2. Geology, v. 387, p. 607–610, https://doi.org/10.1130/g30777.1.

Suganuma, Y., Ogg, J. G., 2006. Campanian through Eocene magnetostratigraphy of sites 1257–1261, ODP leg 207, Demerara rise (Western Equatorial Atlantic). In Proc. Ocean Drill. Program Sci. Results 207, 1–48.

Talwani, M., and Heirtzler, J.R., 1964, Computation of magnetic anomalies caused by two dimensional structures of arbitrary shape, *in*: G. Parks, Ed., Computers in the Mineral Industries, v. 9, Stanford Univ. Publ., Stanford, California, p. 464–480.

Tarduno, J.A., 2007, On the motion of Hawaii and other mantle plumes: Chemical Geology, v. 241, p. 234–247, doi: 10.1016/j.chemgeo.2007.01.021

Thomas, D. J., J. C. Zachos, T. J. Bralower, Thomas E., and Bohaty S., 2002, Warming the fuel for the fire: Evidence for the thermal dissociation of methane hydrate during the Paleocene-Eocene thermal maximum, Geology, 30, 1067–1070.

Thomas, E., 1989, Development of Cenozoic deep-sea benthic foraminiferal faunas in Antarctic waters, Geol. Soc. Spec. Publ. London., 47, 283–296.

Thomas, E., and Shackleton N. J., 1996, The Palaeocene-Eocene benthic foraminiferal extinction and stable isotope anomalies, in Correlation of the Early Paleogene in Northwestern Europe, edited by R. W. O. B. Knox et al., Geol. Soc. Spec. Publ., 101, 401–441.

Tisseau, J., and Patriat, P., 1981, Identification des anomalies magnétiques sur les dorsales à faible taux d'expansion: Méthode des taux fictifs. Earth and Planetary Science Letters, v. 52 (2), 381–396, doi:10.1016/0012-821X(81)90191-6.

Torrence, C., and Compo, G.P., 1998, A practical guide to wavelet analysis: Bulletin of the American Meteorological Society, v. 79, p. 61–78, doi:10.1175/15200477(1998)079<0061:APGTWA>2.0.CO;2.

Tripati, A., and Elderfield, H., 2005, Deep–Sea Temperature and Circulation Changes at the Paleocene-Eocene Thermal Maximum: Science, v. 308, p. 1894–1898, doi: 10.1126/science.1109202.

Tsukui, K., Clyde, W. C., 2012. Fine-tuning the calibration of the early to middle Eocene geomagnetic polarity time scale: Paleomagnetism of radioisotopically dated tuffs from Laramide foreland basins. Geological Society of America Bulletin 124, 870–885.

Turtù, A., Lauretano, V., Catanzariti, R., Hilgen, F.J., Galeotti, S., Lanci, L., Moretti, M., and Lourens, L.J., 2017, Integrated stratigraphy of the Smirra Core (Umbria-Marche Basin, Apennines, Italy): A new early Paleogene reference section and implications for the geologic time scale: Palaeogeography, Palaeoclimatology, Palaeoecology, v. 487, p. 158–174, doi: 10.1016/j.palaeo.2017.08.031.

Vandenberghe, N., Hilgen, F.J., Speijer, R.P., Ogg, J.G., Gradstein, F.M., Hammer, O., and Hooker, J.J., 2012,The Paleogene period, in Gradstein, F.M., Ogg, J.G., Schmitz, M.D., and Ogg, G.M., eds., The Geological Time Scale 2012: Amsterdam, Netherlands, Elsevier 855–921.

Westerhold, T., Röhl, U., 2009. High resolution cyclostratigraphy of the early Eocene – new insights into the origin of the Cenozoic cooling trend. Climate of the Past 5, 309–327. https://doi.org/10.5194/cp-5-309-2009.

Westerhold, T., Röhl, U., and Laskar, J., 2012. Time scale controversy: Accurate orbital calibration of the early Paleogene, Geochem. Geophys. Geosyst., 13, Q06015, doi:10.1029/2012gc004096.

Westerhold, T., Röhl, U., Donner, B., Zachos, J.C., 2018. Global Extent of Early Eocene Hyperthermal Events: A New Pacific Benthic Foraminiferal Isotope Record From Shatsky Rise (ODP Site 1209). Paleoceanography and Paleoclimatology 33, 626–642. https://doi.org/10.1029/2017PA003306.

Westerhold, T., Röhl, U., Frederichs, T., Agnini, C., Raffi, I., Zachos, J.C., and Wilkens, R.H., 2017, Astronomical calibration of the Ypresian timescale: implications for seafloor spreading rates and the chaotic behavior of the solar system?: Climate of the Past, v. 13, p. 1129–1152, doi: 10.5194/cp-13-1129-2017.

Westerhold, T., Röhl, U., Frederichs, T., Bohaty, S.M., Zachos, J.C., 2015. Astronomical calibration of the geological timescale: closing the middle Eocene gap. Climate of the Past 11, 1181–1195. https://doi.org/10.5194/cp-11-1181-2015.

Westerhold, T., Röhl, U., Laskar, J., Raffi, I., Bowles, J., Lourens, L.J., and Zachos, J.C., 2007, On the duration of magnetochrons C24r and C25n and the timing of early Eocene global warming events: Implications from the Ocean Drilling Program Leg 208 Walvis Ridge depth transect: Paleoceanography, v. 22, PA2201, https://doi .org/10.1029/2006PA001322.

Westerhold, T., Röhl, U., McCarren, H.K., Zachos, J.C., 2009. Latest on the absolute age of the Paleocene–Eocene Thermal Maximum (PETM): new insights from exact stratigraphic position of key ash layers +19 and –17. Earth and Planetary Science Letters 287, 412–419.

Whittaker, J.M., Muller, R.D., Leitchenkov, G., Stagg, H., Sdrolias, M., Gaina, C., and Goncharov, A., 2007, Major Australian-Antarctic Plate Reorganization at Hawaiian-Emperor Bend Time: Science, v. 318, p. 83–86, doi: 10.1126/science.1143769.

Wilson, D.S., 1993, Confirmation of the astronomical calibration of the magnetic polarity timescale from sea-floor spreading rates: Nature, v. 364, p. 788–790, doi: 10.1038/364788a0.

Wilson, D.S., 2016, Revision of Paleogene plate motions in the Pacific and implications for the Hawaiian-Emperor bend: COMMENT: Geology, v. 44, p. e384–e384, doi: 10.1130/G37388C.1.

Wright, N.M., Müller, R.D., Seton, M., and William, S.E., 2016, Revision of Paleogene plate motions in the Pacific and implications for the Hawaiian-Emperor bend: REPLY: Geology, v. 44, p. e385–e385, doi: 10.1130/G37828Y.1.

Wright, N.M., Müller, R.D., Seton, M., and Williams, S.E., 2015, Revision of Paleogene plate motions in the Pacific and implications for the Hawaiian-Emperor bend: Geology, v. 43, p. 455–458, doi: 10.1130/G36303.1.

Wright, N.M., Seton, M., Williams, S.E., and Müller, R.D., 2016, The Late Cretaceous to recent tectonic history of the Pacific Ocean basin: Earth-Science Reviews, v. 154, p. 138–173, doi: 10.1016/j.earscirev.2015.11.015.

Zachos, J. C., Dickens, G. R., Zeebe, R. E., 2008. An early Cenozoic perspective on greenhouse warming and carbon-cycle dynamics. Nature 451, 279–283.

Zachos, J. C., McCarren, H., Murphy, B., Röhl, U., Westerhold, T., 2010. Tempo and scale of late Paleocene and early Eocene carbon isotope cycles: Implications for the origin of hyperthermals. Earth and Planetary Science Letters 299, 242–249.

Zachos, J.C., Dickens, G.R., Zeebe, R.E., 2008. An early Cenozoic perspective on greenhouse warming and carbon-cycle dynamics. Nature, v. 451, p. 279–283, doi:10.1038/nature06588.

Zachos, J.C., McCarren, H., Murphy, B., Röhl, U., and Westerhold, T., 2010, Tempo and scale of late Paleocene and early Eocene carbon isotope cycles: Implications for the origin of hyperthermals: Earth and Planetary Science Letters, v. 299, p. 242–249, doi: 10.1016/j.epsl.2010.09.004.

Zachos, J.C., Pagani, M., Sloan, L.C., Thomas, E., Billups, K., 2001. Trends, Rhythms, and Aberrations in Global Climate 65 Ma to Present. Science 292, 686–693. doi:10.1126/science.1059412.

Zachos, J.C., Röhl, U., Schellenberg, S.A., Sluijs, A., Hodell, D.A., Kelly, D.C., Thomas, E., Nicolo, M., Raffi, I., Lourens, J.L., et al., 2005, Rapid acidification of the ocean during the Paleocene-Eocene thermal maximum: Science, v. 308, p. 1611–1615, https://doi .org/10.1126/science.1109004.

Zeebe, R.E., Zachos, J.C., 2007. Reversed deep-sea carbonate ion basin gradient during Paleocene-Eocene thermal maximum. Paleoceanography 22. https://doi.org/10.1029/2006PA001395.